Study on three-dimensional deformation of epithelial sheets in lumen and dome morphogenesis with *in vitro* cell culture model

（インビトロ細胞培養実験系を用いた管腔形成及び
ドーム形成における上皮細胞シートの
三次元変形に関する研究）

Sumire Ishida-Ishihara

December 2020

Doctoral Dissertation

Transdisciplinary Life Science Course

Graduate School of Life Science

Hokkaido University

Abbreviations

2D: two-dimension(al)

3D: three-dimension(al)

AQP: aquaporin

bHS: basal hypertonic stress

ECM: extracellular matrix

F-dome: fluid-filled dome

G-dome; gel-filled dome

GP: genipin

GP-Matrigel: genipin-treated Matrigel

H-DMEM: hypertonic DMEM

I-DMEM: isotonic DMEM

IS: isotonic stress

MDCK cells: Madin-Darby Canine Kidney cells

MDCK-WT cells: MDCK wild type cells

MDCK-CAAX cells:

MDCK-2 cells: MDCK subcloned line 2

MRLC: myosin regulatory light chain

1P-MRLC: mono-phosphorylated MRLC

2P-MRLC: di-phosphorylated MRLC

ROCK: Rho-associated, coiled coil-containing kinase

TGF-β1: transforming growth factor-β1

Chapter 1

General Introduction

1-1. Development and Morphogenesis

Development of animals starts from a single cell, a zygote. A zygote divides repeatedly and forms complicated shapes in the similitude of its parents. It has been a long-standing question that how the cells accurately develop the 3-dimensional (3D) shapes. Recent studies have demonstrated that the deformation of cell sheet plays an important role in the shape forming. Cell sheet deforms via the accumulation of cell's behaviors, such as cellular contractile force, cell shape change, cell proliferation and collective cell migration. Epithelial cells show lumen and dome formation *in vitro*, however, how sheet deformation contributes to them has not been fully explained yet.

1-1-1. History of Developmental Biology

Developmental biology has been studies since ancient times. Aristotle (B.C. 384 – B.C. 322) wrote about development in his book, Generation of Animals. He observed hen's eggs and found chicks are born from a formless state. However, the hypothesis that says an invisibly small child with complete 3D shapes exists in an egg or a sperm and the child gets big in pregnancy (preformation theory) was supported until eighteenth centuries. Casper Frendrich Wolff (1733-1794) precisely observed the development of hen's eggs and suggested that an organ is formed from a disorderly cluster during development (epigenesis theory). Establishment of cell theory, which suggests that cells are the basic unit of all organisms, supported the epigenesis and accelerated to study development on the basis of cells (Wolpert and Tickle, 2012). Concurrently, cell theory demonstrated that the 3D shapes are generated from the formless accumulation of cells.

After this, experimental embryology led understanding of development. Scientists applied a certain treatment to embryos and investigated the mechanisms of development from the results of the treatments. For example, Hans Spemann (1869-1941) and Hilde Mangold (1898-1924) transplanted a part of embryo to another embryo and found the donor part induced another body formation to the recipient embryo (Wolpert and Tickle, 2012). From this result, they found that the specific cells are able to lead the direction of the development.

In 1920s, chromosomes are introduced as a gene carrier by Thomas Hunt Morgan (1866-1945) who made a great genetic contribution to developmental biology

(Raven et al., 2006) , Gregor Mendel (1822-1844) demonstrated that morphologic traits are inherited by genes from both parents to offspring. Morgan and his colleagues established the Mendel's work and showed that genes exist on chromosome, not on protein which were thought as a gene carrier in those days. They crossed mutated *Drosophila* and observed the character of offspring. By both analyzing the ratio of expressed character and investigating the pattern of salivary chromosome, they proved that genes exist on chromosomes. Oswald Theodore Avery (1877-1955), Alfred Day Harsy (1908-1997) and Martha Cowles Chase (1927-2003) also demonstrated that genes are not on protein but on DNA (Raven et al., 2006). Avery incubated the bacteria *Diplococcus pneumoniae* with either protein or DNA extracted from the bacteria with different phenotypes. As a result, only the bacteria incubated with DNA obtained the different phenotype of the extracted source. Harsy and Chase used phage to prove the gene carrier. They labeled the either protein or DNA of the phage with radioisotopes and infected them to bacteria in different culture. Then they separated phage body and the bacteria and detected the radioisotope. The results showed that only the radioisotope of DNA was detected from the infected bacteria. From these, Harsy and Chase concluded that DNA, not protein, was injected into bacteria as genetic materials in order to make up the phage's offspring. These prominent works revealed that DNA carries gene information, however, how the information is passed on was unexplained.

This question was solved by James Watson (1928-) and Francis Click (1916-2004) in 1953 (Raven et al., 2006). They clarified DNA has double-strand structure with complementation of DNA basis (Adenine pairs with Thymine, Guanine pairs with Cytosine). When the double-strand structures were separated, each strand calls DNA bases to pair off and then the strands are replicated. By further studies of molecular biology, gene editing techniques was established. With these techniques, the expression and function of genes at each stage of development have been largely clarified in modern developmental biology. However, it has been difficult to explain how group of cells coordinately build the 3D shapes only by the gene expression patterns.

In addition to gene technics, biophysical analysis gains important roles in development, especially in understanding how the organs are shaped (Gilmour et al., 2017; Keller, 2012; Okuda et al., 2015). Biophysical analysis approaches the shape forming from the viewpoint of the deformation of cell sheets. The recent studies

reported that cell sheet deformation is the basic event of the 3D shape forming. The deformation is caused by accumulation of single cell's behaviors, such as cellular contractile force, cell shape change, cell proliferation and cell migration. Recently, it has been also revealed that the mechanical properties of scaffolds modify gene expression and subsequent cell behaviors (Dupont et al., 2011; Haga et al., 2005; Imai et al., 2015; Ishihara et al., 2016; Ishihara et al., 2013; Nukuda et al., 2015; Paszek et al., 2005; Rozario and DeSimone, 2010). However, how the deformation of cell sheet and the mechanical properties of scaffolds contribute to build the complex 3D shapes are largely unknown. As described above, development has been studied for a long time, yet, the whole picture has not been explained.

1-1-2. Basic Stages of Vertebrate Development

Development of vertebrates has several stages, such as cleavage, gastrulation, neurulation, and organogenesis in the vertebrates (Raven et al., 2006). The single cell repeats cleavage to produce smaller cells (blastomeres) after the fertilization and becomes an embryo. As the cleavage proceeds, the blastomeres obtain fluid-filled lumen at the center of blastomeres. This is called blastula.

After the blastula is formed, the embryo undergoes gastrulation. The part of surface cells invaginates and moves to the inside of the embryo. Through the gastrulation process, cells are rearranged their positions and differentiate into three germ layers; ectoderm, mesoderm or endoderm. There three germ layers mainly differentiate into epidermis and nerve tissue, skeleton and connective tissue, or epithelium of a gastrointestinal tract, respectively.

Then the embryo start neurulation. Notochord, which is generated from mesoderm at the end stage of gastrulation, triggers folding of ectoderm and form a long groove in long axis direction of the embryo. The both edges of the groove move and fuse together, resulting in the formation of a neural tube beneath the ectoderm. Just before the neural tube closure, neural crest cells appeared by being separated from the neural tube. The neural crest cells spread out and induce the various characteristic structures of the vertebrates at the point of arrival.

The last stage of the development is organogenesis. In organogenesis, cells proliferate to increase the size of the embryo. And the cells of the three germ layers interact each other to develop the organs.

1-1-3. Morphogenesis

In various stages in development, group of cells coordinately generates the characteristic shapes of organs. This shape forming process is called morphogenesis. In morphogenesis, the monolayer of epithelial cells plays a central role to form the organ's shapes via the cell sheet deformation and collective cell migration.

1-1-3-1. Characters of Epithelial Cells

Epithelial cells are highly polarized with distinct protein localization patterns to perform specialized functions. Simple columnar epithelial cells cover the surface of digestive tract including stomach, intestines and of kidney tubes. They form a monolayer with connection to neighboring cells on their lateral side. The basal of the cells adhere to scaffolds of basement membrane, and the apical (opposite side of basal) is free from adhesion (Figure 1.1A). Like these, epithelial cells are structurally polarized. In polarized epithelial cells, specific proteins localize on the cell membrane for each compartment. On basolateral (basal and lateral) membrane, membrane protein for cell-cell adhesion (E-cadherin) and cell-substrate adhesion (integrins) richly exist, however, these proteins rarely localize on apical membrane. Likewise, podocalyxin/gp135 richly exists on apical surface of kidney epithelial cells, but it hardly exists on basolateral surface (Ojakian and Schwimmer, 1988). Tight junction is the complex of membrane proteins that localize between cells to establish the polarized distribution of the membrane proteins (Zihni et al., 2016).

Because epithelial cells localize along the border between the inside and outside of the bodies, epithelial monolayers have a function of the barrier to defend the body against foreign substances and a function to take water and substances necessary for the body. Tight junctions play a central role for the barrier functions (Zihni et al., 2016). They tightly close the intracellular spaces to restrict the invasion of virus, bacteria, and large molecules (>3.5 angstrom) (Figure 1.1B)(Van Itallie et al., 2009). Tight junctions do not shut out the all substances but slightly pass small molecules including water and ions. The transfer of the small molecules through the intercellular space is called paracellular transport. The molecules are also transferred through cell bodies. Transporters and channels take the substances actively and passively, respectively. For example, in small intestine, nutrition is taken into the cells from apical

side and then transported from the cell to blood vessels on basal side. This transporting system is called transcellular transport. The barrier function and epithelial transport generate osmotic stress which is essential for maintaining body homeostasis and also contributes to morphogenesis (see section 1-3-3).

The migration of cells is essential for physiological functions such as wound healing, tissue morphogenesis, and also for pathological processes such as cancer invasion (Friedl and Gilmour, 2009). The mechanisms of migration have been extensively studied in single cell (Ridley et al., 2003). In recent years, migration of group of cells (collective cell migration) has been increasingly recognized. In collective cell migration, cells move together with keeping cell-cell connections stably or transiently (Figure 1.1C) (Ilina and Friedl, 2009). Collective migration has been studied both *in vivo* and *in vitro* (see section 3-1-3 for *in vitro* studies). A directed collective migration often modifies the tissue shapes *in vivo*. Examples include border-cell migration in *Drosophila*, lateral-line migration in zebrafish, and gastrulation in vertebrates (Friedl and Gilmour, 2009; Scarpa and Mayor, 2016). The directed collective migration is regulated by chemical and mechanical signals from surrounding environment, such as the gradient of chemokines and contact inhibition of locomotion, respectively. In addition to directional migration, rotational migration is also observed in somite of zebrafish and in egg chamber of *Drosophila*, which accompanies the deformation of the tissues (Chen et al., 2019; Hollway et al., 2007). Like these, the contribution of collective migration to morphogenesis has been extensively studied in recent days.

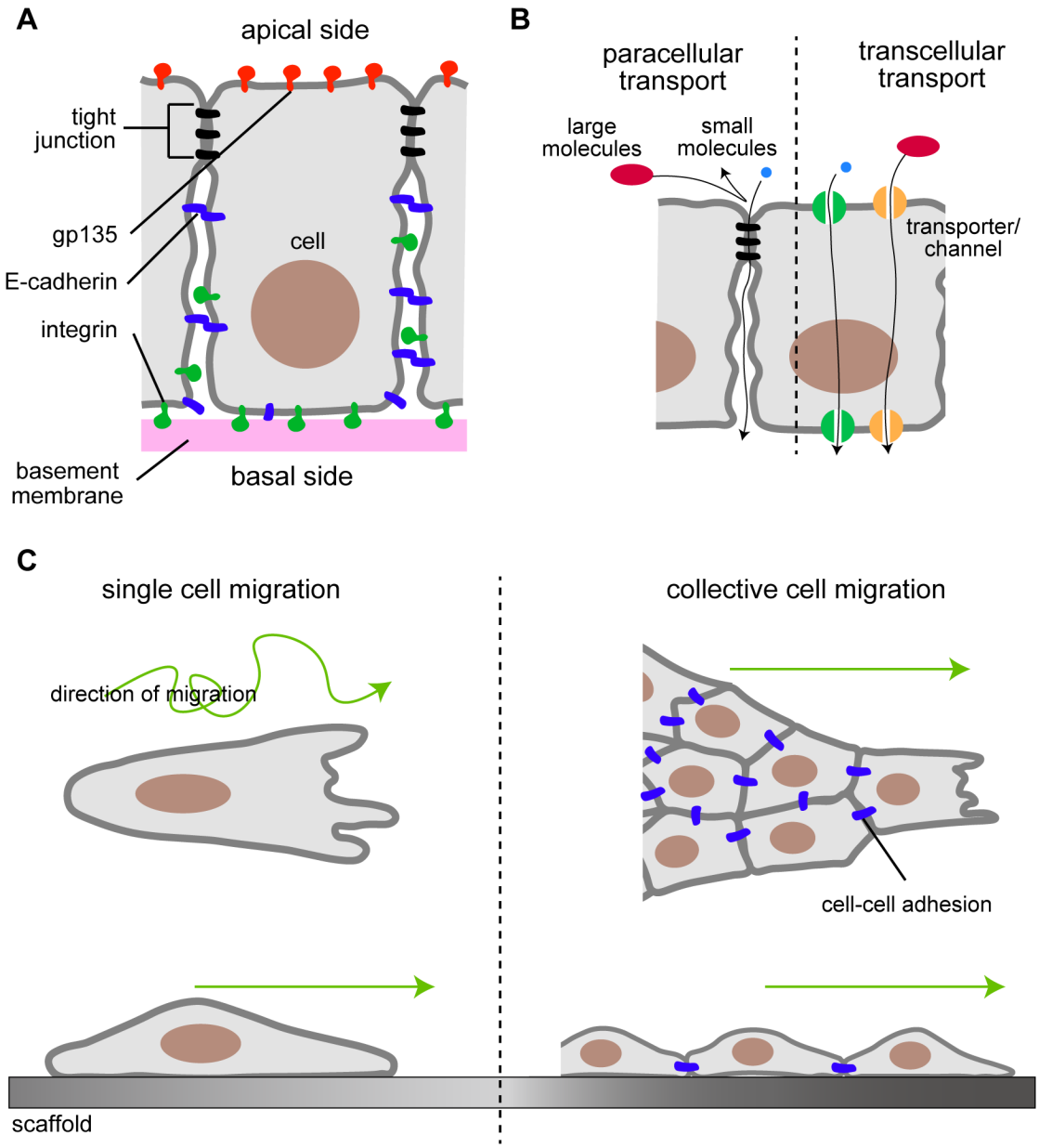

Figure 1.1 Characters of Epithelial Cells

(**A**) Apical-basal polarity and distinct protein distribution on plasma membranes. (**B**) Paracellular and transcellular transport of epithelial cells. (**C**) Single and collective migration of epithelial cells.

1-1-3-2. Deformation of Epithelial Sheets

During the morphogenesis, deformation of epithelial monolayers have critical role in 3D tissue shaping (Gilmour et al., 2017). For example, wings of adult *Drosophila* and horns of adult beetles are prepared in pupa as compressed and folded epithelial sheets, respectively (Diaz-de-la-Loza et al., 2018; Matsuda et al., 2017). At

the transformation, the cell sheets quickly expand and unfolded, respectively, to emerge 3D morphologies of the adult tissue. Sheet deformation is also observed in vertebrates. Optic-cup develops via folding back of cell sheets (Figure 1.2). In neural tube formation, smooth epithelial sheets fold and then the cells at the edge fuse to close the groove and then form a tube structure with a lumen (Nikolopoulou et al., 2017). In chick and mouse, dome-like structures (villi) on intestinal surface are emerged by the bending of a smooth epithelial monolayer (Chin et al., 2017; Shyer et al., 2013; Walton et al., 2016a; Walton et al., 2016b). Hence, the deformation of cell sheets are fundamental processes in morphogenesis, however, the mechanisms is largely unknown.

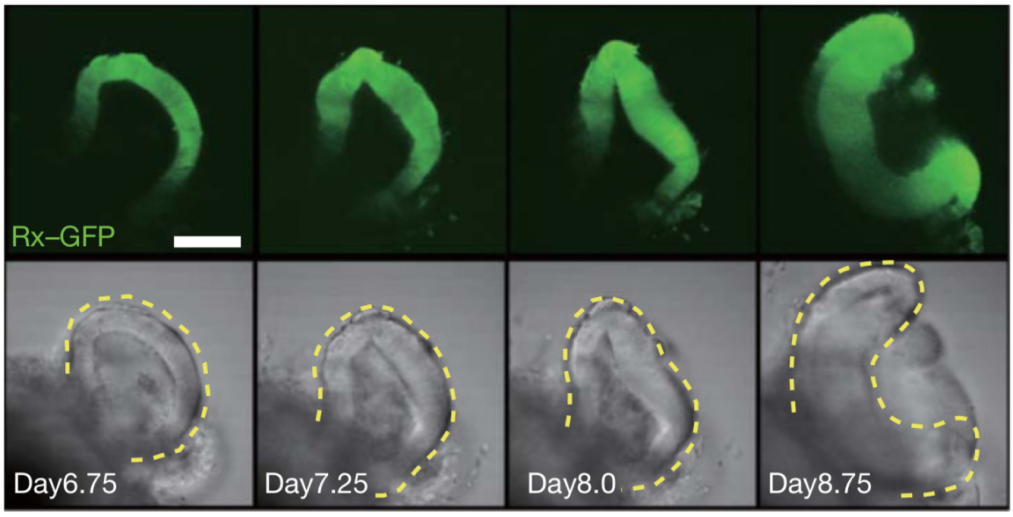

(Eiraku *et al.*, 2013, modified)

Figure 1.2 Epithelial folding observed in optic-cup morphogenesis.

Time sequence of optic-cup morphogenesis derived from mouse embryonic stem cell aggregates. Green indicates the epithelial cell sheets.

1-1-3-4. Epithelial Morphogenesis *in vitro*

Epithelial morphogenesis is also observed *in vitro*. Madin-Darby Canine Kidney cells (MDCK cells) are derived from proximal tubes of kidney of a dog (Gaush et al., 1966). MDCK cells preserve the epithelial characters well, showing the distinct polarized distribution of membrane proteins, barrier functions, and ion transport activity (Dukes et al., 2011; Simmons, 1982). Therefore, they have been used as an excellent model to study epithelial morphogenesis *in vitro*. MDCK cells are known to show

lumen morphogenesis (see Chapter 3) and dome morphogenesis (see Chapter 4) with sheet deformations, but the factors to cause the deformations have not been fully investigated yet.

1-2. Extracellular Matrix (ECM).

Extracellular matrix (ECM) is the non-cellular component of the hydrogel in organs and tissues (Rozario and DeSimone, 2010). ECM hydrogel is composed of 3D networks of proteins containing water. Gelatinous collagen (collagen gel) and Matrigel is widely used in *in vitro* cell culture. ECMs do not only fill the space between cells but also have functions as adhesive scaffold and structural supports of morphogenesis. Furthermore, the mechanical properties of ECM influence morphogenesis.

1-2-1. Collagen Gel

Collagens are the most abundant proteins in animal bodies and provide the mechanical strength to the matrix (Rozario and DeSimone, 2010). Collagen molecules form a long fiber with a triple-helical structure of the collagen α-chains. About 28 types of collagen family have been identified. Type-I collagen is the main component of skin and bone and gelated type-I collagen (collagen gel) is widely used in *in vitro* cell culture. Type-I collagen molecules orderly accumulate to form a collagen fibril. Collagen fibrils often aggregate and become thick bundles (collagen fibers), which are visible by the light microscope. They provide the resistance to traction force. Both the increase of the collagen concentration and chemical crosslinking of collagen fibers increase the elasticity of the collagen gels (Miroshnikova et al., 2011; Mizutani et al., 2006a; Paszek et al., 2005; Sundararaghavan et al., 2008).

1-2-2. Matrigel

Matrigel is basement membrane proteins secreted by Engelbreth-Holm-Swarm mouse sarcoma cells. Matrigel is mainly composed of laminin, type-IV collagen, nidogen and perlecan (Yurchenco, 2011). Laminin is a glycoprotein which has a large family. A laminin molecule is formed of a cross with three long polypeptide chains (Rozario and DeSimone, 2010). Tails of the molecule function as self-assembly or interact with other molecules to form the network. Type-IV collagen is one of the network-forming collagens and another main component of the basement membrane. Laminin and type-IV collagen interact with other molecules in basement membranes, including nidogen and perlecan, to form a highly crosslinked network. Matrigel has been used for various experiments *in vitro*, such as lumen formation of

epithelial cells, angiogenesis of vascular endothelial cells, and invasion of cancer cells.

1-2-3. Culture Dimension of ECM Scaffolds

Adhesion to ECM is an important cue for cells. Cells adhere to ECM via membrane proteins integrins (described in section 1-3-2). For example, the inhibition of integrin-ECM binding modulates cell-substrate adhesion and disrupts the rearrangement of cell positions in *Xenopus* development (Marsden and DeSimone, 2003). *In vitro* studies also reported that collective migration of both normal epithelial cells and cancer cells is inhibited by the disruption of integrin-β1 (Kato et al., 2014; Yamaguchi et al., 2015). In addition, knockdown of collagen receptor protein discoidin domain receptor tyrosine kinase 1 (DDR1) causes hyperproliferation in branching morphogenesis of mouse (Vogel et al., 2001). Like these, adhesion to ECM plays important roles in various cell behaviors.

In addition, the culture dimension of the adhesive scaffolds is important experimental condition to study morphogenesis *in vitro* as epithelial cells show different morphologies in different culture dimension. When cells are seeded onto flat collagen gel (which referred as two-dimensional (2D) culture)(Figure 1.3), cells grow as a flat monolayer (Yu et al., 2005). On the other hand, cells form a sphere structure with a lumen after cells are embedded into collagen gel (referred as 3D culture) (Martin-Belmonte and Mostov, 2008; O'Brien et al., 2002; Yu et al., 2005). Gel overlay is the methods to shift the culture dimension from 2D to 3D (Hall et al., 1982; Hashimoto et al., 2008; Schwimmer and Ojakian, 1995; Yu et al., 2005; Zuk and Matlin, 1996). Cells are firstly seeded onto a gel scaffold (2D), and then another gel layer is set by pouring gel solution onto the cells. After the gelation of the second layer, cells are covered by gel scaffold (3D). Epithelial sheets are known to respond to gel overlay, generating lumens after the second gel is overlaid, however, the process of this lumen formation is not fully understood.

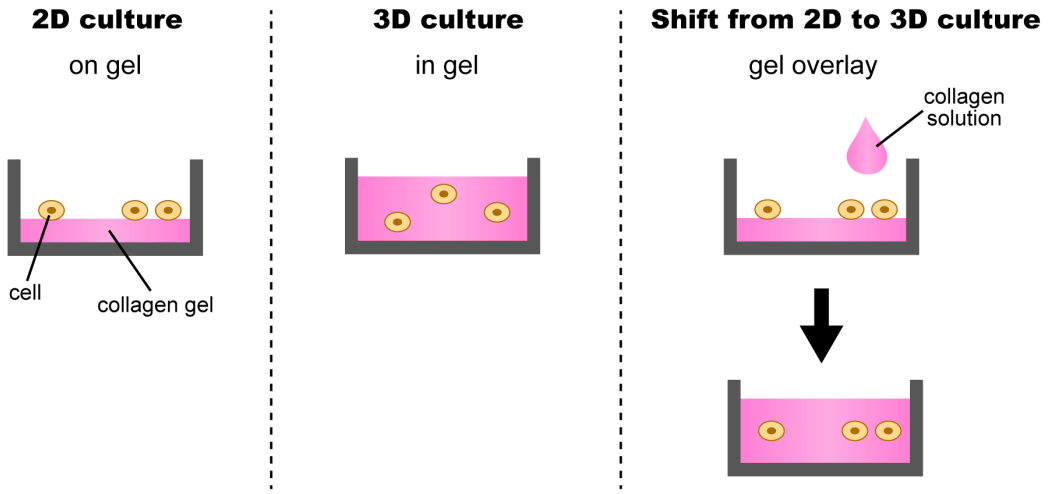

Figure 1.3 Culture Dimension for Cell Culture.

1-2-4. Structural Support of ECM

ECM provides the structural support to 3D morphologies (Rozario and DeSimone, 2010). Knock down of type-III and -V collagen decreases the assembly of type-I collagen, resulting in skin blisters and aortic rupture. Loss of type-IV collagen, β3- and γ2-laminin also leads to skin blistering. Furthermore, there is a case that structural integrity of ECM works as a clamp during morphogenesis (Diaz-de-la-Loza et al., 2018). In the development of *Drosophila* wings, epithelial cells are compacted with a cover of ECM. When the ECM is degraded, the sheets initiate to expand and result in the appearance of adult wings. Like these, the structural contribution of ECM is crucial for morphogenesis.

1-2-5. Mechanical Contribution of ECM

Mechanical properties of ECM regulate the cell behaviors. An example of elastic contribution to morphogenesis is the development of *Drosophila* egg chamber (Chen et al., 2019). This development starts from a round shape and the egg chamber becomes elongated as the development proceeds. In round phase, the elasticity of ECM (basement membrane) is isotropic. As the development proceeds, the elasticity becomes anisotropic and this lead the elongation of the organs. When the asymmetry of the elasticity is inhibited, the organs remain round. The elastic contribution of morphogenesis is also observed in *in vitro* studies (Miroshnikova et al., 2011; Paszek et

al., 2005). The colonies of mammary epithelial cells create spherical structure in soft gel (around 150 Pa), which is similar to *in vivo* normal mammary acinus. On the other hand, the colonies embedded in stiff gel (around 1400 Pa) lack the spherical shapes and obtained a disrupted morphology like tumors.

Compared with elastic contribution, only a few studies have been reported the viscous contribution to cellular behavior. Imai *et al.* modulated the viscosity of Matrigel with a low cytotoxic crosslinker genipin (see section 1-3-4) and reported morphological change of MDCK colonies (Imai et al., 2015). The colonies exhibit the tulip-hat like morphology on Matrigel with lower viscosity and they become flat with higher viscosity.

In addition to morphogenesis, the viscoelasticity of substrate is reported to regulate the collective cells migration. MDCK cells move randomly on stiff glass (2~3 GPa) with collagen coating but show directed migration on soft collagen gel (about 600 Pa) (Haga et al., 2005; Mizutani et al., 2006a). Murrell and his colleagues showed that the movement of mouse mammary epithelial cells is correlated on viscosity of the substrate (Murrell et al., 2011). As described above, the viscoelastic properties of ECM play an important role in morphogenesis and also in collective cell migration.

1-3. Key Factors and Molecules

1-3-1. Cell Contraction (Myosin)

Cells generate contractile force for many cell activities, such as cell migration, cell shape change and cell division. Cellular traction force is generated by actomyosin, which is composed of actin filaments (F-actin) and myosin II (Figure 1.4A)(Cooke, 1995; Vicente-Manzanares et al., 2009). Myosin II is the motor protein that interacts with F-actin to exert the traction force. Myosin II is comprised of three pairs of peptides, two heavy chain, two essential light chains, and two regulatory light chains (MRLCs) (Figure 1.4B). The head domains of heavy chains have binding domain to both F-actin and ATPs and they pull the F-actin with the consumption of ATPs. The head domain is followed by the neck domain, which contains the binding sites for the two kinds of light chains. The neck domain bends and amplifies the head stroke to pull the F-actin. The neck domain is followed by the long α-herical coiled-coil domain (tail domain), which dimerize the pair of heavy chains. The essential light chains stabilize the heavy chain structure, and MRLCs regulates the contractile force by the phosphorylation of Ser19, Thr18, or both (Figure 1.4C). Ser19 is known to phosphorylated prior to Thr18. Di-phosphorylated MRLC (2P-MRLC) induces stronger force than mono-phosphorylated MRLC (1P-MRLC) (Mizutani et al., 2006b). The several kinases have been reported to phosphorylate MRLC, such as Rho-associated, coiled coil-containing kinase (ROCK) (Ueda et al., 2002), citron kinase, myosin light chain kinase (MLCK) (Somlyo and Somlyo, 2003) and leucine zipper interacting kinase (ZIPK) (Murata-Hori et al., 1999). These kinases are activated in different pathway, for example, the small GTP-binding protein RhoA activate ROCK and citron kinase, Ca^{2+}-calmodulin activates MLCK.

Contraction by myosin activity is necessary for epithelial sheet deformation and cell migration (for migration, see the section below). During the folding deformation, apical of the cells shrinks by myosin contraction, showing the stronger phosphorylated MRLC localization on apical side (Martin and Goldstein, 2014). For example, 2P-MRLC localizes at the apical surface of folding epithelial sheet during the crypt formation in intestine and the inhibition of myosin prevents the sheet folding (Sumigray et al., 2018). Thus, contraction of actomyosin is a basic factor for sheet deformation.

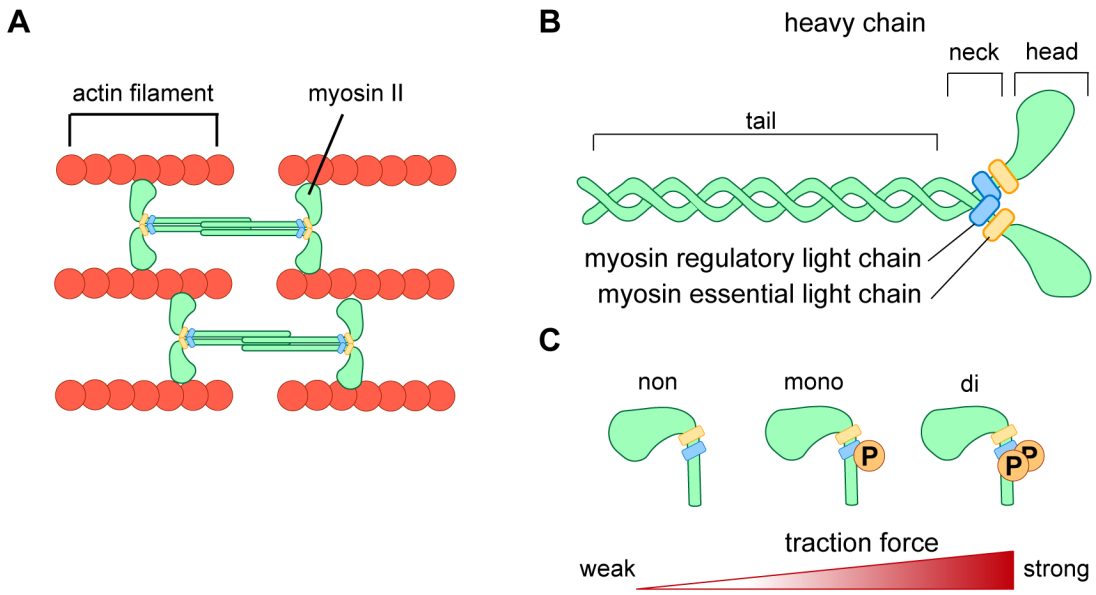

Figure 1.4 Cellular Contraction Generated by Actomyosin

(**A**-**B**) The schematic view of actomyosin (A) and myosin II (B). (**C**) The regulation of actomyosin contraction by phosphorylation of MRLC.

1-3-2. Cell Migration (Integrin, Rac)

Collective cell migration occurs when two or more cells move together with keeping cell-cell junctions. Whereas the cell cohesion exists, collective cell movement retains the cyclical process of single cell migration; a cell extend protrusion of the leading edge by Rac activation, followed by attachment of the leading edge to the substrate with integrins, and actomyosin contraction of the migrating tail (Figure 1.5) (Ilina and Friedl, 2009).

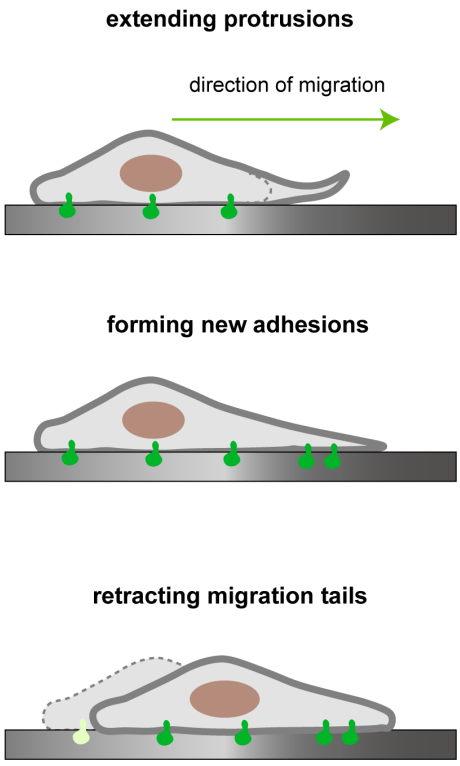

Figure 1.5 The processes of single cell migration

Integrins are a large family of heterodimeric transmembrane proteins, contributing to the adhesion between cells and ECM (Hynes, 2002). The heterodimers are composed of a pair of α and β chains. 19 α chains and 8 β chains have been identified (Caswell et al., 2009). The combination of the α and β chains determines the affinity to specific ECM proteins (Humphries et al., 2006). Integrins are regulated by both biochemical and mechanical signaling. Biochemical signaling is classified into two categories; inside-out and outside-in signaling (Figure 1.6). Inside-out signaling is the regulation by molecular interaction between integrin's cytoplasmic domains and scaffold proteins, such as talin and kindlin. For example, when talins, scaffold proteins to link integrin β-subunit to actin filaments, bind to integrin cytoplasmic tails, integrins shift their conformation from inactive (bent closed form; low affinity to ECM) to active (extended open form; high affinity to ECM) state. Another major effector of inside-out signaling is kindlin. The binding of kindling to integrin β-subunit supports the activation of integrin and recruit an important focal adhesion component, paxillin. This nascent adhesion activates Rac1 and mediates cell spreading. In contrast to inside-out

signaling, outside-in signaling start from integrin's engagement with ECM. When the extracellular domain of integrins connects to ECM, the cytoplasmic domain initiates accumulation and activation of scaffold proteins, such as focal adhesion kinase (FAK), talin and vinculin and small GTPases of the Rho family. In addition to biochemical signaling, mechanical regulation of integrins are recently well studied (Kechagia et al., 2019). Because integrins connect ECM and cell cytoskeleton, integrins have a role to transmit forces between ECM and cells. As such, integrins are positioned as a sensor of mechanical signaling. Once force is applied to integrins through the binding with ECM, the force opens the integrins to active conformation. In addition to this, force triggers talin's unfolding and subsequent vinculin binding, a linker between talin and actin fibers. These result in the maturation of the adhesion. The maturation promotes actin polymerization, which directly affect the nuclear localization and function of transcription factors, such as YAP/TAZ (Yes-associated protein/transcriptional coactivator with PDZ binding motif) (Dupont et al., 2011). Thus, integrins transduce biochemical/mechanical signaling between cytoplasmic and extracellular proteins to regulate cellular behaviors.

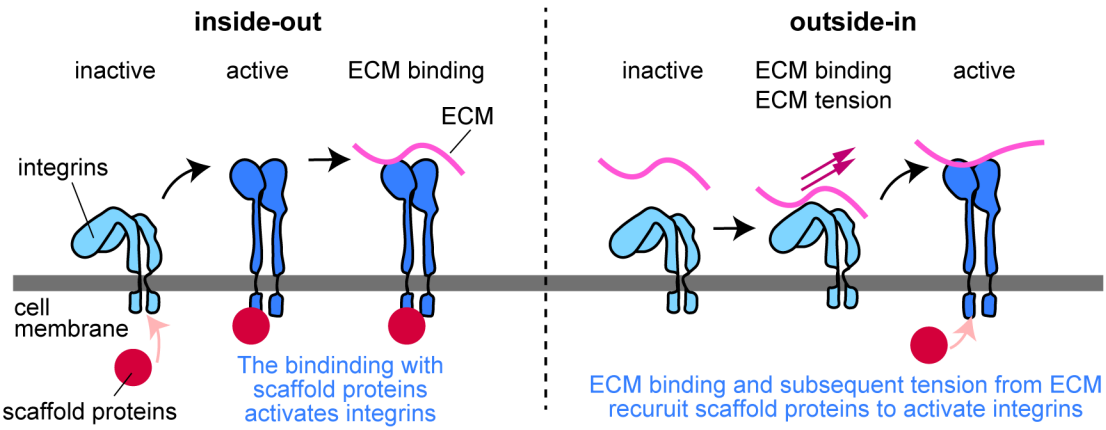

Figure 1.6 Inside-out and Outside-In signaling of Integrins.

Integrin-β1 plays crucial roles in collective cell migration. Integrin-β1 is upregulated at the leading edge of collective migration to promote the migration (Kato et al., 2014; Yamaguchi et al., 2015). In addition of adhesion to surrounding substrates, a few studies reported that integrin-β1 mediates cell-cell interaction during collective cell migration (Hegerfeldt et al., 2002). A431 cutaneous squamous carcinoma cells

(SCCs) shows collective cell migration when surrounded in collagen gel, and the blockage of integrin-β1 leads the loss of cell-cell cohesion, resulting in cell detachment and single cell migration (Kumagai et al., 2019).

Rac is a subfamily of the Rho family of GTPases, which is activated by GTP-binding and inactivated by GDP-binding (Ridley, 2001; Ridley, 2015). Rac plays a key role in lamellipodia extension. Rac regulates the F-actin accumulation at the migrating edge, leading the formation of branched actin filaments. When the Rac is inhibited, collective cell migration is prevented. The *in vivo* examples include that collective migration of border cells in *Drosophila* (Wang et al., 2010), endoderm cells in mouse embryo (Migeotte et al., 2010), and mesodermal cells in *Xenopus* gastrulation (Hayashi et al., 2018). *In vitro*, MDCK cells on collagen gel also require the active Rac for collective cell migration (Yamaguchi et al., 2015). During the collective migration of MDCK cells, a cell with prominent lamellipodia (a leader cell) appears on the edge of an epithelial sheet and guides the collective migration with leading neighboring cells called follower cells (Haga et al., 2005; Omelchenko et al., 2003; Yamaguchi et al., 2015). Rac is activated within the leader cells, and inhibition of the Rac disrupts the collective migration. These demonstrate that the integrin-β1 and Rac1 is significant in collective cell migration.

1-3-3. Osmotic Stress (Aquaporin)

Osmotic pressure is the pressure to prevent the inward flow of the solvent across a semi-permeable membrane (Figure 1.7A). When the solutions with different concentration are separated by semi-permeable membrane, only the solvent, but not the solute, moves across the membrane from a lower to a higher concentration compartment. Osmotic pressure is defined as the pressure to get the water levels equal. Osmotic pressure occurs by the concentration of solutes. The types of solutes do not affect the intensity of osmotic pressure.

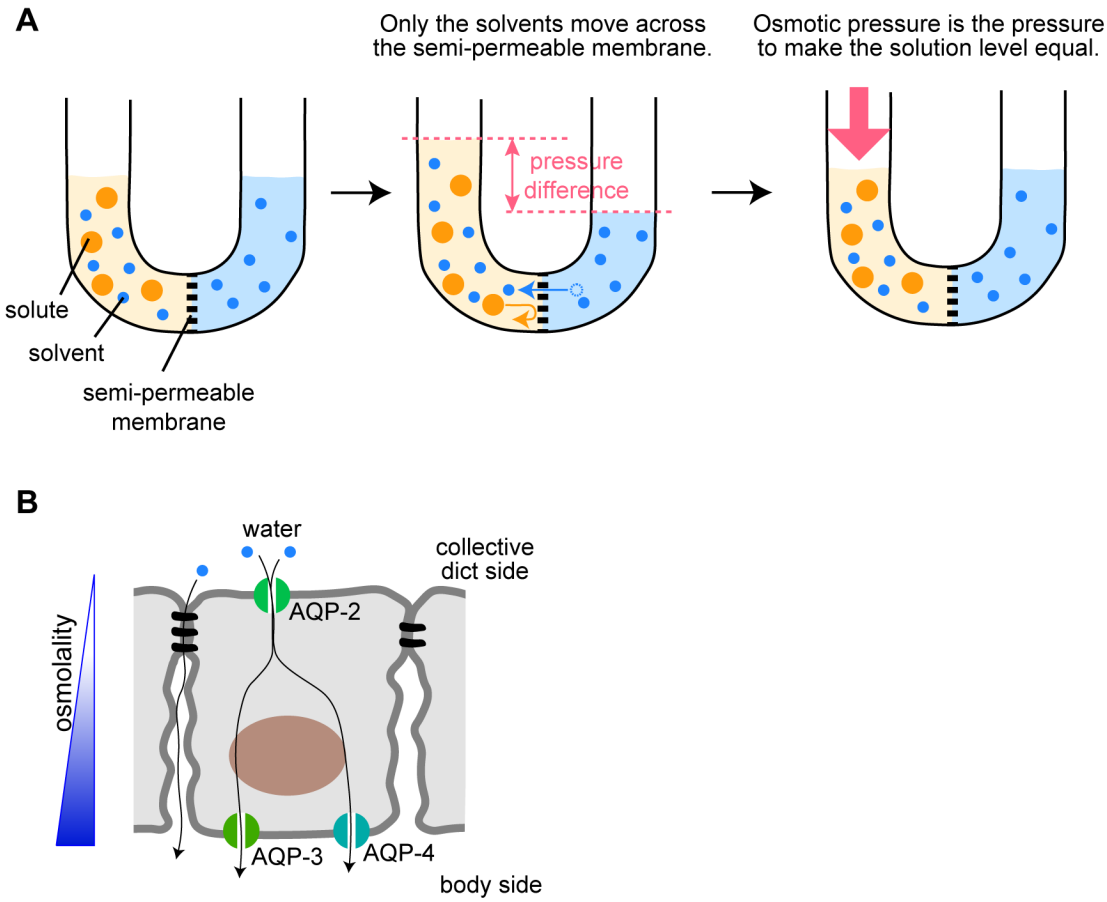

Figure 1.7 The Definition and Function of Osmotic Pressure.

(**A**) The definition of osmotic pressure. (**B**) The schematic view of the function of osmotic pressure to water reabsorption in kidney.

Cells and organs respond the osmotic gradient to keep the homeostasis. In the case of red blood cells, the cells in isotonic solution import and export the same amount of fluid, thus keep their cell volume (Raven et al., 2006). On the other hand, the cells in hypertonic solutions export more fluid from the cells, resulting in the decrease in cell volume. In hypotonic solution, more fluid comes into the cells and cells increase their volume. In organ level, epithelial sheets act as semi-permeable membranes because of epithelial barrier function (see section 1-1-3-1). In kidney, osmotic gradient between collecting ducts and body side leads water reabsorption to keep body homeostasis (Figure 1.7B)(Day et al., 2014). In intestine, the disruption of an osmotic balance leads diarrhea (Camilleri et al., 2017). Non-absorbable materials persist in the gut and increase the intratubular osmolality. This causes water flux into the intestinal tract,

subsequently leading diarrhea. From these, osmotic pressure is important for homeostasis.

Although the osmotic pressure during development is very little known, a few reports show the osmotic contribution to morphogenesis. Extension of the excretory canal in *Caenorhabditis elegans* (*C. elegans*) *in vivo* and branching morphogenesis in mouse lungs *ex vivo* are both stimulated by hypertonic stress (Figure 1.8)(Kolotuev et al., 2013; Nogawa and Hasegawa, 2002). Thus, it is possible that osmotic pressure contributes to various morphogenesis.

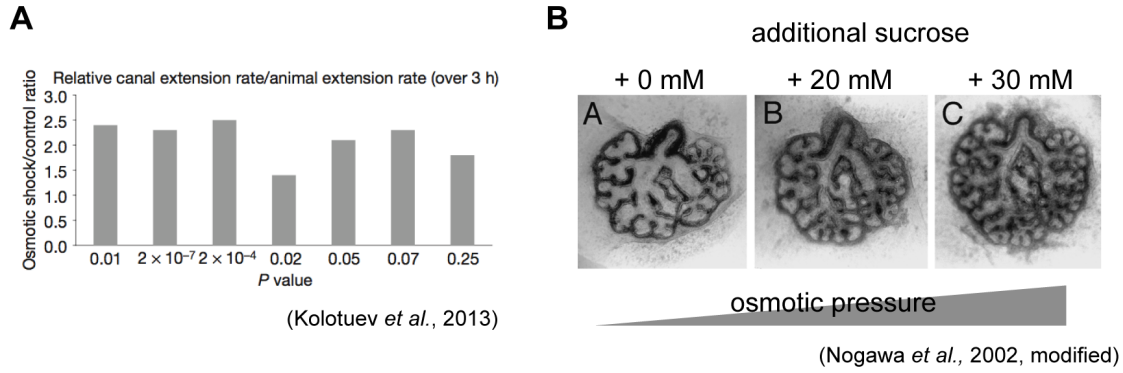

Figure 1.8 Osmotic Contribution to Morphogenesis

(**A**) Graph for the relative length of *C. elegans* canal tubes after hypertonic shock. (**B**) Images of mouse lung rudiments cultured in hypertonic medium by adding indicated sucrose.

Aquaporin (AQP) water channels are the membrane intrinsic protein to regulate osmotic water permeability of cells. 13 AQPs (AQP-0 ~ AQP-12) are identified in mammals (Verkman, 2011). There are classified into three subtypes; classic AQPs (AQP-0, -1, -2, -4, -5, -6 and -8), which are bidirectional water-selective channels with high flow rate; aquaglyceroporins (AQP-3, -7, -9 and -10), which transport both water and electroneutral small molecules, including glycerol and urea; unorthodox AQPs (AQP-11 and -12), which functions are not clear. AQP-6 is reported to also transport anion (Liu et al., 2005).

The monomer of AQP is ~30 kDa and has six membrane-spanning α-helical domains and two short helical segments that surround cytoplasmic or extracellular vestibules (Borgnia et al., 1999; Verkman, 2011). These vestibules are connected with a narrow path for water molecules. Water-selective AQP-1 has two water-selective filters

at the path; aromatic/arginine constriction region composed of Phe56, His180, Cys189 and Arg195 and asparagine-proline-alanine box. These two filters physically restrict the diameter of the path and prevent the electroneutral and proton molecules. Mercury is a broad inhibitor of AQPs, including AQP-1, -2, -3, and -5 (Deen et al., 1997; Horsefield et al., 2008; Ishibashi et al., 1994; Kuwahara et al., 1997; Mulders et al., 1997; Preston et al., 1993), while AQP-4, -6 and -7 was not inhibited with mercury (Ishibashi et al., 1994; Jung et al., 1994). Mercury interacts aromatic arginine constriction region (for example, Cys189 in AQP-1 (Preston et al., 1993)), causing structural change and blockage of the water path (Hirano et al., 2010).

Cells expressing AQPs have higher osmotic water permeability than cells not expressing AOPs. One important function of epithelial cells is fluid transport across the epithelial barriers. AQPs involves to this fluid regulation. In the case of kidney, AQP-1 and AQP-7 expressed in proximal tubule, and AQP-2, AQP-3 and AQP-4 expressed in collecting duct cells (Day et al., 2014). AQP-1 in proximal tubules is responsible for most water absorption and the mouse lacking AQP-1 have defect in water absorption (Schnermann et al., 1998). AQP-2 in collecting ducts adjusts the water balance by vasopressin regulation. AQP-3 and AQP-4 excrete the water to blood vessel when AQP-2 take water into collecting duct cells (Figure 1.7B). In the case of MDCK epithelial cells, which are derived from Dog kidney proximal tubes, expresses AQP-1, -2, -3 and -4 (Madrid et al., 2001; Matsuzaki et al., 2001; Noitem et al., 2018; van Balkom et al., 2003; Wang et al., 2015). AQP-2 localizes on apical membrane in highly expression level in isotonic condition, and it distributes to both apical and basolateral membrane with the exposure of long term hypertonicity (van Balkom et al., 2003). AQP-3 is upregulated and localizes basolateral membrane when cultured in hypertonic culture medium (Matsuzaki et al., 2001). Additionally, AQP-4 localizes on basolateral membrane cultured in isotonic condition (Madrid et al., 2001).

A few studies suggest AQP fluid regulation affects morphogenesis *in vivo* and *in vitro* (Figure 1.9). Overexpression of AQP-8 in *C. elegans* expands the lumen of the canal, which is rescued by mercury chloride ($HgCl_2$) (Khan et al., 2013). *In vitro*, overexpressing AQP-1 stimulates tubulogenesis in MDCK cells (Wang et al., 2015). Furthermore, in the presence of hydrostatic pressure, AQP-1 mediates water efflux and promotes tubulogenesis of endothelial cells via transient activation of Ras/ERK pathway (Yoshino et al., 2020). These observations indicate that AQP's fluid regulation

are involved in 3D shaping, however, large part of AQPs contribution to morphogenesis has been unexplored.

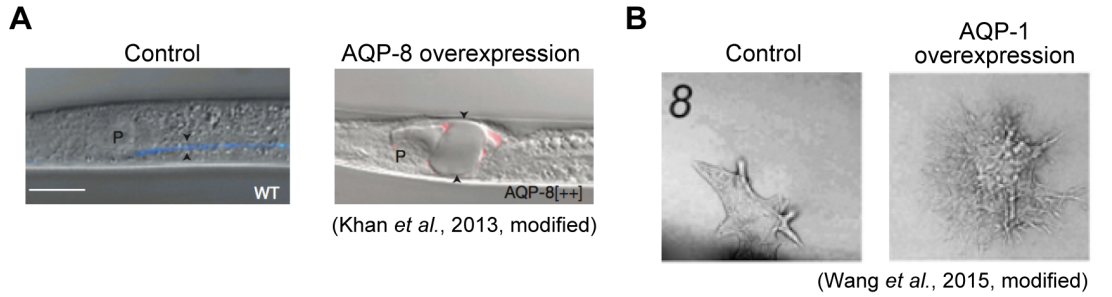

Figure 1.9 The AQPs contribution to morphogenesis.

(**A**) Images of disrupted canal tubes in *C. elengas* by overexpressing AQP-8. (**B**) Images of stimulated tubulogenesis of MDCK colonies by overexpressing AQP-1.

1-3-4. Crosslinker (Genipin)

Genipin (GP) is the naturally driven crosslinking regent, which is extracted from a plant, *Gardenia jasminoides* (Sung et al., 1998). GP attacks to primary amines of protein polymers and then the attached GP molecules dimerize to mediate the intramolecular and intermolecular cross-linkings (Figure 1.10)(Hwang et al., 2011; Sundararaghavan et al., 2008; Sung et al., 2003). GP cross-linkings modify the physical properties of various biomaterials; viscoelasticity of collagen (Sundararaghavan et al., 2008), viscoelasticity of chitosan gel (Gao et al., 2014) and viscosity of Matrigel (Imai et al., 2015) are increased after GP treatment. GP crosslinks show higher cell viability compared with other crosslinker, such as glutaraldehyde and epoxy (Gao et al., 2014; Muzzarelli et al., 2015; Sundararaghavan et al., 2008; Sung et al., 1998; Tsai et al., 2000).

GP crosslinks also exhibited the unique outcomes. The color of gel turns blue after GP crosslinks (Lee et al., 2003; Mi et al., 2000; Muzzarelli et al., 2015; Sundararaghavan et al., 2008; Takami and Suzuki, 1994). The blue becomes darker as the GP is treated more strongly (Muzzarelli et al., 2015). So far, the mechanisms of genipin-derived blue color are unclear. In addition of blue color, the crosslinks absorb the light of 590 nm wavelength (Lee et al., 2003) and emits strong red fluorescence (Excitation/Emission 510-560/590 nm, and Excitation/Emission 590/630 nm) (Hwang

et al., 2011; Muzzarelli et al., 2015; Sundararaghavan et al., 2008) in the case of collagen gel. An additional fluorescent emission is detected at 464 nm (Em 300-500 nm) in collagen and at 369 nm (Em 369 nm) in chitosan, which may due to different fluorophores generated by different GP access to amino acid residues within the ECM polymers (Chen et al., 2005; Hwang et al., 2011). The intensity of both absorbance and fluorescent shows the positive correlation to GP crosslinks increases, thus, the intensity is used as a barometer of the degree of GP crosslinks (Hwang et al., 2011; Sundararaghavan et al., 2008). Thus, GP has been used as effective tool to modify biomaterial culture scaffold.

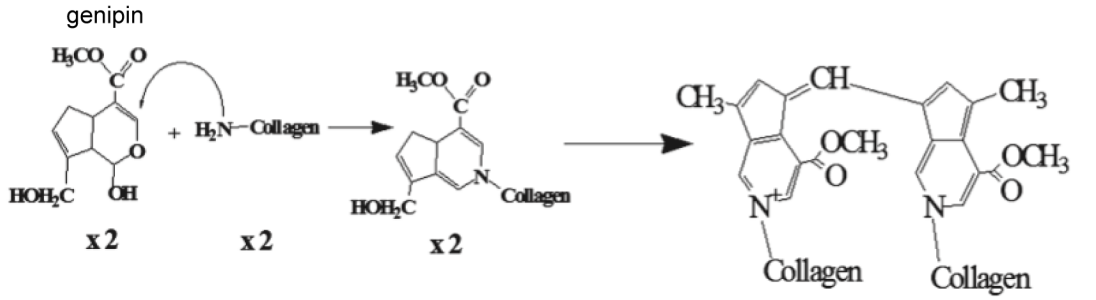

Figure 1.10 GP-collagen crosslinkings.

1-4. The Aim of This Study

Epithelial sheet deformation is an important cue in morphogenesis. Previous studies have reported that *in vitro* epithelial morphogenesis of lumens and domes involves sheet deformations. However, the factors to cause the cell sheet deformation in the morphogenesis have not been fully examined. In this study the lumen and dome formation were observed *in vitro* with the use of ECM, whose physical properties influences the morphogenesis. The observations were performed with focusing on epithelial characters, such as collective migration, apical-basal polarity and transporting activity.

Chapter 2

Materials and Methods

2-1. Sample Preparation

2-1-1. Regents and Cell Culture

Monoclonal antibody (mAb) AIIB2 (Hall et al., 1990), Rac1 inhibitor II, and Y27632 were used to inhibit integrin-β1, Rac1, and ROCK, respectively (For the information of the concentration used in this study, catalog numbers and the suppliers, see Table 2.1). Transforming growth factor (TGF)-β1 was used to disrupt apical-basolateral cell polarity. Roscovitine was used for the inhibitor of cell proliferation. $HgCl_2$ was used to prevent AQPs water transport. Cytochalasin D and blebbistatin (+/-) were used to inhibit actomyosin.

Antibodies used for immunofluorescent staining were as follows: anti-pig collagen for collagen gel; Phospho-MRLC (Thr18/Ser19) rabbit IgG for di-phosphorylated MRLC (2P-MRLC); Phospho-MRLC (Ser 19) rabbit IgG for mono-phosphorylated MRLC, (1P-MRLC); Tri-Methyl-Histone H3 (Lys4) (C42D8) rabbit mAb for nuclei; p-histone H3 (S10) rabbit mAb (p-Histone) for nuclei in cell division; anti-gp135 for gp135; rr1 for E-cadherin; and AIIB2 for integrin-β1. Alexa Fluor-594-labeled goat anti-mouse IgG (H+L), Alexa Fluor-594-labeled donkey anti-rat IgG (H+L), Alexa Fluor-594-labeled goat anti-rabbit IgG (H+L), goat anti-rabbit Alexa Fluor-488 superclonal antibody were used as secondary antibodies. F-actin was stained with Alexa Fluor-488 phalloidin or Alexa Fluor-647 phalloidin. For nuclei staining, DAPI, Hoechst 33342, Syto9 green fluorescent nucleic acid stain were used. Calcein-AM was used to stain live cells.

Antibodies used in western blot were as follows: anti-phospho-MRLC (Ser 19/Thr 18) rabbit IgG, anti-phospho-MRLC (Ser 19) rabbit IgG, and anti-GAPDH mAb for primary antibodies; anti-rabbit IgG HRP-linked antibody and anti-mouse IgG HRP-linked antibody were used for secondary antibodies.

Dulbecco's Modified Eagle's Medium (DMEM) was supplemented with 10% bovine fet al serum (FBS) and 1% antibiotics and antimycotics for cell culture. In chapter 4, this culture medium was used as isotonic DMEM (I-DMEM). Hypertonic DMEM (H-DMEM) was prepared with the addition of mannitol (133-00845, FUJIFILM Wako Pure Chemical Corporation) to I-DMEM at the concentration of 200 mM. The absolute osmolality was determined by a cryoscopic osmometer (OSMOMAT 030; Gonotec, Berlin); I-DMEM and H-DMEM were 298 (± 2.5 S.D.) mOsm per kg

H_2O and 441.6 (± 26.5 S.D.) mOsm per kg H_2O, respectively. To prepare the H-DMEM of different solutes, glycerol (G5516, Sigma-Aldrich) or sucrose (196-00015, FUJIFILM Wako Pure Chemical Corporation) was added to I-DMEM at the concentration of 200 mM. When the name and the concentration of solute were not mentioned, the H-DMEM was supplemented with 200 mM mannitol. We also prepared hypotonic DMEM by diluting I-DMEM with the distilled water (water: I-DMEM = 1:2). Cell matrix type IP and Cell matrix type IC were used for collagen gel and collagen coat, respectively. Matrigel and Matrigel High Concentration (Matrigel HC) were used as gel and coat. Matrigel was treated with GP when indicated. Fibronectin was used for coating.

Table 2.1 Reagents used in this study

Regents	concentration	Catalog Number	Suppliers
Inhibitors			
AIIB2	100 ng/mL		The Developmental Studies Hybridoma Bank at University of Iowa
Rac1 inhibitor II	100 μM	Z62954982	Calbiochem
Y27632	10 μM (chapter 3) 20 μM (chapter 4)	Y0503	Sigma-Aldrich
TGF-β1	1.5 ng/mL	1210209 F2011	PeproTech Inc.
Roscovitine	100 μM (chapter 3) 10 μM (chapter 4)	R7772	Calbiochem
$HgCl_2$	100 μM	130-01151	FUJIFILM Wako Pure Chemical Corporation
Cytochalasin D	5 μM	BML-T109-0001	COSMO BIO CO., LTD
Blebbistatin (+/-)	100 μM (chapter 3) 20 μM (chapter 4)	 BML-EI315-0005	Gift from Dr. M. Takahashi (Hokkaido University) (chapter 3) COSMO BIO CO., LTD (chapter 4)
Fluorescent staining			
Anti-pig collagen I and III	1:20 diluted	PS067	MONOSAN
Phospho-MRLC (Thr18/Ser19) rabbit IgG	1:100 diluted	#3674	Cell Signaling Technology

Phospho-MRLC (Ser19) rabbit IgG	1:100 diluted	#3671	Cell Signaling Technology
Anti-gp135	1:300 diluted		Gift from Dr. G. Ojakian (SUNY Downstate Medical Center)
rr1	1:200 diluted		The Developmental Studies Hybridoma Bank at University of Iowa
AIIB2	1:100 diluted		The Developmental Studies Hybridoma Bank at University of Iowa
Tri-Methyl-Histone H3 (Lys4) (C42D8) rabbit mAb	1:4000 diluted	9751S	Cell Signaling Technology
p-histone H3 (S10) rabbit mAb	1:1000 diluted	9701S	Cell Signaling Technology
Alexa Fluor-594-labeled goat anti-mouse IgG (H+L)	1:500 diluted	A-11005	Invitrogen
Alexa Fluor-594-labeled goat anti-rat IgG (H+L)	1:500 diluted	A-21209	Invitrogen
Alexa Fluor-594-labeled donkey anti-rabbit IgG (H+L)	1:500 diluted	A-11012	Invitrogen
goat anti-rabbit Alexa Fluor-488 superclonal antibody	1:500 diluted	A27034	Invitrogen
Alexa Fluor-488 phalloidin	1:500 diluted	A12379	Thermo fisher Scientific
Alexa Fluor-647 phalloidin	1:100 diluted	A12379	Thermo fisher Scientific
DAPI	Unknown		Gift from Dr. Ushiki and Dr. Hoshi, Niigata University
Hoechst	2 μg/mL or 10 μg/ml	14533	Sigma-Aldrich
Calcein-AM	1 μM	C396	DOJINDO LABORATORIES

Syto9 green fluorescent nucleic acid stain	10 μM	S34854	Thermo Fisher Scientific
Western Blot			
Phospho-MRLC (Thr18/Ser19) rabbit IgG	1:2000 diluted	#3674	Cell Signaling Technology
Phospho-MRLC (Ser19) rabbit IgG	1:1000 diluted	#3671	Cell Signaling Technology
Anti-GAPDH mAb	1:5000000 diluted	AM4300	Invitrogen
1:10000 diluted anti-rabbit IgG HRP-linked antibody	1:10000 diluted	#7074	Cell Signaling Technology
1:50000 diluted anti-mouse IgG HRP-linked antibody	1:50000 diluted	#7076	Cell Signaling Technology
Cell Culture			
Dulbecco's Modified Eagle's Medium (DMEM)		D6046	Sigma-Aldrich
Bovine fetal serum (FBS)			Equitech-Bio. Inc
		172912	Sigma-Aldrich
antibiotics and antimycotics		A5955	Sigma-Aldrich
Cell Matrix Type IP		KP-3100	Nitta Gelatin. Inc
Cell Matrix Type IC		KP-4100	Nitta Gelatin. Inc
Matrigel Growth Factor Reduced		354230	Corning
Matrigel High Concentration		354248	Corning
Fibronectin		063-05591	FUJIFILM Wako Pure Chemical Corporation
Genipin	Indicated in the text	078-03021	FUJIFILM Wako Pure Chemical Corporation

2-1-2. Cell Culture

Canine kidney epithelial cells (MDCK cells) were purchased from RIKEN BRC through the National BioResource Project of the MEXT/AMED, Japan. MDCK cells were not authenticated. Mycoplasma contamination was not detected. Wild type MDCK (MDCK-WT) cells were cloned by limiting dilution, and subclonal cell line (MDCK-2) was established (by Kentaro Umeno). MDCK-2 cells were transfected with a phmAG1-H-Ras-CAAX vector and a stable cell line (MDCK-CAAX) was established (Appendix 1; performed by Mr. Naoya Yamaguchi). Cells were maintained with culture medium at 37 °C in a humidified incubator with 5% CO_2.

2-1-3. Gel Overlay Assay

1.6 mg/mL collagen type I gel consisting of Cellmatrix type I-P was used to make collagen gel. First, hand-made glass dish with a diameter of an 8.0 or 12.5 mm was filled with 150 or 300 μl of the collagen gel, respectively, onto which trypsinized cells ($1.0x10^3$ or $2.0x10^3$, respectively) were seeded. After culture for 4 or 5 days, gel solution (equal in volume to the first gel layer) was poured onto the cell. For collagen overlay, collagen gel solution was poured onto the cells and incubated for 30 min at 37°C for gelation. For Matrigel overlay, liquified Matrigel was poured and incubated for gelation. For agarose gel overly, 0.8% agarose gel solution was kept at 40°C and poured onto cells and incubated at room temperature for gelation. After gelation, the dish was then filled with culture medium.

To observe the migration rate of epithelial cells during lumen formation, an epithelial sheet with constant shape was generated on collagen gel. A plastic circular cylinder (1.5 mm radius) was glued to a 5 mm radius glass coverslip. A hole was opened in the coverslip along the inside edge of the cylinder. A handmade glass dish of 12.5 mm radius was filled with 300 μl of collagen gel. Before the dish was filled with culture medium, the cylinder was placed onto the center of the collagen gel. Culture medium was added outside of the cylinder and then MDCK cells were seeded into the cylinder. After incubated overnight, the cylinder was removed gently to reveal an epithelial sheet on the collagen gel. To observe the gel deformation, 2.0 mm latex beads (Polysciences, Inc.) were embedded to the collagen gel. Coverslips coated with collagen type I (1:10 diluted Cell matrix I-C) served as glass surfaces.

2-1-4. Preparation of Genipin-treated Matrigel (GP-Matrgiel)

Liquified Matrigel was mixed well with GP solution on ice at the final concentration of 1.0, 0.75, 0.63, 0.50, 0.25, and 0.13 mM, respectively. 35 μL and 105 μL of the mixture was poured into a 24-well and 12-well transwell inserts with 0.4 μm pore size (353095 and 353180, CORNING), respectively and incubated for 48 or 72 h at 37°C for gelation and cross-linking. After the gel is rinsed by DMEM (non-serum, non-antibiotics), the cells were seeded for experiments. If the concentration of GP was not mentioned, 0.63 mM GP-Matrigel was used. To measure the absorbance of GP crosslinking, 100 μL of GP-Matrigel was prepared to each well of a 96-well plate (TR5003, NIPPON Genetics Co., Ltd). The absorbance at 595 nm wavelength was measured by a plate reader (iMark, Bio-Rad). The fluorescence of GP crosslinking was observed by confocal laser-scanning microscopy (A1 confocal imaging system; Nikon Instech) at an excitation wavelength of 561 nm and an emission wavelength of 604 nm. The fluorescence intensity was determined using ImageJ (National Institutes of Health). For the experiments with atomic force microscopy, 800 μL GP-Matrigel was prepared on a 35 mm dish.

2-1-5. ECM Preparation and Osmotic Stress Treatment

Matrigel and Matrigel HC were stored at -20°C and thawed overnight at 4°C before use. For ECM coating, Matrigel and fibronectin were diluted with ice-cold PBS, poured into 24-well transwell insert and incubated at 4°C overnight. To prepare gel substrate, 100 μL of Matrigel or Matrigel HC was poured into hand-made glass dish and incubated at 37°C for gelation. Collagen gel was prepared with Cellmatrix type IP at the concentration of 1.6, 1.2, 0.75, 0.36 mg/mL. If not mentioned, 1.6 mg/mL of Cellmatrix type IP was used as collagen gel. To mix Matrigel and collagen gel, each gel solution was mixed on ice at indicated mixing ratio and then gelated at 37°C for 30 min. For osmotic treatment, 30 μl of the gel was set to 24-well transwell inserts with 0.4 μm pore size (353095, CORNING).

The trypsinized cell suspension (2.0×10^5 cells or 4.0×10^5 cells) was seeded onto a permeable membrane (with and without ECM coat) or ECM gel in a 24-well transwell insert, respectively. After cells become the tight confluent, cells were incubated with osmotic stress. After removal of the culture medium, 500 μL of I-DMEM and 1000 μL of H-DMEM was added to the apical side and basal side of the

chamber in the 24-well plate, respectively (basal hypertonic stress, bHS). For control, 1000 μL of I-DMEM was added to the basal side of the chamber (isotonic stress: IS). Then cells were incubated at 37°C. For long-term culture with osmotic stress, the medium of both apical side and basal side was renewed about every 24 h. To make subconfluent cell sheets on GP-Matrigel, 1.0 x 10^5 cells were seeded to 24-well transwells. A day after seeding, cells were exposed osmotic stress.

2-2. Sample Observation

2-2-1. Phase-contrast Images and Time-lapse Observations

Phase-contrast images were taken by a phase-contrast microscope (TE300 or TE2000, Nikon Instech), equipped with a 10x or a 4x objective. Image-Pro software (Media Cybernetics Inc.), WraySpect software or Q-Capture Pro software was used for still images and time-lapse observations, respectively. Wide-field images were taken using a digital camera (EX-ZR1800, CASIO COMPUTER CO., LTD.) from an eyepiece lens of the microscope.

For time-lapse observations in chapter 3, the handmade glass dish was filled with culture medium containing 5% CO_2 immediately after gel overlay. Then the dish was sealed with silicone grease to keep the pH of the medium. In chapter 4, a 24-well transwell insert was set to the handmade glass bottom dish with the same radius and height of a 24 well. I- and H-DMEM was incubated in 5% CO_2 in advance. Immediately after the osmotic stress was applied to cells, the insert was sealed with mineral oil (M5904, Sigma-Aldrich) to keep the pH of the medium. In both chapter 3 and 4, the microscope was maintained at 37°C in an acrylic resin box. Phase contrast images were taken every 2.5 min or 5 min, and the images were edited to create movies.

2-2-2. Confocal Observation and 3D Live Imaging

In chapter 3, MDCK-CAAX cells were observed with a confocal laser scanning microscope (TCS-SP5; Leica Microsystem CMS GmbH) coupled to a Leica DMI6000 CS microscope. Cells cultured with collagen gel containing the latex beads were imaged using a confocal laser scanning microscope (A1R Confocal Imaging System, Nikon Instech.). The TCS-SP5 or A1R were maintained at 37 °C. Images were captured at 20 min or 10 min intervals for TCS-SP5 or A1R, respectively.

In chapter 4, non-transfected MDCK cells (MDCK-WT cells) were stained with Calcein-AM in I-DMEM at 37°C for 30 min. The transwell insert was placed to a handmade glass bottom dish and fluorescence images were obtained by using the Nikon A1 confocal microscopy. For 3D live imaging, MDCK-CAAX cells were seeded on a GP-Matrigel embedded with fluorescent beads (I-7221, Invitrogen). Immediately after the osmotic treatment was started, the insert was sealed with mineral oil and maintained at 37°C by STX (TOKAI HIT). Images were taken every 10 min.

2-2-3. Fluorescent Staining

In chapter 3, cells were fixed with 1% or 2% paraformaldehyde in phosphate-buffered saline (PBS) for 10 min for 2P-MRLC or other proteins, respectively. The samples were permeabilized with 0.5% Triton-X100 in PBS for 10 min, and then blocked with 0.5% skim milk (Megmilk Snow Brand Co., Ltd.) in PBS for 2P-MRLC or with 0.5% bovine serum albumin (Sigma-Aldrich) in PBS for other proteins. Samples were incubated with primary antibody overnight at 4 °C for nuclei or at room temperature for other proteins. The appropriate secondary antibody and Alexa Fluor-488 phalloidin were then added for 3 h at room temperature. For nucleus staining, cells were incubated with DAPI at 37 °C for 1 h. The fluorescent images were captured using a confocal laser scanning microscope (C1 confocal Imaging System (Nikon Instech.) or A1R Confocal Imaging System).

In chapter 4, cells were fixed with 4% paraformaldehyde in PBS, permeabilized with 0.5% Trion X-100 in PBS, and stained with Hoechst 33342 and Alexa Fluor-647 phalloidin in PBS for overnight at 4°C. For phosphorylated MRLC staining, cells were blocked with 0.5% skim milk in PBS after permeabilization and incubated with primary antibodies at room temperature for 2 days. The primary antibodies used were anti-phospho-MRLC (Ser 19) rabbit IgG and anti-phospho-MRLC (Thr18/Ser19) rabbit IgG. Cells were then incubated with goat anti-rabbit Alexa Fluor-488 superclonal antibody and Alexa Fluor-647 phalloidin at room temperature for 2 days. Because the sample was too large to observe cells due to the focal distance of a high magnification objective lens, stained sample was gently removed from the insert and inverted on a glass coverslip. Fluorescence images were captured using Nikon A1 confocal microscopy.

2-3. Analysis

2-3-1. Analysis of Migration Velocity

To analysis the migration velocity of epithelial cells, time-lapse images were taken after collagen gel overlay. The folded area (*S*) and the outer perimeter (*P*) of the epithelial sheet were calculated using Image Pro software (Figure 2.1A). The average distance from the outer periphery to the leading edge was calculated using the equation *S/P*. The distance was plotted as a function of the observation time, a linear approximation was applied, and the slope was defined as the migration velocity. To calculate the migration velocity of epithelial cells on a glass surface, an epithelial sheet was made on a collagen-coated glass coverslip using a cylinder. After the cylinder was gently removed, time-lapse images of cell migration were captured. The area of migration (*S*') and the length of the epithelial sheet in the vertical plane (*L*) were measured (Figure 2.1B). The average migration distance was calculated using the equation *S'/L*. The migration velocity was estimated by plotting the distance as a function of time.

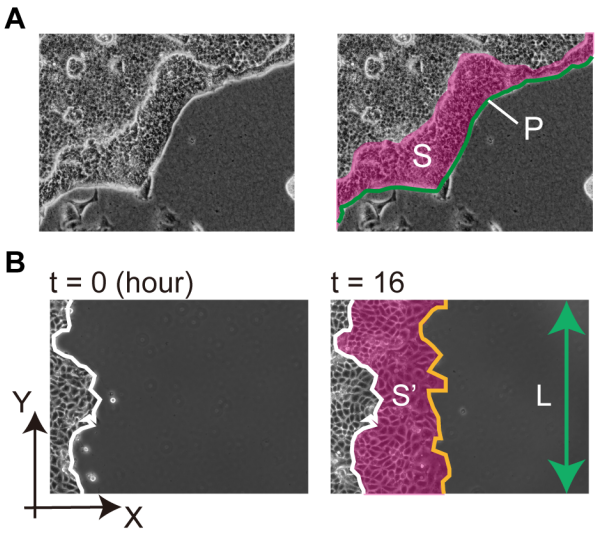

Figure 2-1. Measurement of the migrating area and the outer perimeter to determine migration velocity.

(**A**) The phase-contrast image on the left represents the raw data and that on the right shows the measurement example. *S*, indicated by the pink area, represents the folded area. *P*, indicated by the green line, represents the outer perimeter of the epithelial sheet. (**B**) Images represent cell migration

on glass. Two black arrows denote the *X*-axis and *Y*-axis, respectively. The white line represents the migrating edge at the beginning of the observation. The orange line denotes the migrating edge at the indicated time point. *S'*, indicated by the pink area, represents the migrating area. *L*, indicated by the green arrow, represents length of the MDCK sheet in the *Y*-axial direction.

2-3-2. Analysis of Osmotic Tolerance

To measure the osmotic tolerance of cells, MDCK-2 cells (2.0 x 10^5) were seeded onto non-coated glass with a diameter of 1.6 mm and incubated overnight with various osmotic pressure. For hypotonic stress, I-DMEM was diluted with sterile pure water. For hypertonic stress, mannitol was added to I-DMEM this the indicated concentrations. For positive control, cells cultured in I-DMEM were exposed to UV light in a clean bench for 15 min, and then incubated at 37°C overnight. After the incubation, cells in each condition were trypsinized and suspended. The suspension was mixed with 0.4% trypan blue solution (5250061, Thermo Fisher Scientific) at a ratio of 1:1, and the number of live cell and dead cells were counted with Countess II (Thermo Fisher Scientific), respectively.

2-3-3. Viscosity Measurement of GP-Matrigel

To measure the viscosity of GP-Matrigel, a stainless ball was dropped into the GP-Matrigel. This experiment is referred as the ball dropping analysis hereafter. The mixture of GP and Matrigel was poured into a plastic cylinder with the radius of 1.5 mm and with the height of approximately 50 mm. The mixture was incubated at 37°C for gelation and GP-crosslinking. After the incubation, a stainless ball was dropped onto the upper surface of GP-Matrigel. The cylinders were subsequently filled with DMEM (non-serum, non-antibiotics) and sealed with mineral oil. The cylinders were kept at 37°C in an acrylic resin box. Time-lapse images were captured with a camera every 10 min for 48 h. For 0.25 mM GP-Matrigel and control (0 mM), fall velocities (v) was estimated from a linear approximate equation of the displacement-time graph and calculated viscous moduli (η) using the following equation:

$$\eta = \frac{2}{9} \cdot \frac{r^2(\rho_2 - \rho_1)g}{v},$$

where r is radius of stainless ball, ρ_1 and ρ_2 represent the density of the Matrigel and the stainless ball, respectively, and g is the acceleration of gravity, and their values are

as follows, r = 1.0 x 10^{-3} m, ρ_1 = 1.1 x 10^3 kg/m^3, and ρ_2 = 7.9 x 10^3 kg/m^3, and g = 9.8 m/s^2.

To observe whether plastic deformation occurs in GP-Matrigel, a stainless ball was removed from the GP-Matrigel. This experiment was referred as ball removing analysis hereafter. 100 μL GP-Matrigel was prepared into a hand-made glass bottom dish with a diameter of 7 mm. The stainless ball was dropped onto the surface of GP-Matrigel and incubated for 2 days and then gently removed. The sample was maintained at 37°C and the surface shape was observed with the A1 confocal microscope every day.

To determine the relaxation time of GP-Matrigel, GP-Matrigel was prepared in the same way of ball removing analysis. A stainless ball was placed on the surface of each GP-Matrigel with various contact time and then the ball was gently removed. Immediately after the removing, the surface shape was captured with the A1 confocal microscope.

2-3-4. Analysis of Gel Swelling

The center part of GP-Matrigel was observed by the A1 confocal microscopy. Then the gel was exposed to osmotic stress or immersed in pure water. After overnight incubation at 37°C, the center part of the gel was captured again, and its volume was measured by ImageJ software.

2-3-5. Analysis of Water Transport

To measure the transcellular water flow, we referred to a spectroscopic method developed by Jovov *et al*. (Jovov et al., 1991). The same number of cells (4.0 x 10^5) were seeded onto GP-Matrigel in 24 well transwell with 0.4 μm pore. After the cell sheet became tight confluent, apical and basal compartment of the transwell was rinsed with PBS. The apical compartment was filled with 250 μL of I-DMEM supplemented with additional phenol red (P3532, Sigma-Aldrich) at final concentration of 224 μM. Basal compartment was filled with 500 μL of phenol red-free I-DMEM or phenol red-free H-DMEM. After incubated for 9 h, all the apical and basal medium was separately collected. After the weight of each medium was measured, the medium was centrifuge at 15,000 rpm for 30 s. The supernatant was collected to new tube to remove cell debris. Then absorbance at absorbency at 479 nm (A479), the isosbestic point for

phenol red, was measured using an absorption spectrometer (SmartSpec Plus; Bio-Rad). The concentration of phenol red was calculated according to the following formula which is determined by calibration curve: phenol red (μM) = 0.0083 / A479. The phenol red in basal compartment was corrected to apical medium by using the weight of the medium and the concentration of phenol red. Then the corrected phenol red concentration of apical medium was divided by the initial phenol red concentration to calculate the level of phenol red condensation. To analysis the correlation between cell density and water transport per cells, the different numbers of cells (1.0×10^5 or 4.0×10^5, respectively) were seeded into the non-coat transwell with 1.0 μm pore (353104, CORNING). After the cell sheets become confluent, the level of phenol red condensation was determined as described above. After the medium was collected, the cell density was counted as described in section 2-3-6, the cell density assay. Then, the level of phenol red condensation was divided by the total number of cells seeded on the insert.

2-3-6. Analysis of Cell Density

Cells on GP-Matrigel were stained with SYTO 9 green fluorescent nucleic acid stain in culture medium, vital stains of nuclei, for 30 min at 37°C. Cells on non-coat transwells with 1.0 μm pore were fixed with 4% paraformaldehyde in PBS, permeabilized with 0.5% Trion X-100 in PBS, and stained with 2 μg/mL Hoechst 33342 and 1:500 diluted Alexa Fluor 488 phalloidin in PBS for overnight at 4°C. Then the cells were captured by the confocal microscopy and the nuclei were counted by ImageJ or by hand. To track cell density, the result of 3D live imaging was used. An area with strong fluorescence of cell membrane was selected from the variation of fluorescence intensities, and cell number was counted by hand. Cell density was then determined by measuring the area change using ImageJ.

2-3-7. Analysis of Cell Proliferation

MDCK-CAAX cells (1.0×10^5) were seeded onto a non-coat 24 well plate. After 1 day, cells were treated with 10 μM Roscovitine or DMSO (control) for 24 h at 37°C. Cells were trypsinized and suspended in 200 μL. One tenth of the suspension was taken for cell counting. The suspension was mixed with 0.4% Trypan Blue solution at a ratio of 1:1, and the number of live cells was counted with a counting chamber.

Remaining cell suspension was seeded to 24 well with the addition of 10 μM Roscotivine or DMSO, respectively. After cells were incubated for 24 h at 37°C, cells were counted again as described above.

2-3-8. Quantitative Analysis of Cell Height

In chapter 3, cell sheets after gel overlay was stained and observed with C1 confocal microscope. A Z-sectional view of cell sheet was randomly selected from a field of view and cell height was measured with ImageJ. Cells were categorized as ‘‘flat’’ when the width was greater than height in the *Z*-section.

In chapter 4, cells were seeded on non-coat transwell with 1.0 μm pore at the cell density of 1.0 x 10^5 or 4.0 x 10^5 cells/24 well transwell. The cells were stained and observed as described in section 2-2-3. A Z-sectional view was randomly selected from a field of view and Z-sectional area of cell sheet was measured by ImageJ. The area was divided by the length of X-axis to calculate the average height of cells. Cells on GP-Matrigel were stained with F-actin, as described in section 2-2-3. Cell height was measured from a Z-sectional view, which was randomly selected from a field of view. Thet allest point of each cell was measured by ImageJ.

2-3-9. Quantitative Analysis of Cell Distance

The domes on GP-Matrigel with bHS and flat cell sheets on GP-Matrigel with IS were stained with Syto9 for 30 min at 37°C and observed by A1 confocal microscopy. The cell distance was measured by ImageJ as the distance between the centers of the nuclei.

2-3-10. Western Blot

Cell sheets on GP-Matrigel were incubated with 20 μM Y27632 in bHS for overnight. Following incubation, the cells were fixed with ice-cold 10% trichloroacetic acid (T9159, Sigma-Aldrich) in PBS. After rinsed thrice with PBS on ice, The cells were lysed using a sample buffer (0.13 M Tris-HCl pH 6.8, 5% dithiothreitol, 2.3% sodium dodecyl sulfate, 10% glycerol, and 0.01% bromophenol blue). The lysed cells were sonicated and heated at 95°C for 5 min, and stored at -20°C. Cell lysates were separated by SDS page with a 12.5% sodium dodecyl sulfate polyacrylamide gel and the separated protein bands were transferred onto polyvinylidene difluoride membranes

(IPVH304F0, Millipore). The membranes were blocked with Can Get Signal Immunoreaction Enhancer Solution 1 (NKB-101, TOYOBO) or 0.5% skim milk in TBST (20 mM Tris-HCl, 150 mM NaCl, and 0.05% Tween 20, pH 7.5) for P-MRLCs or GAPDH, respectively. The membranes were incubated with the primary antibodies in blocking solution and TBST for P-MRLC and GAPDH, respectively, at 4°C for overnight. After washing with TBST, the membranes were probed with anti-rabbit IgG HRP-linked antibody in Can Get Signal Immunoreaction Enhancer Solution 2 or anti-mouse IgG HRP-linked antibody in TBST solution for P-MRLCs and GAPDH at room temperature for 1 h. The dilution rate was described in Table 2.1. The blots were detected using ChemiDoc Touch Imaging System (Bio-Rad). Quantification of signal intensity was performed using Image Lab software (Bio-Rad).

2-3-11. Nuclear Volume Analysis

To stretch cells, a handmade silicone rubber chamber was used as previously described in (Takemoto et al., 2015). The chamber was made of a transparent silicone rubber (SH9555, Toray Dow Corning Silicone) and coated with 50 μg/mL fibronectin for overnight at 4°C. 4.0×10^5 cells were seeded onto the chamber with 30 mm diameter and incubated for 2 days. After staining with 1 μM calcein-AM and 10 μg/mL Hoechst for 1 h at 37°C, the cells were stretched by inserting a steel ring into the ditch of the silicone chamber. Before and after stretching, cells in the same area were observed using A1 confocal microscopy. To observe cells with different densities, hand-made 16 mm radius glass dishes were coated with 1:10 diluted Matrigel for overnight at 4°C. 0.2×10^5, 1.6×10^5, and 2.0×10^5 cells were seeded onto the dishes and incubated for 2 days. After staining with calcein-AM and Hoechst, cells were observed. Cell area and nuclear volume were measured using ImageJ. Cell area was determined from the variation in fluorescence intensity of calcein-AM.

2-4. Quantification and Statistical Analysis

In chapter 3, each experimental condition is described in figure legends. The error bars represent the mean±S.D. The statistical significance was determined as follows. The variance of the two data sets verified whether significantly different or not by using F-test, in which $p<0.05$ indicates the variance was significantly different. For data sets without statistically different variances, two-sided Student's *t*-test was used to analyze the significance. For data sets with statistically different variances, two-sided Welch's *t*-test was used to determine the statistical significance. In Student's *t*-test and Welch's *t*-test, $p<0.05$ indicates statistical significance.

In chapter 4, each experimental condition is described in figure legends. The error bars represent the mean±S.D. The statistical significance was determined as follows. For comparison between the two values both with variance, the data sets were checked to meet the normal distribution by Kolmogorov-Smirnov test, in which $p>0.05$ indicates the normal distribution. Then the variance of the two data sets was verified whether significantly different or not by using F-test, in which $p<0.05$ indicates the variance was significantly different. For data sets without statistically different variances, two-sided Student's *t*-test was used to analyze the significance. For data sets with statistically different variances, two-sided Welch's *t*-test was used to determine the statistical significance. In Student's *t*-test and Welch's *t*-test, $p<0.05$ indicates statistical significance. For comparison between values without variance, the data were tested by 99% confidence interval. The significance estimated by Student's *t*-test, Welch's *t*-test, and confidence interval is indicated with *, §, and †, respectively. For multiple comparisons, Bonferroni correction was used. Cells that were not healthy during data acquisition were excluded from the analysis.

Chapter 3

In vitro Lumen Morphogenesis Induced by Folding Sheet Deformation with Collective Cell Migration

3-1. Introduction

3-1-1. *In vivo* Lumen Morphogenesis

Many organs have tubular networks with continuous lumen to transport fluids or gases. Therefore, lumen morphogenesis is important in development. Common mechanisms include that cells create the new closed space within the cells or between the cells, where there was no outside space previously (Figure 3.1A). This phenomenon is called '*de novo*' lumen formation (Sigurbjörnsdóttir et al., 2014). *De novo* lumen formation *in vivo* is observed in zebrafish vasculature, *C. elegans* excretory cells and the *Drosophila* trachea. In another common mechanism, the lumen is generated by the folding of epithelial sheet (Figure 3.1B). Outside space is enwrapped by a polarized epithelial sheet and becomes the lumen. The *in vivo* folding lumen formation is observed in *Drosophila* gastrulation and *Xenopus* neural tube closure (Martin and Goldstein, 2014). The folding deformation is followed by rearrangement of cells, such as cell shape change or cell positional change (Nikolopoulou et al., 2017). Computer simulation suggests that collective cell migration requires for final closure of neurulation (Inoue et al., 2016). Another report supports this, showing that impairment of migration by integrin-β1 knockdown results in closure defects (Morita et al., 2012). The defect of neural tube closure causes fetal death, stillbirths or neonatal death (Greene and Copp, 2014). Therefore, lumen formation is fundamental process in morphogenesis.

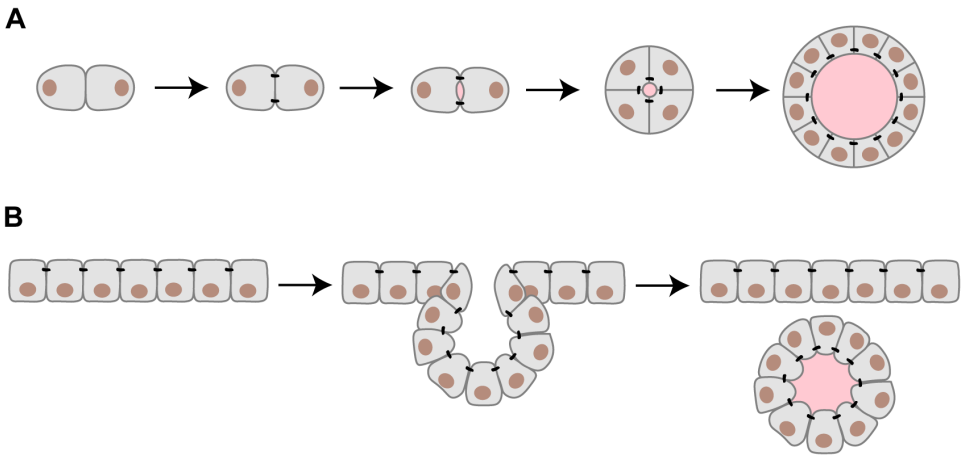

Figure 3.1 Patterns of Lumen formation

(**A**) *De novo* lumen formation. (**B**) Folding lumen formation. Pink area indicate lumen. Black dots indicate tight junctions.

3-1-2. *In vitro* Lumen Morphogenesis

In *in vitro* experiments, MDCK cells cultured in 3D substrate are known to the excellent model to study lumen formation. When single MDCK cells is embedded into collagen gel or Matrigel, the cell proliferates with determining the apicobasal polarity, generates a *de novo* lumen and becomes a spherical monolayer, which is called as “a cyst” (O'Brien et al., 2002). At the initiation of *de novo* lumen formation, cells are not polarized, in which apical proteins distribute on the whole surface of cells. When integrin-β1 receives the signals from ECM, the apical compartment is loaded to endosomes and transported to the center of the cell clusters, opening the luminal cavity. The inhibition of integrin-β1 activity or the downstream factor Rac1 activation inverts the apicobasal polarity and disrupts the lumen formation. Under these conditions, the inhibition of RhoA expression rescues normal polarity and luminal morphogenesis (Yu et al., 2005; Yu et al., 2008).

Lumen formation is also induced by overlaying an polarized MDCK monolayer with a collagen gel (Figure 3.2A)(Hall et al., 1982), a technique that facilitates the reorganization of apical-basolateral polarity (Schwimmer and Ojakian, 1995; Yu et al., 2005; Zuk and Matlin, 1996). After the application of collagen layer to apical surface of MDCK sheets, the sheet becomes multilayered and the polarity dynamically changes to reorganize the apical surface away from the collagen layers, resulting in new lumen structures (Figure 3.2B). This lumen formation is prevented by the inhibitory antibody of integrin-β1, dominant negative of Rac1 or RhoA (Eisen et al., 2006; Yu et al., 2005; Zuk and Matlin, 1996). Taken together, these previous studies indicate that integrins and small G proteins play essential roles in determining polarity and *in vitro* lumen formation.

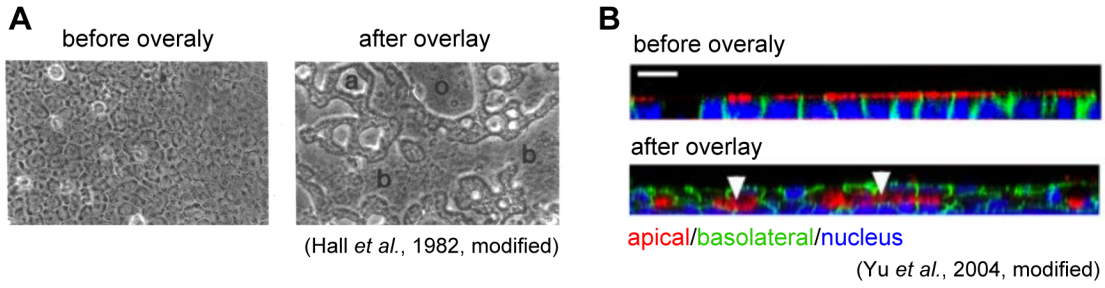

Figure 3.2 Lumen formation in previous studies

(**A**) Phase contrast images of MDCK lumens observed after gel overlay. a and b indicate lumens. o indicates open space. (**B**) Fluorescent images of epithelial remodeling after gel overlay. Arrowheads indicate newly formed lumens. Cells are seeded onto collagen gel (A) or glass (B).

3-1-3. *In vitro* Collective Cell Migration

The collective migration of epithelial cells is a key factor in morphogenesis (see section 1-1-3-1), it is also well observed *in vitro*. In *de novo* lumen formation, MDCK colonies show rotational migration during lumen formation (Hirata et al., 2018). When MDCK colonies are cultured on Matrigel, cells generate tulip-hat like 3D structures on Matrigel (Imai et al., 2015). In the process of the formation of tulip-hat, a cell exhibits mesenchymal phenotype with larger lamellipodium appears at the periphery of the colonies and digs into the substrate with rotational migration. However, it is unknown whether collective cell migration is involved in lumen formation after gel overlay.

The present study showed that a collagen gel overlay induced lumen formation via epithelial sheet folding. The sheet folding was caused by the folding collective cell migration from the periphery of cell sheets. The migration required integrin-β1, Rac1, and the maintenance of cell polarity.

3-2. Results

3-2-1. Lumen Formation by the Folding Collective Cell Migration

To investigate whether the collective cell migration involves to lumen formation after collagen gel overlay, a MDCK epithelial sheet on collagen gel was overlaid with another collagen gel and observed with time-lapse imaging. Immediately after the overlay, periphery of the MDCK sheet moved toward the center of the sheet at a constant velocity, and met at the center (Figure 3.3A,B; Movie 3.1). The morphology of the sheet changed from a flat sheet to a cyst with a lumen (Figure 3.3C). To observe the morphological change in detail, we performed the 3D live cell imaging with MDCK-CAAX cells. After the gel overlay, the periphery of the sheet folded up and migrated to the center of the sheet with keeping the sheet structure, which finally formed the luminal structure (Figure 3.3D; Movie 3.2). To determine whether all of the cells within the colony migrated during the folding of MDCK cell sheets, mosaic colonies, composed of the mixture of fluorescent and nonfluorescent cells, was overlaid with collagen gel and monitored simultaneously using phase contrast and fluorescence microscopy (Figure 3.3E). The cells near the leading edge migrated at the same rate as the leading edge moved ahead. In contrast, the cells distant from the leading edge rarely migrated. These data indicate that MDCK epithelial sheets formed a lumen with folding cell migration after collagen gel overlay.

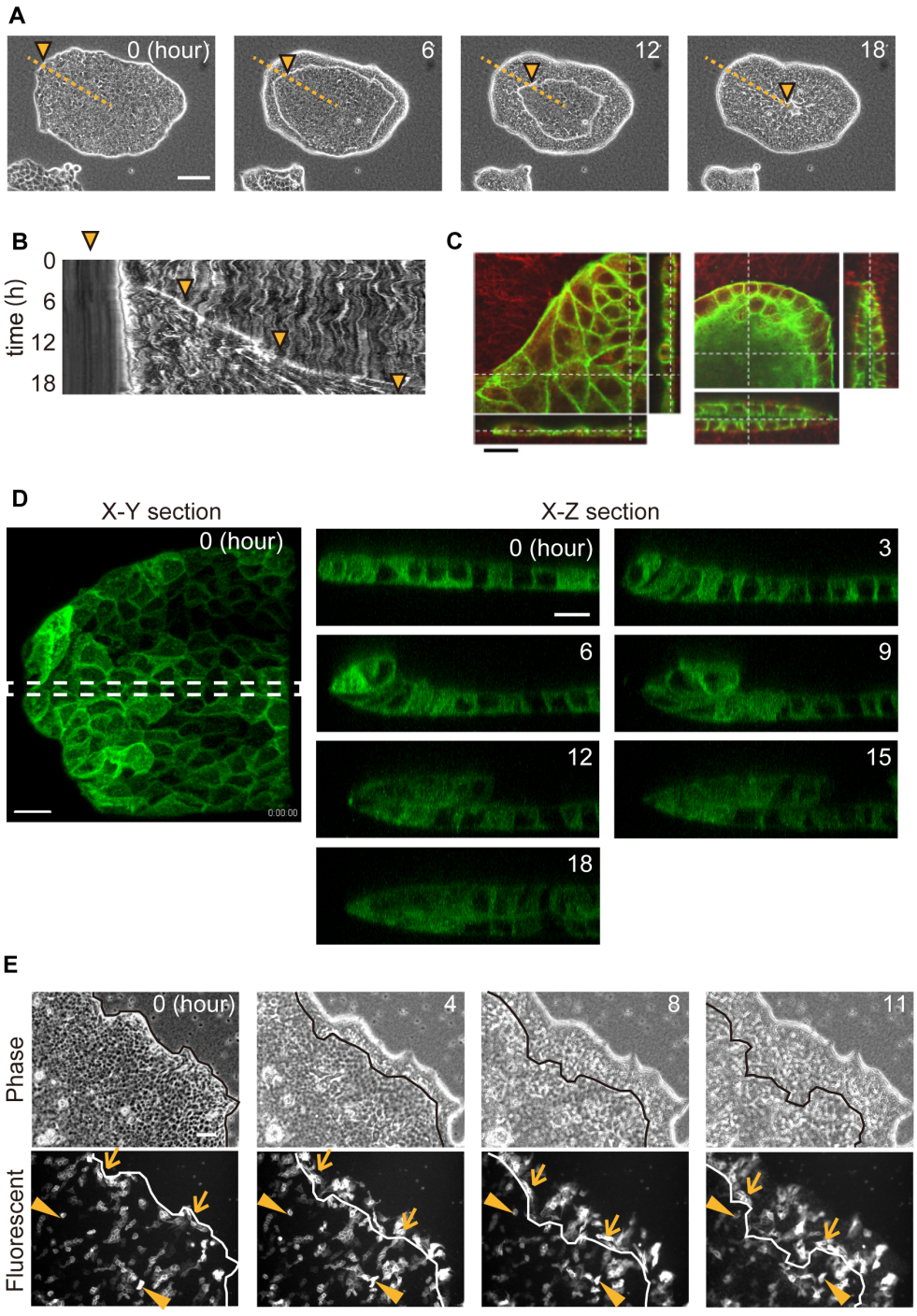

Figure 3.3 Epithelial sheets formed luminal structures by folding migration after the collagen gel overlay.

(**A**) Time development of an epithelial sheet after the collagen gel overlay. Images were taken by a phase contrast microscopy. The orange dotted line corresponds to the horizontal axis of the kymograph in Figure 3-1B. The arrowheads indicate the position of the migrating edge of the

MDCK sheets, and they correspond with the kymograph. Scale bar, 100 μm. (**B**) Kymograph of folding migration of an epithelial sheet. (**C**) Fluorescent images of MDCK sheet immediately after (left) and 24 h after (right) gel overlay. Green, F-actin. Red, collagen. Scale bar, 20 μm. (**D**) 3D live cell imaging of the lumen formation after gel overlay. Green, the fluorescent labeled-cell membrane of MDCK-CAAX cells. *X-Z* sectional views were projection images from the area indicated by the dotted line in an *X-Y* sectional view. Scale bar, 20 μm. (**E**) Simultaneous phase contrast and fluorescence images of the migration. The sheet is composed of fluorescent (MDCK-CAAX cells) and nonfluorescent cells. The lines represent the migrating edge of the folding. The arrows and arrowheads chase the cells at the migrating edge or within the colony, respectively. White, MDCK-CAAX. Scale bar, 100 μm.

The elasticity of scaffolds influence the cell behaviors, including cell migration and morphogenesis (Chen et al., 2019; Haga et al., 2005; Paszek et al., 2005; Rozario and DeSimone, 2010). Therefore, we examined the contribution of the ECM elasticity to lumen formation with the folding migration. When either the upper or lower substrate was a collagen-coated glass coverslip (2-3 GPa) (Barnes et al., 2017) instead of collagen gel (around 600 Pa) (Mizutani et al., 2006a), folding migration did not occur (Figure 3.4A,B). Matrigel (443 Pa) (Soofi et al., 2009) has similar elasticity with collagen gel. When the Matrigel is overlaid to MDCK sheet, cells showed collective folding migration (Figure 3.4C). Agarose gel is not ECM, thus, cells are not able to adhere to agarose gel. The overlaying 0.8% agarose gel (about 3 kPa) (Markert et al., 2013) did not induce the folding migration (Figure 3.4D). Agarose gel is softer than glass but not as soft as collagen gel, therefore, we cannot rule out the possibility of the effect of elasticity. Yet, these data indicate that cell-adherable soft substrate may be important for folding migration. Computer simulation supported the elastic contribution of substrates, showing that extensively high elasticity prevent sheet folding (Appendix 2; performed by Mr. Ryosuke Tanaka).

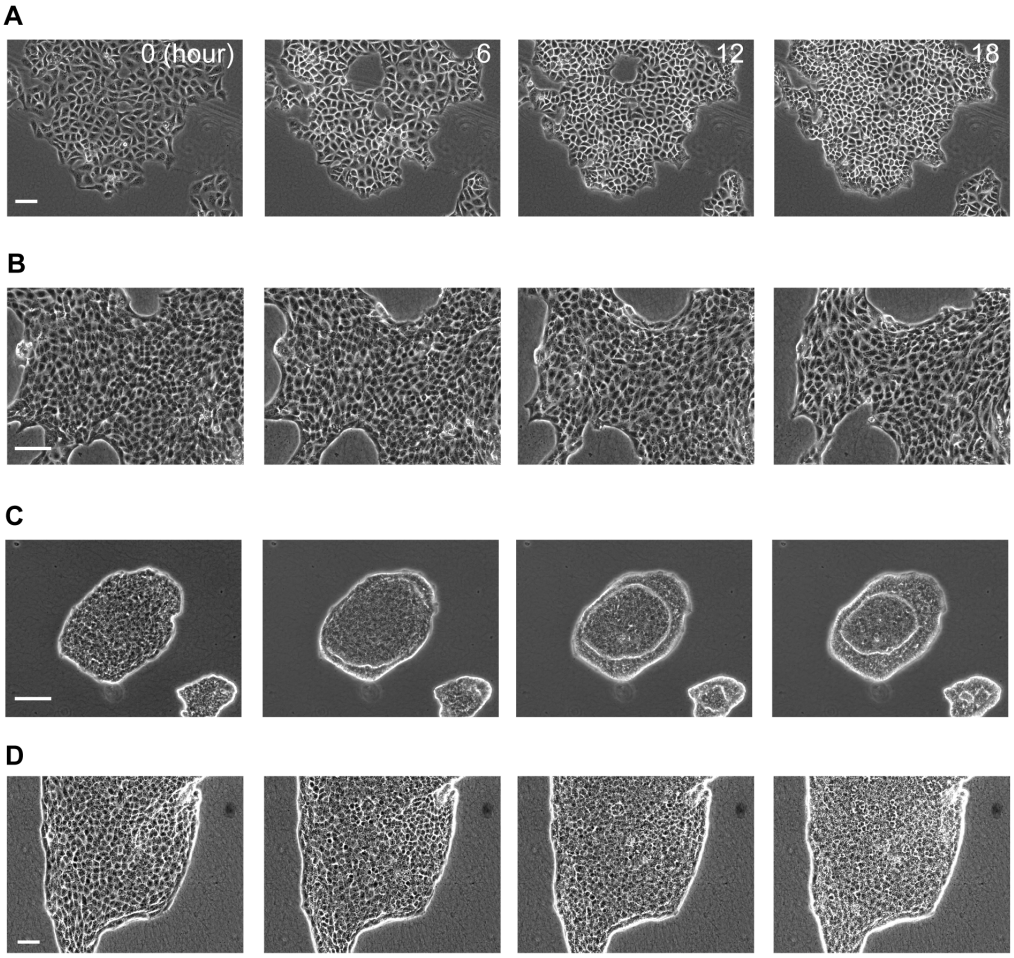

Figure 3.4 The folding migration occurred when surrounded by cell-adherable soft substrates.

(**A**) Time-lapse images of MDCK colonies cultured on a collagen-coated glass and overlaid with collagen gel. (**B**) Time-lapse images of MDCK colonies cultured on collagen gel and overlaid with a collagen-coated glass cover slip. (**C**-**D**) Time-lapse images of MDCK colonies cultures on collagen gel and overlaid with Matrigel (*C*) or agarose gel (*D*). Scale bars, 100 μm.

After gel overlay, cells formed a lumen with keeping the initial round shape of MDCK sheets (Figure 3.3A). This was not limited to round shape. For example, the epithelial sheets were cut in an arbitrary shape using a micromanipulator (Figure 3.5; Movie 3.3; Appendix 3-1; Appendix 3 was performed by Mr. Genki Ogata). When the epithelial sheet was shaped into letters such as "L," "O," "V," or "E," the peripheries of the sheets folded up in response to gel overlay. After the folding migration was completed, lumens retaining its initial shape were generated.

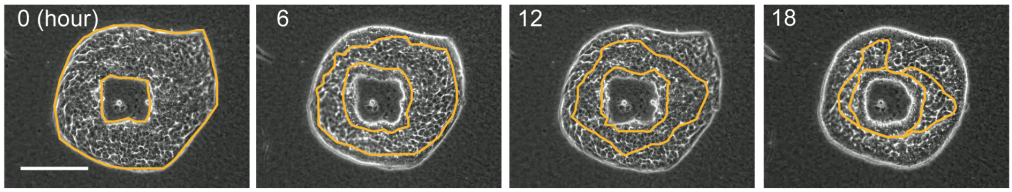

Figure 3.5 The lumen induced by the folding maintained the initial shape of the sheets.

(**A**) Temporal sequence of epithelial sheets cut in "O" shape. Orange lines represent the migrating edge of the folding. Scale bar, 200 μm.

3-2-2. The Contribution of Integrin-β1, Rac1 and Myosin to the Folding Migration

We examined the contribution of cell migration to lumen formation with the inhibitor of integrin-β1 (AIIB2), Rac1 (Z62954982), or ROCK (Y27632). To minimize experimental error, large epithelial sheets were prepared so that folding initiated from relatively straight periphery (Figure 3.6A). Compared with the control, lumen formation became slower with the treatment of AIIB2 or Z62954982. In contrast, lumen formation proceeded faster compared with control with the treatment of Y27632. For statistical analysis, cell migration was observed for 8 h before and after inhibitor treatment. The distance of cell migration was plotted against observation time, and the migration velocity was calculated from the slope of the linear approximation of the curve. The ratio of change in migration velocity was estimated (Figure 3.6B). The results showed that the velocity of folding migration significantly decreased with the treatment of AIIB2 and Z62954982, but significantly increased with the treatment of Y27632 (Figure 3.6C).

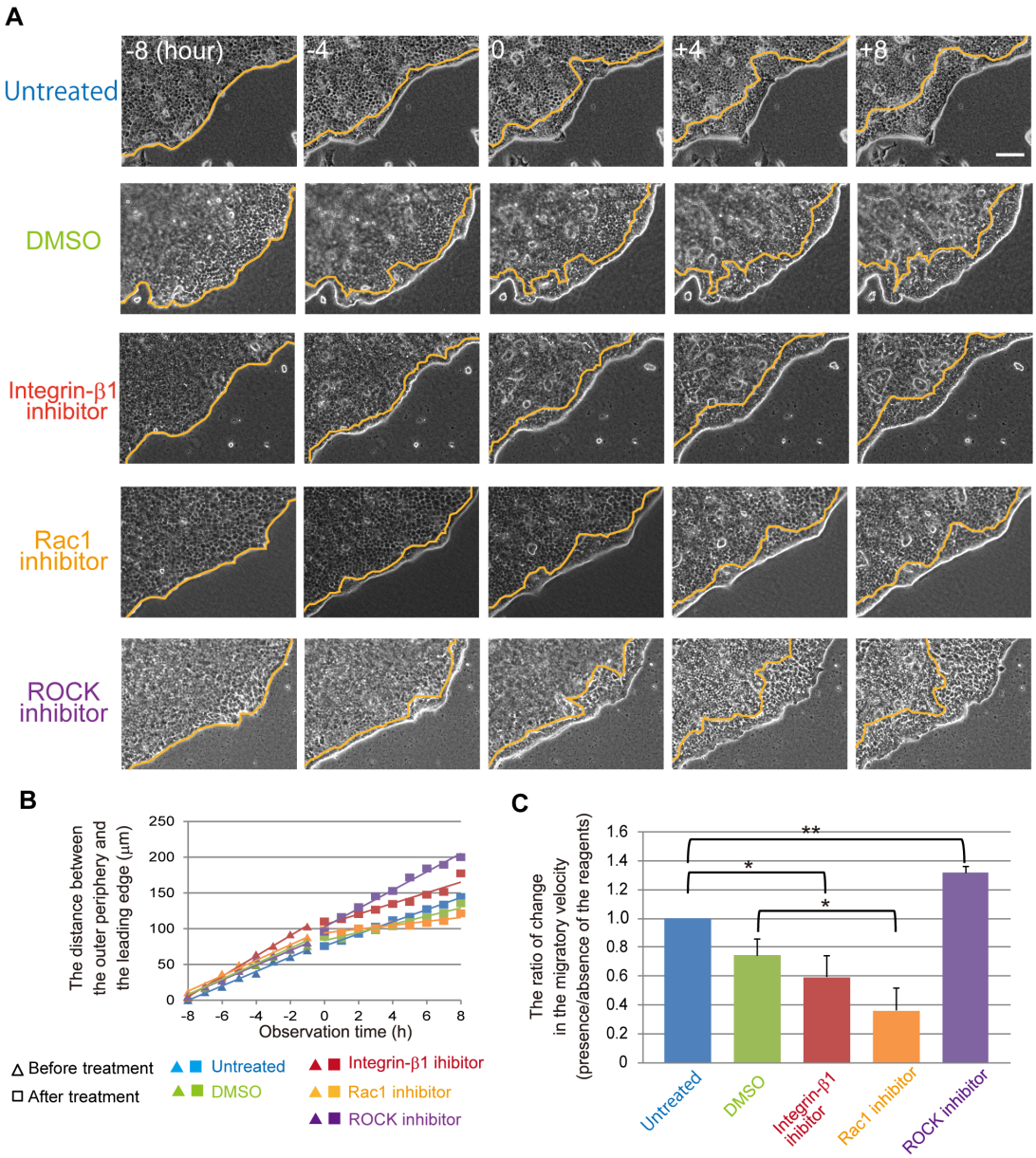

Figure 3.6 Inhibition of either integrin-β1 or Rac1, but not ROCK, delayed folding.

(**A**) Time development of folding in the presence of integrin-β1 inhibitor (AIIB2), Rac1 inhibitor (Z62954982), ROCK inhibitor (Y27632). DMSO was used as a control for the Rac1 inhibitor. Each reagent was added at time zero. Orange lines represent the leading edges of the folding sheet. Scale bar, 100 μm. (**B**) The scatter plot shows the migration distance from the outer periphery to the migrating edge for each treatment. (**C**) Bar graph indicating the mean ratio of the migration velocity in the presence of inhibitors. n = 3 independent experiments. Mean±S.D. *, p<0.05. **, p<0.01.

To determine whether integrin-β1, Rac1, and ROCK activities contribute to the initiation of folding, inhibitors were added for at least 30 min before the gel overlay. The ratio of the velocities of folding migration was estimated using the same methods described above (Figure 3.7). Consistent with the data shown in Figure 3.6, AIIB2 and Z62954982 decreased the velocity of migration, and Y27632 had no significant effect.

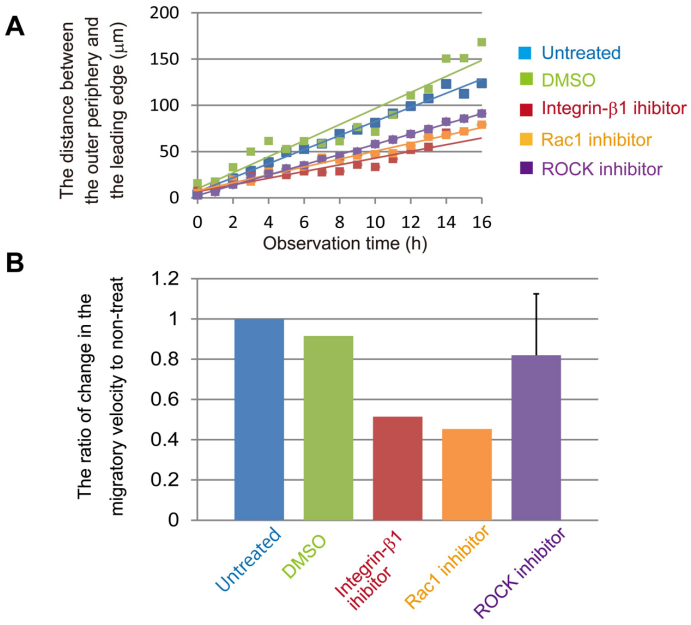

Figure 3.7 Inhibition of either integrin-β1 or Rac1, but not ROCK, delayed early folding.

(**A**) The scatter plot of the migration distance from the outer periphery to the leading edge for each treatment against observation time. Inhibitors were added at least 30 min before gel the overlay. The mean values of at least three independent experiments are shown for untreated or Y27632 treated cells. The data of the other reagents represent one experiment. (**B**) Bar graph of the mean ratio of the migration velocity with or without inhibitors. *n* = at least three independent experiments. Mean±S.D.

To confirm whether Y27632 inhibited ROCK activity, we detected the 2P-MRLC in MDCK cells on collagen gel with immunofluorescent staining. In untreated cells, 2P-MRLC was localized to the smooth periphery of the MDCK sheets but was not detected when the cells were treated with Y27632 (Figure 3.8A). In the cells leading collective migration (leader cells), 2P-MRLC was also detected at the periphery of leader cells. In contrast to the smooth edge, 2P-MRLC was detected in leader cells in presence of Y27632 (Figure 3.8B). Further, migration of leader cells was

not prevented with Y27632 treatment (Figure 3.8C). These results suggest that integrin-β1 and Rac plays important roles in the collective migration during lumen formation. In contrast, ROCK activity may not have significant effects for lumen formation by the folding.

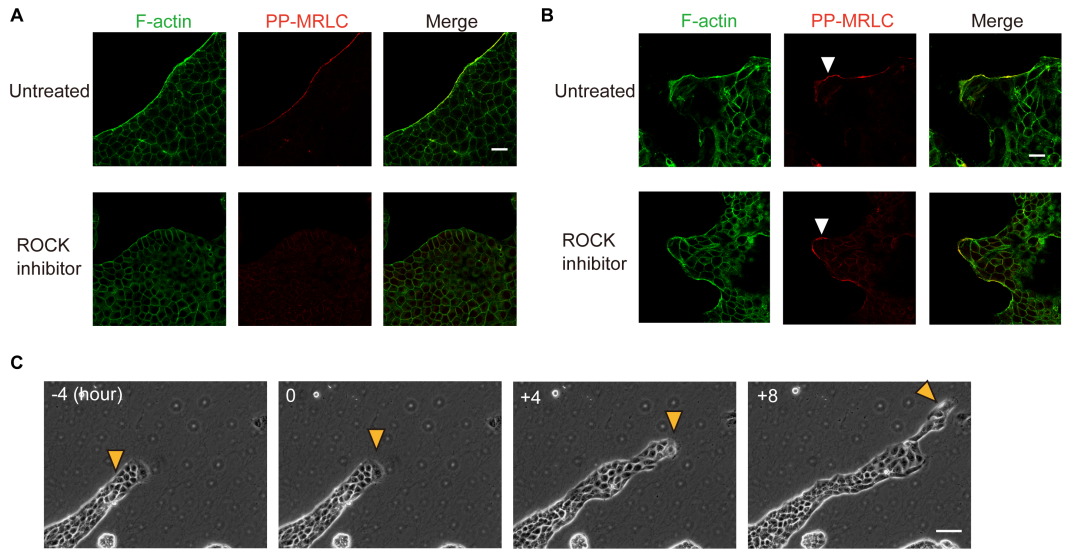

Figure 3.8 Treatment with a ROCK inhibitor induced dephosphorylation of MRLC at the edge of colonies, but in the leader cells.

(**A**-**B**) Fluorescent images of smooth edge (*A*) and leader cells (*B*) of MDCK sheets cultured on collagen gel. Y-27632 was treated for 30 min or overnight before fixation in smooth edge or leader cells, respectively. Green, F-actin. Red, 2P-MRLC. Scale bars, 25 μm. (**C**) Time-lapse images of a leader cell migrating on collagen gel. Y27632 was added at time zero. Scale bar, 100 μm. The arrowheads point to the leader cells.

3-2-3. The Contribution of Epithelial Cell Polarity to the Folding Migration

We next investigated the contribution of cell polarity to MDCK sheet folding. The apical marker gp135 kept localizing on the inner surface of a future lumen (Figure 3.9A). In addition, and lateral marker E-cadherin and basolateral marker integrin-β1 also continued to localize on cell-cell and cell-substrate interface. From these results, apical-basolateral polarity was maintained during epithelial sheet folding. When MDCK sheet were treated with TGF-β1, which disrupts cell polarity (Figure 3.9B)(Xu et al., 2009), the sheet did not fold after gel overlay, but instead, cells moved randomly and

did not form a lumen (Figure 3.9C-E; Movie 3.4). These suggest that maintaining apical-basal polarity is crucial for lumen formation by folding migration.

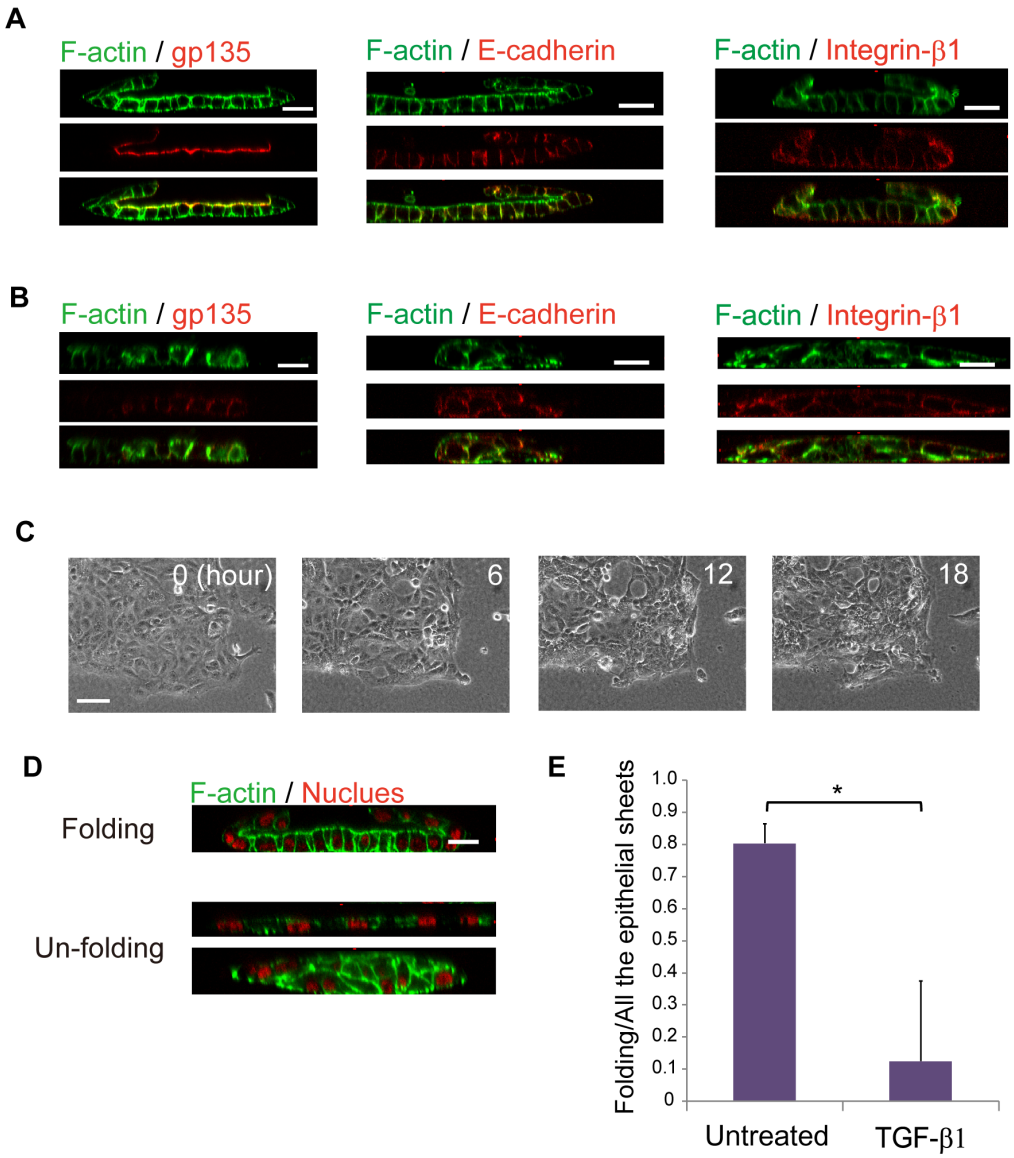

Figure 3.9 Disruption of cell polarity by TGF-β1 treatment prevented folding.

(**A**) Fluorescent images of epithelial sheet during lumen formation by the folding. (**B**) Fluorescent images of cells treated with TGF-β1 after gel overlay. TFG-β1 was pretreated for 2 days before gel overlay. Green, F-actin. Red, gp135, E-cadherin, or integrin-β1. (**C**) Time-lapse images of polarity-disrupted MDCK colonies after the gel overlay. Scale bar, 100 μm. (**D**) Categorization of folding and unfolding MDCK sheets. Green, F-actin. Red, nucleus. Cells were categorized as "folding sheet" when a space was detected between the upper and the lower cell layers in the

Z-sectional view. (**E**) The ratio of folding to non-folding cells in the presence or absence of TGF-β1. $n = 4$ independent experiments. Mean±S.D. *, $p<0.05$. (A, B, D) Scale bars, 25 μm.

To observe how cells at the periphery of the colony initiate folding, we focused on integrin-β1, because cells pretreated with AIIB2 delayed lumen formation (Figure 3.6 and Figure 3.7). In addition, we found that disrupting the localization of integrin-β1 prevented folding (Figure 3.9). Therefore, we reasoned that the polarized localization of integrin-β1 before the gel overlay played a key role to initiate folding. We found that integrin-β1 localized to the whole cell surface only at the periphery of the colony before the gel overlay (Figure 3.10). Integrins is activated by adhesion to the ECM and its outside-in signaling promotes to cell migration (Hynes, 2002), suggesting apical integrin-β1 on cell periphery may have a key role to initiate and lead folding migration in response to gel overlay.

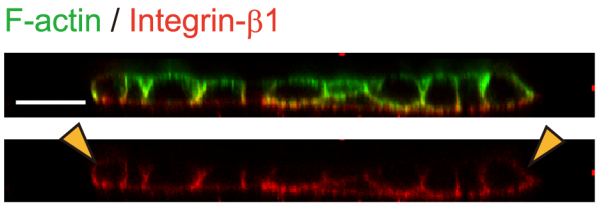

Figure 3.10 Integrin-β1 localized to the entire surface at the periphery of the MDCK sheet.
Fluorescent image of MDCK cells on collagen gel. Green, F-actin. Red, Integrin-β1. The arrowheads point to the integrin-β1 at apical side. Scale bar, 25 μm.

3-2-4. The Contribution of Cell Flattening to the Folding Migration

The epithelial colonies maintained the initial area of the sheet during folding (Figure 3.3A and Figure 3.5A), causing the surface area of the epithelial monolayer to double in size after lumen formation. To determine how the cells increased the surface area, we first observed the contribution of cell proliferation. Histone-H3 Ser10 is phosphorylated during mitosis (Hendzel et al., 1997). Few fluorescent cells were detected with the anti-p-histone antibody in midway of the lumen formation, suggesting the cell proliferated during the folding (Figure 3.11A). However, the inhibitor of cell division Roscovitine did not prevent folding (Appendix 3-2). Instead, a *Z*-sectional view

of the folding epithelial colony revealed that the cells in the top layer became flatter compared with those in the bottom layer (Figure 3.11B,C). These data indicate that the surface area of epithelial colonies was increased by the flattening of cells in the top layer during folding lumen formation.

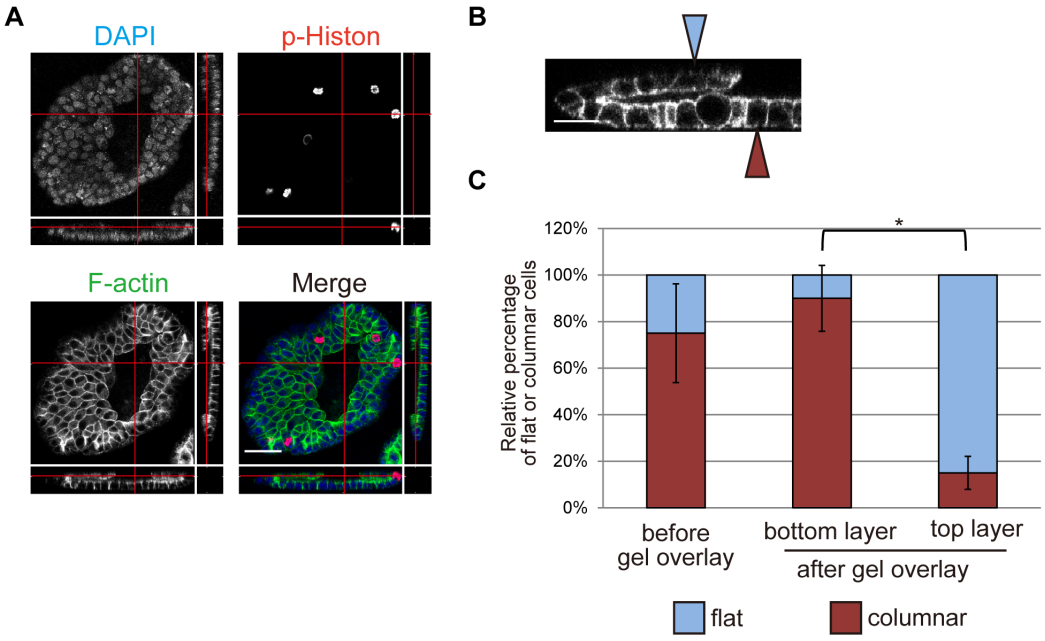

Figure 3.11 The surface area of epithelial colonies increased by cell flattening.

(**A**) Fluorescent images of MDCK sheets stained with DAPI (blue), and antibodies against p-histone (red) and F-actin (green) during folding. Red lines represent the planes from which the sectional views were generated. Scale bar, 50 μm. (**B**) The *Z*-sectional view of folding with F-actin fluorescent staining. The blue and red arrowheads indicate flattened and columnar cells, respectively. Scale bar, 25 μm. (**C**) The ratio of flat to columnar cells in the colony before and after the gel overlay. $n = 20$ cells from two independent experiments. Mean±S.D. *, $p<0.05$.

3-2-5. The Contribution of Cellular Traction Force to the Folding Migration

Cellular contractile force plays important roles in morphogenesis (Diaz-de-la-Loza et al., 2018; Eiraku et al., 2011; Heisenberg and Bellaïche, 2013; Kasza and Zallen, 2011; Martin, 2010; Young et al., 1993); therefore, we examined whether MDCK cells generate a mechanical force during folding. First, we observed lumen formation with collagen gel containing latex beads. With 12 h-observation of the

folding, the beads moved by approximately 10.5 μm along the direction of cell migration on the *X*-*Y* plane, but rarely along the *Z*-axis (Figure 3.12A). Actomyosin generates a contractile force through the phosphorylation of MRLC (Mizutani et al., 2006b). Immunofluorescent staining was performed on the folding MDCK sheets. The images of F-actin and 2P-MRLC showed that cells exert the contractile force at the leading edges of the folding sheet (Figure 3.12B). Leader cells, which are reported to have a traction force on substrates through MRLC phosphorylation (Reffay et al., 2014), were present in some regions of the leading periphery during folding. In addition, the myosin inhibitor blebbistatin completely prevented the lumen formation (Figure 3.12C). These results suggest that MDCK cells generated a traction force at the leading edge of cell migration during lumen formation.

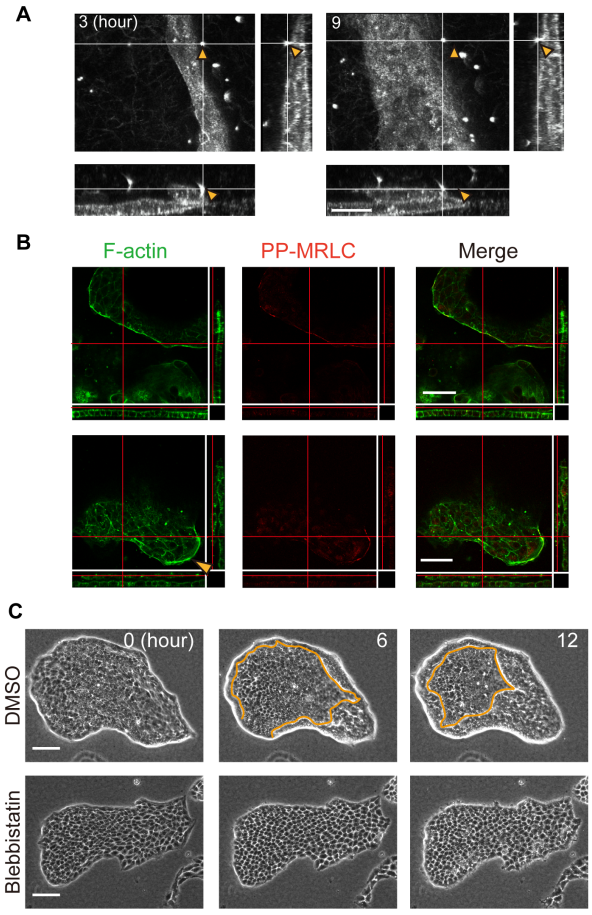

Figure 3.12 MDCK cells deformed the collagen gel during lumen formation.

(**A**) 3D live cell imaging of MDCK cells within a latex bead-containing collagen gel. Images were

acquired using the reflection interference mode of a confocal fluorescence microscope. The arrowheads point to the position of the beads at 0 h. Scale bar, 25 μm. (**B**) Immunofluorescent images of folding MDCK sheet. Green, F-actin. Red, 2P-MRLC. Sectional views along the red lines are shown. The arrowhead points to a leader cell. Scale bars, 50 μm. (**C**) Time development of MDCK sheet with the treatment of myosin inhibitor blebbistatin or DMSO (control). Orange lines indicate the migrating edge of the cell sheet. Scale bars, 100 μm.

3-2-6. The Contribution of ECM Degradation to the Folding Migration

In addition to traction force, the degradation of the ECM plays an important role in cell migration through a 3D matrix. For example, MDCK cells secrete matrix met alloproteinase (MMP) isoforms that degrade collagen during tubulogenesis (Hellman et al., 2008; Kadono et al., 1998). Therefore, we determined whether degradation of the ECM contributed to folding. Immunofluorescence staining of collagen detected a collagen gel-free region between overlaid collagen layer and the bottom cell layer during folding (Fig. 2-13A). To examine whether the degradation of the ECM contributed to folding, the MMP inhibitor GM6001 was treated to the cells with gel overlay. GM6001 treatment reduced the size of the collagen gel-free space and delayed the lumen formation (Fig. 2-13A,B). Collagen zymography was performed to determine whether MDCK cells degraded collagen. Considering the molecular masses of MMPs (Kivelä-Rajamäki et al., 2003), the result reveals that MDCK cells likely secreted MMP-8 during the folding phenomena (Appendix 3-3). These results suggest that the degradation of the ECM may help cells migrate smoothly through the collagen matrix in gel overlay-induced lumen formation.

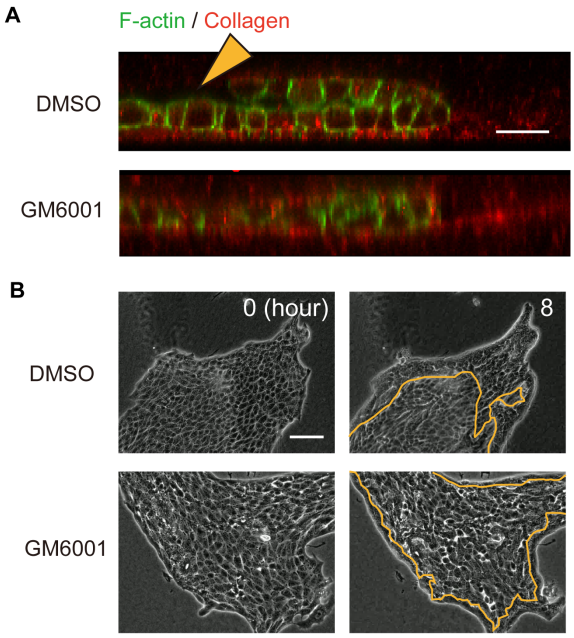

Figure 3-13 MDCK cells degraded the collagen gel.

(**A**) Z-sectional fluorescent image of the folding lumen formation with the treatment of MMP inhibitor GM6001 or DMSO (control). Green, F-actin. Red, collagen. Red lines indicate the plane from which the Z-sectional view was generated. Arrowheads point to the space between the upper collagen layer and the lower cell sheet. Scale bar, 20 μm. (**B**) Time-lapse observation of MDCK cells in the presence or absence of GM6001, which was added immediately after the collagen gel overlay. The orange line represents the migrating edge of the MDCK sheet. Scale bar, 100 μm.

The inhibition of MMP activity by GM6001 reduced the size of the gel-free space, although the lumen still formed. This indicates that folding was not a simple cell migration on a planar surface of collagen gel. To determine whether folding was induced by the migration to the collagen gel-free space, we observed MDCK cells by using a collagen gel sandwich assay (Appendix 3-4). In the collagen gel sandwich assay, gelled collagen is layered on the colonies, instead of the collagen gel overlay in which the collagen solution gels after it is poured over the cells. By changing the order of gelation, the sandwich method provides the cells with a gel-free region between the upper and lower gels. Despite the presence of a gel-free space surrounding the colony, the MDCK cells did not spread out to the free space but migrated inwardly to the center of the colony. Therefore, the collagen gel sandwich assay indicates that folding was not the simple migration on gel surface.

3-3 Discussion

Here we demonstrated that a collagen gel overlay induced the folding of an epithelial sheet from its periphery to form a luminal structure. The folding did not occur when either upper or lower substrates were glass coverslips. The elasticity of a substrate changes various cellular behaviors (Butcher et al., 2009; Engler et al., 2006; Haga et al., 2005; Ishihara et al., 2013). Example includes the migration of MDCK cells; directional collective migration is induced when the cells are cultured on a soft collagen gel, but not on a glass coverslip (Haga et al., 2005). We show here that collective migration occurs during lumen formation after the collagen gel overlay. Peripheral cells of the epithelial sheet migrated collectively toward the center of the colony in response to gel overlay. Although these results indicate that a collagen gel provides a soft substrate for the collective migration of cells to form a luminal structure, the molecular mechanism is yet to be investigated.

Inhibitor of integrin-β1 or Rac1 delayed the lumen formation by folding collective migration, on the other hand, inhibitor of ROCK increased the migration. The results of ROCK inhibition are consistent with the previous report showing that ROCK inhibition enhances the migration of epithelial cells and fibroblast (Nakayama et al., 2005). In addition, ROCK also contributes to the directional persistence of migration (Totsukawa et al., 2004). Because integrin-β1 and Rac1 are crucial factors for cell migration, cell migration is essential for epithelial sheet folding and subsequent lumen formation.

Cell polarity has important roles for epithelial sheet folding that forms a lumen. The results of immunofluorescent staining showed that apical-basolateral polarity was maintained during lumen formation after gel overlay. In a previous report, MDCK cells cultured on a glass substrate formed small lumens after gel overlay, in which a reorganization of cell polarity, but not cell migration, was observed (Schwimmer and Ojakian, 1995). These suggest that the maintenance of cell polarity may be indispensable for lumen formation induced by folding migration of an epithelial sheet.

The observation of the velocity field during folding revealed that the cells around the migrating edge moved faster than those located near the center of bottom cell layer. A similar velocity field is observed in cell migration of wound healing (Zahm

et al., 1997), where the cells around the wound edge migrate faster than those far from the edge. The structure of the migrating edge is also similar. Actomyosin fibers and leader cells localized at the leading edge (Jacinto et al., 2001). In contrast, apical-basolateral cell polarity has different phenotype, which is lost in wound healing (Aukhil, 2000) but maintained during folding. These suggest that maintenance of cell polarity is a specific character of folding and its further study may provide insights into the molecular mechanisms of lumen formation after gel overlay. Our present study showed that the disruption of cell polarity by TGF-β1 prevented lumen formation, but how cells maintain polarity is unknown. Par3/Par6/aPKC complex is the regulator of apical-basal polarity in epithelial cells (Chen and Zhang, 2013), which suggests an avenue of investigation for future studies.

Integrin-β1 plays an essential role in the initiation of collective migration *in vivo* (Marsden and DeSimone, 2001; Solnica-Krezel, 2005). For example, cell migration during gastrulation in frogs has similar migration to the folding studied here. The sheets of mesodermal and endodermal precursors roll into the blastopore, reverse the direction of migration from veget al pole to the animal pole, and proceed on the back surface of the prefolded cell layer via radial intercalation (Chen and Zhang, 2013). In the early stage of gastrulation, the adherence of integrin-β1 to the ECM is required (Marsden and DeSimone, 2001). Future studies on the downstream effectors of integrin-β1, such as paxillin or FAK (Hynes, 2002), may provide further insights into the role of integrin-β1 in the initiation of folding.

Although the folding of an epithelial sheet is not reported *in vivo*, the manipulation of lumen formation *in vitro* becomes a promising application for tissue engineering. Here we succeeded to generate arbitrarily shaped tubes in a collagen gel. Especially, tubes by the folding are able to contain branching structures, which has been difficult to produce by tissue engineering. If this method can be applied to vascular endothelial cells, then any branched blood vessel structure with an arbitrary shape can be produced and utilized for transplants.

In summary, a collagen gel overlay induced the integrin-β1 and Rac1-mediated folding migration of MDCK cells cultured on a collagen gel to form a luminal structure. Apical-basolateral polarity was maintained during the entire process. With a computational approach, elasticity of the surrounding substrate is proposed to be important for the folding of an epithelial sheet although the molecular mechanism of

folding is yet to be unknown, the collagen gel overlay method has great potential for tissue engineering.

3-4 Legends for Movies

Movie 3.1 Folding lumen formation by MDCK sheets after collagen gel overlay.

Phase contrast time-lapse movie of folding lumen formation. 150 min/frame.

Movie 3.2 3D live imaging of viable MDCK sheets after collagen gel overlay.

3D live cell imaging movie of folding lumen formation. 330 min/frame.

Movie 3.3 Lumen formation of an "O"-shaped MDCK sheets.

Phase contrast time-lapse movie of folding lumen formation of "O"-shaped sheets. 30 min/frame

Movie 3.4 The movement of cell sheet after gel overlay in the presence of TGF-β1

Phase contrast time-lapse movie of cells with TGF-β1 treatment in collagen gel. 150 min/frame

Chapter 4

Stable *in vitro* Dome Morphogenesis on ECM Induced by Osmotic Gradients

4-1. Introduction

4-1-1. Dome Formation *in vivo* and *in vitro*

Dome is a hemi-sphere-shaped structure and dome formation is one of the fundamental processes in morphogenesis. Morphogenesis builds 3D shapes via bending, folding, and elongating of flat epithelial sheets (Gilmour et al., 2017). Dome formation is the example of bending deformation (Gilmour et al., 2017), and it is reported in both *in vivo* and *in vitro* morphogenesis.

Dome-like structures *in vivo* were found at the surface of gut and reported in the early twentieth century (Figure 4.1A)(Boyd et al., 1968; Ushiki, 2013). The dome structures are called villi and have a function to absorb nutrition from meals to the body. In the case of villi formation in chicken, smooth surface of epithelium buckles into ridges as the surrounding muscle layers develop (Shyer et al., 2013). The ridges transform into zigzag shape, and then finally become dome-like shape. Meanwhile, villification of mouse proceeds in different process from that of chicken. The villification starts from simultaneous appearance of round domes with a polka dot pattern, not through ridges (Chin et al., 2017; Walton et al., 2016a). At the domes, epithelial cells extend the cell area to grow the dome structures. The dome formation is also observed in follicle formation on chicken skin (Shyer et al., 2017). In common with mouse villification, the follicle formation initiates from round domes with polka dot pattern. However, in contrast to villi formation in mouse, epithelial cells in the follicle become compressed in the process of the dome formation.

Domes *in vitro* were firstly reported in epithelial monolayer in 1969 (Figure 4.1B)(Leighton et al., 1969). On the solid substrate, a part within a monolayer detaches from the substrate and forms domes with expanding cell area (Latorre et al., 2018). The *in vitro* domes hold the fluid in their interior. The domes are observed in many epithelial cell lines, such as Canine kidney epithelial (MDCK) cells, *Xenopus* kidney epithelial cells, pig kidney epithelial cells, Fischer Rat thyroid epithelial cells (Hull et al., 1976; Ichigi and Asashima, 2001; Ikuzawa et al., 2007; Latorre et al., 2018; Leighton et al., 1969; Leighton et al., 1970; Tonoli et al., 2000). Like these, dome formation is often observed in both *in vivo* and *in vitro* morphogenesis.

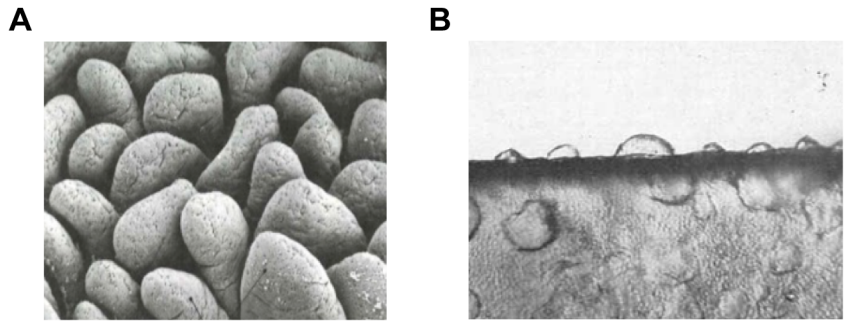

Figure 4.1 Dome structures in vivo and in vitro

(**A**) Image of *in vivo* domes on the intestine. (**B**) The image of *in vitro* domes of epithelial cell lines.

4-1-2. The Driving Factors of the Dome Formation

The driving factors of dome formation are still not fully elucidated. In villifation and follicle of chicken, the compressive stress has been reported as the key factors to initiate the morphogenesis (Shyer et al., 2017; Shyer et al., 2013). In chick villification, muscle layers restrict the expansion of epithelial layer to proceed the epithelial deformations (Shyer et al., 2013). The inhibition of muscle layer development leaves the epithelium smooth, and physical restriction with a silk tube rescues to initiate the villi formation. In the follicle, the mesodermal cells aggregate and contract the epithelial layer, inducing the compression of epithelial cells (Shyer et al., 2017). The compressive stress activates the β-catenin signaling in cells, which initiate the follicle differentiation. The inhibition of the mesodermal traction prevents the epithelial compression and subsequent β-catenin activation. In contrast to these, the compressive stress is not likely to contribute to mouse villification, Dome structures in mouse appear independently from the development of muscle layer (Chin et al., 2017; Walton et al., 2016a; Walton et al., 2016b). Where the domes' shape is determined by the mesenchymal cell cluster beneath the epithelium like the follicles, but epithelial cells in mouse villification become extended rather than compressed, suggesting the different mechanisms from follicle development are required. Thus, the factor that triggers dome formation on mouse gut is not known.

The mechanism of *in vitro* domes is better studied than *in vivo* domes. *In vitro* domes are considered to form through the following steps: 1) Transcellular transport of Na^+ ions, which results in the interstitial increase of the ion concentration on the cell's basal side. 2) The osmotic gradient emerges by the increase of the ions, which leads to

fluid influx to the basal side. 3) Hydrostatic pressure generated by the fluid detaches cells from the substrate and induces dome formation. Previous reports have already demonstrated the contribution of 1) the transcellular transport of ions and 3) hydrostatic pressure. The contribution of the Na^+ ion transport is examined with the inhibitor of the ion transporter, which results in the disappearance of the fluid-filled domes (Ikuzawa et al., 2007; Leighton et al., 1970). Additionally, cells did not form domes on permeable substrate, which let the ions go out from the underneath of cells (Leighton et al., 1970). The hydrostatic pressure of the fluid is observed from the deformation of soft polydimethylsiloxane substrate (Latorre et al., 2018). Other paper shows that the increase of cell-substrate adhesion abolishes the dome formation (Rabito et al., 1980). However, 2) the osmotic gradient has not been fully examined, and it is not enough investigated the reaction of epithelial sheets with the exposure of osmotic gradient.

4-1-3. The Difference in Stability between *in vivo* and *in vitro* Domes.

The dome structures are observed both *in vivo* and *in vitro*, however, there is a notable difference in stability between these two domes. *In vitro* domes repeat collapse and rebirth, on the other hand, *in vivo* domes in mouse villification are stable once their shape are formed (Chin et al., 2017; Latorre et al., 2018; Leighton et al., 1969; Walton et al., 2016a). This difference is likely to result from the substrate of the inside of the domes. Basal side of *in vitro* domes are filled with fluid., Meanwhile, *in vivo* domes has an extracellular matrix (ECM), which provides the structural supports to 3D shape (Bonnans et al., 2014; Rozario and DeSimone, 2010). For example, loss of collagens weaken the integrity of connective tissues and causes the rupture of blood vessels (Liu et al., 1997). However, any previous studies have not observed the contribution of osmotic gradient to the dome formation with ECM. Here, we found that osmotic gradient triggers dome formation of an epithelial sheet on ECM *via* AQP water transport and subsequent ECM swelling *in vitro*.

4-2. Results

4-2-1. Osmotic Tolerance of MDCK Cells

In this study, *in vitro* experiments were performed because it is technically difficult to observe osmotic contribution *in vivo*. We firstly investigated that osmotic tolerance of MDCK cells to perform the experiments in the state that cells alive. To prepare hypotonic stress, normal DMEM was diluted with sterile water. For hypertonic stress, normal DMEM was supplemented with additional mannitol. Cells were incubated in each medium for overnight and the viability was checked. For positive control, cells were exposed to UV in clean bench for 15 min, and the results showed that 90% of the UV irradiated cells were died (Figure 4.2). In response to osmotic stress, the viability declined in 1:6 diluted DMEM (approximately 50 mOsm/kg•H_2O) and in DMEM with additional 400 mM Mannitol (approximately 700 mOsm/kg•H_2O). From these results, cells were treated with osmotic stress from about 100 to 600 mOsm/kg•H_2O.

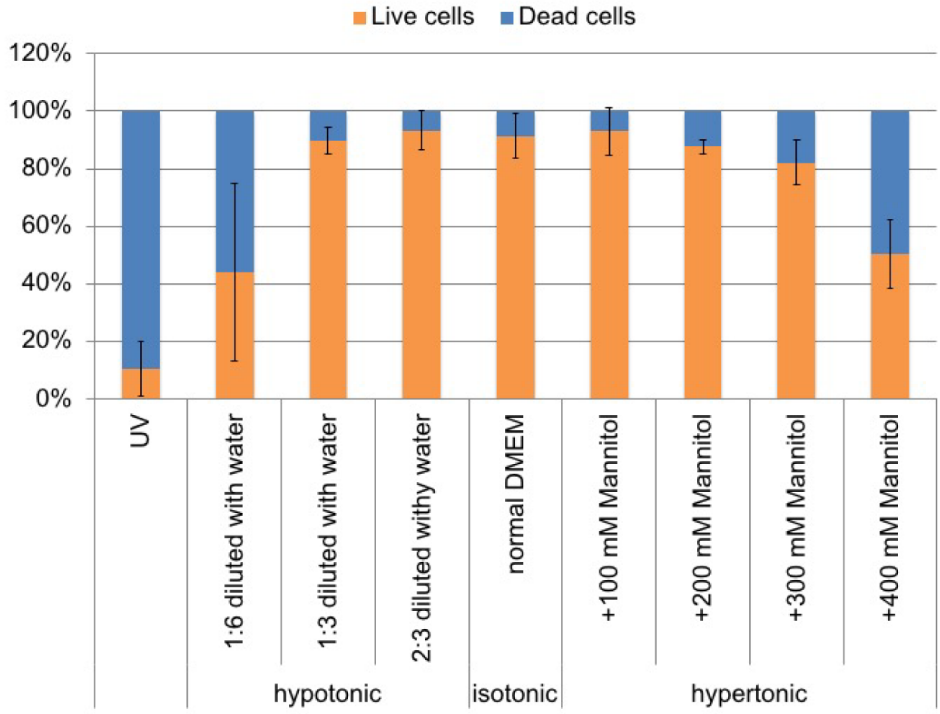

Figure 4.2 Cells withstood a certain range of osmotic stress

The analysis of osmotic tolerance in MDCK-2 cells incubated overnight in indicated culture conditions. *n* = at least 3 independent experiments. Mean±S.D.

4-2-2. Fluid-Filled Dome Formation on Permeable Membrane

In order to confirm the osmotic contribution to dome formation suggested in preceding researchers, we examined whether osmotic gradient induce the domes to epithelial sheet without ECM (Figure 4.3A). Cells were seeded onto permeable membrane without ECM and exposed to basal hypertonic stress (bHS), which the basal compartment was replaced with hypertonic DMEM (H-DMEM). For control, a cell sheet was incubated in isotonic stress (IS) with isotonic DMEM (I-DMEM). Regardless of a type of additional solutes, a fluid-filled domes (F-domes) appeared in bHS (Figure 4.3B-D). In contrast, cell sheets remained flat in IS. Consistent with the previous reports (Latorre et al., 2018; Leighton et al., 1969), F-domes repeatedly collapsed and reformed (Figure 4.3E; Movie 4.1). Once a dome is formed, the structure is maintained *in vivo* (Chin et al., 2017; Walton et al., 2016a). Therefore, the experimental system without ECM was not adequate to imitate *in vivo* dome formation.

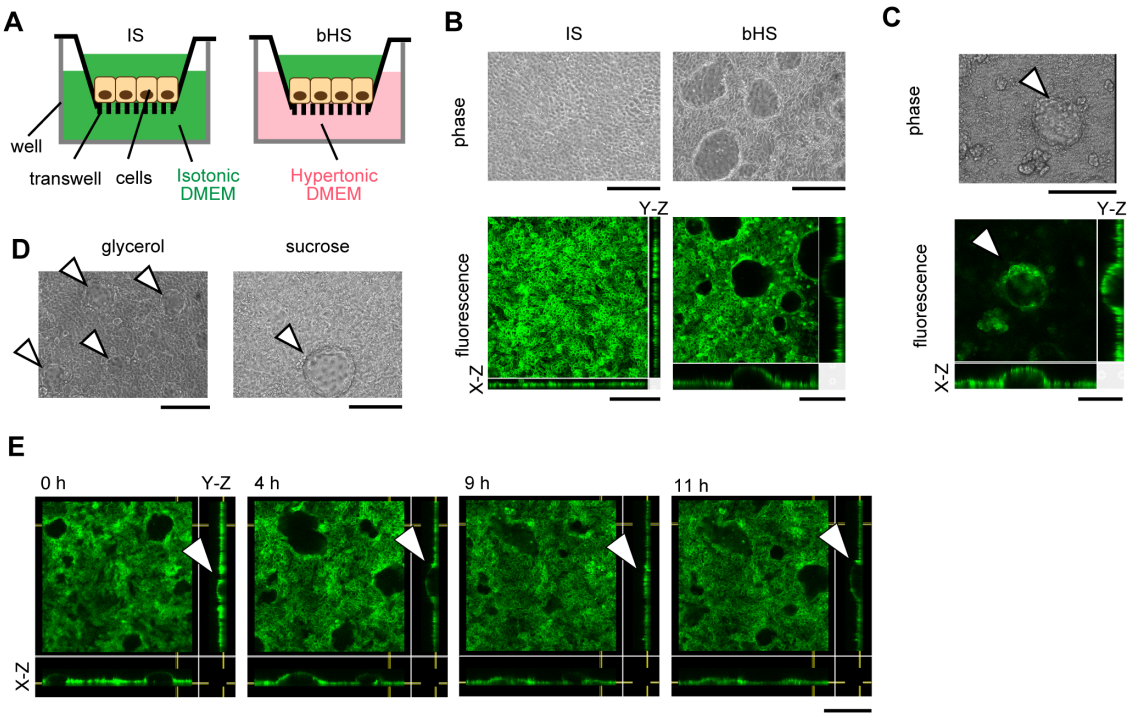

Figure 4.3 Fluid filled domes were induced by bHS

(**A**) The experimental system to apply basal hypertonic stress (bHS) and isotonic stress (IS) to MDCK sheet. Green and pink indicate isotonic DMEM and hypertonic DMEM, respectively. (**B**) Phase contrast and fluorescent images of confluent MDCK sheets on 0.4 μm pore membrane in IS or bHS. (**C**) The same area was taken with phase-contrast and confocal microscopy. Arrowheads

indicate the same F-domes. (**D**) F-domes appeared in bHS with addition of glycerol or sucrose. (**E**) 3D live cell imaging of F-domes in bHS. Arrowheads indicated the collapse and reform of F-domes. Green, MDCK-CAAX. Scale bars, 200 μm Images are the representatives.

4-2-3. Osmotic Treatment to MDCK Cells on ECMs

We tried to improve the experimental system by putting ECM under cells (Figure 4.4A). First, we tried to coat thin ECM on the surface of transwell. F-domes appeared on Matrigel coat and fibronectin coat, however, the domes collapsed (Figure 4.4B). Next, we tried gel substrate, which is richer in ECM than coating. We put collagen gel with different collagen concentration. Results showed that no dome appeared in response to bHS (Figure 4.4C). Then cells were seeded Matrigel or Matrigel High Concentration (MatrigelHC). MDCK sheet on Matrigels were perforated and the holes did not close with longer incubation time (Figure 4.4D), while dome formation *in vivo* begins from a nonporous monolayer. When the Matrigel and collagen gel was mixed, cell did not spread out with the rate of Matrigel: Collagen gel = 5:1 (Figure 4.4E). Confluent sheet was generated on the mixed gel with the ratio of Matrigel: Collagen gel = 1:1 or 2:1, however, sheet remained flat in bHS.

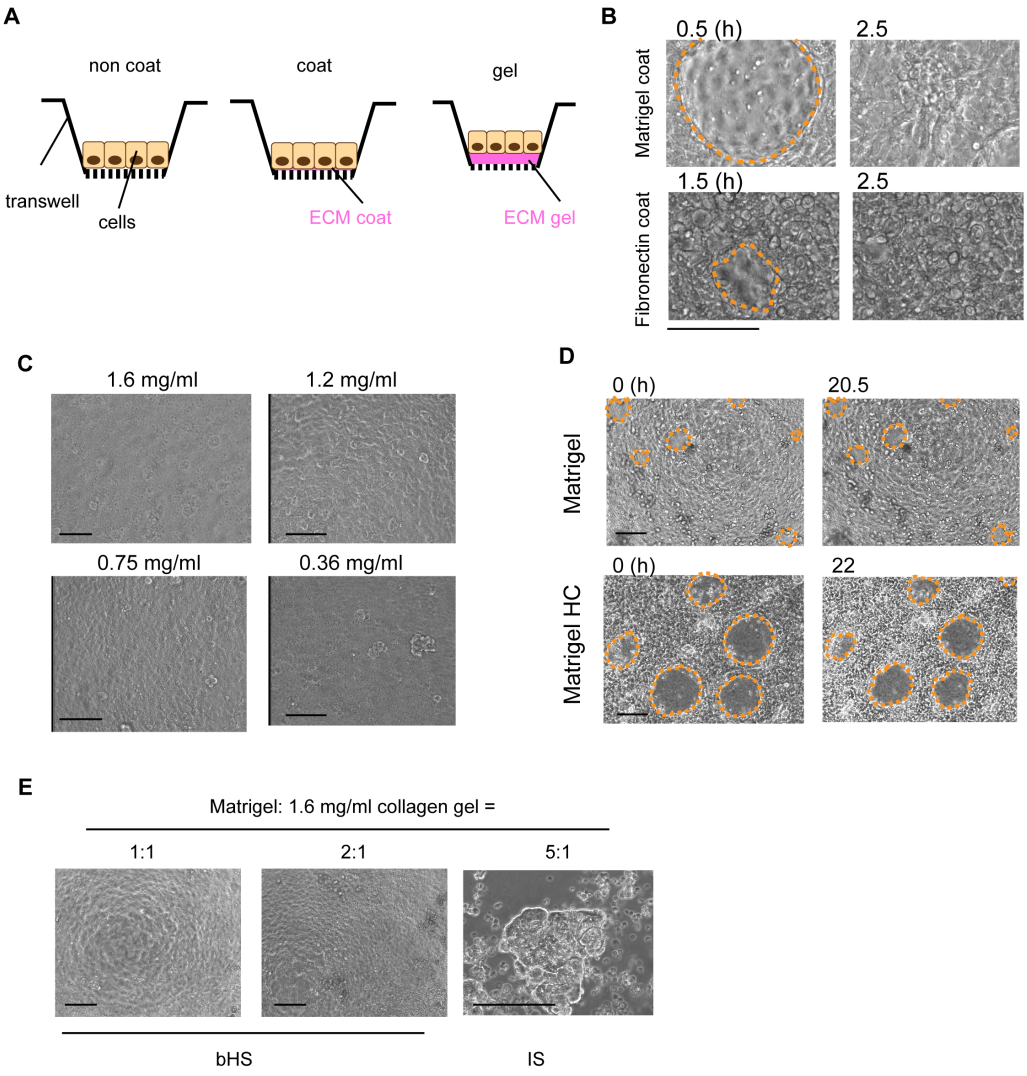

Figure 4.4 Trial and error of ECMs for support dome structures were performed.

(**A**) Experimental system of the transwell with ECM substrate. Pink indicate the ECM. (**B**) Time-lapse phase contrast images of MDCK sheets in bHS on 1:25 diluted Matrigel coat and on 50 μg/ml fibronectin coat. Orange dashed lines indicate the peripheries of F-domes. (**C**) Phase contrast images of MDCK sheets cultured with bHS on collagen gel with indicated collagen concentration. (**D**) Time-lapse phase contrast images of MDCK sheets on Matrigel or MatrigelHC in IS. Orange dashed lines indicate the hole of MDCK sheets. (**E**) Phase contrast images of MDCK sheets on the mixed gel of Matrigel and collagen gel. The cells were incubated in IS or bHS. Scale bars, 100 μm (B,C) and 200 μm (D,E).

4-2-4. Genipin Treatment to Matrigel

The MDCK sheet was perforated on Matrigel (Figure 4.4D), therefore we

modulated the mechanical property of Matrigel because we previously reported that mechanical properties of Matrigel affect MDCK morphologies (Imai et al., 2015; Ishida et al., 2014). Genipin (GP) is less-cytotoxic cross-linker that modulated mechanical properties of ECM gels (Sundararaghavan et al., 2008; Tsai et al., 2000). Matrigel was treated with GP with different concentration. GP crosslinking has three unique outcomes follows: (1) the color of gel turns blue after GP crosslinking (Lee et al., 2003; Mi et al., 2000; Muzzarelli et al., 2015; Sundararaghavan et al., 2008; Takami and Suzuki, 1994); (2) GP-crosslinks absorb 590 nm light; and (3) GP-crosslinks emits strong red fluorescence (Excitation/Emission 510-560/590 nm, and Excitation/Emission 590/630 nm) (Hwang et al., 2011; Muzzarelli et al., 2015; Sundararaghavan et al., 2008). Consistent with these, the color of the Matrigel changed from pick to blue after GP treatment (Figure 4.5A), and the absorbance at 595 nm and red fluorescence (Excitation/Emission 561/604 nm) increased with the increasing concentration of GP (Figure 4.5B,C). The absorbance and GP-crosslinks show a positive correlation (Hwang et al., 2011; Sundararaghavan et al., 2008). In previous reports, longer incubation time was found to increase the GP cross-linking within a gel. However, with our methods, GP-crosslinks did not increased from 2 day to 3 day incubation in 0.25 mM and 0.63 mM GP concentration. When we prepared GP-treated Matrigel (GP-Matrigel), GP solution was mixed with ice-cold liquefied Matrigel at the indicated final concentration, rather than immersing the gelated Matrigel in GP solution. The immersion technique provides abundant GP to gels, therefore, longer incubation time increases the crosslinks. On the other hand, the amount of GP was limited in our methods; thus, 0.25 mM and 0.63 mM GP in Matrigel may be almost completely crosslinked for 2 days incubation. The difference of fluorescence intensity between 1.0 mM and 0.63 mM GP-Matrigel was very small but significant. This is thought to be because the fluorescent became saturated in high GP concentration.

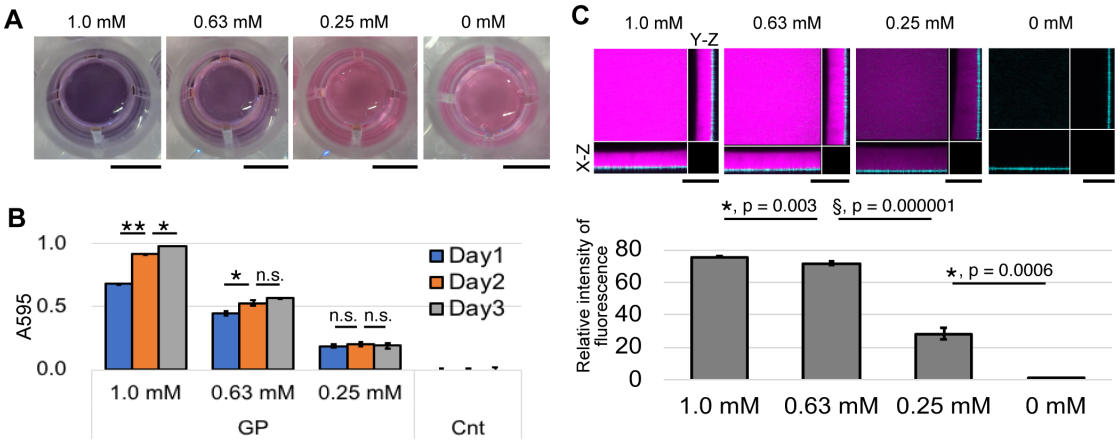

Figure 4.5 GP crosslinked Matrigel

(**A**) Images of Matrigel with the treatment of different GP-concentration. Scale bars, 5 mm. (**B**) The absorbance values at 595 nm wavelength of GP-Matrigels. The values were measured at daily intervals. n=3 independent experiments. Mean±S.D. n.s., no significance. *, p<0.05. **, p<0.0001 (student t-test with Bonferroni correction). (**C**) Fluorescent images of GP-Matrigels with different GP concentrations captured at a constant laser power. Graph of fluorescent intensity (Excitation/Emission = 561 nm/603 nm). n=3 independent experiments. Mean±S.D *, student t-test. §, welch t-test. Magenta, GP-Matrigel. Cyan, the membrane of transwell. Scale bars, 5 mm (A) and 500 μm (B,C). Images are the representatives.

Then we investigate whether the GP treatment modulate the mechanical properties of GP-Matrigel. Previous study reported that GP increases the viscosity of Matrigel. Stainless ball was dropped to Matrigel and the viscosity of Matrigel was estimated from the falling velocity of the ball. The falling velocity of the ball tended to decrease in 0.25 mM GP-Matrigel compared to non-treated Matrigel, which demonstrates that the viscous moduli of the gel increased (Figure 4.6A-C). Stainless ball did not fall into GP-Matrigel and left the track of its falling with 0.5 mM and more GP concentration (Figure 4.6D). To measure viscosity from the falling velocity of the ball, the ball should be surrounded by the substrate. Therefore, the viscosity of the 0.5 mM and more GP-Matrigel was incalculable in this study.

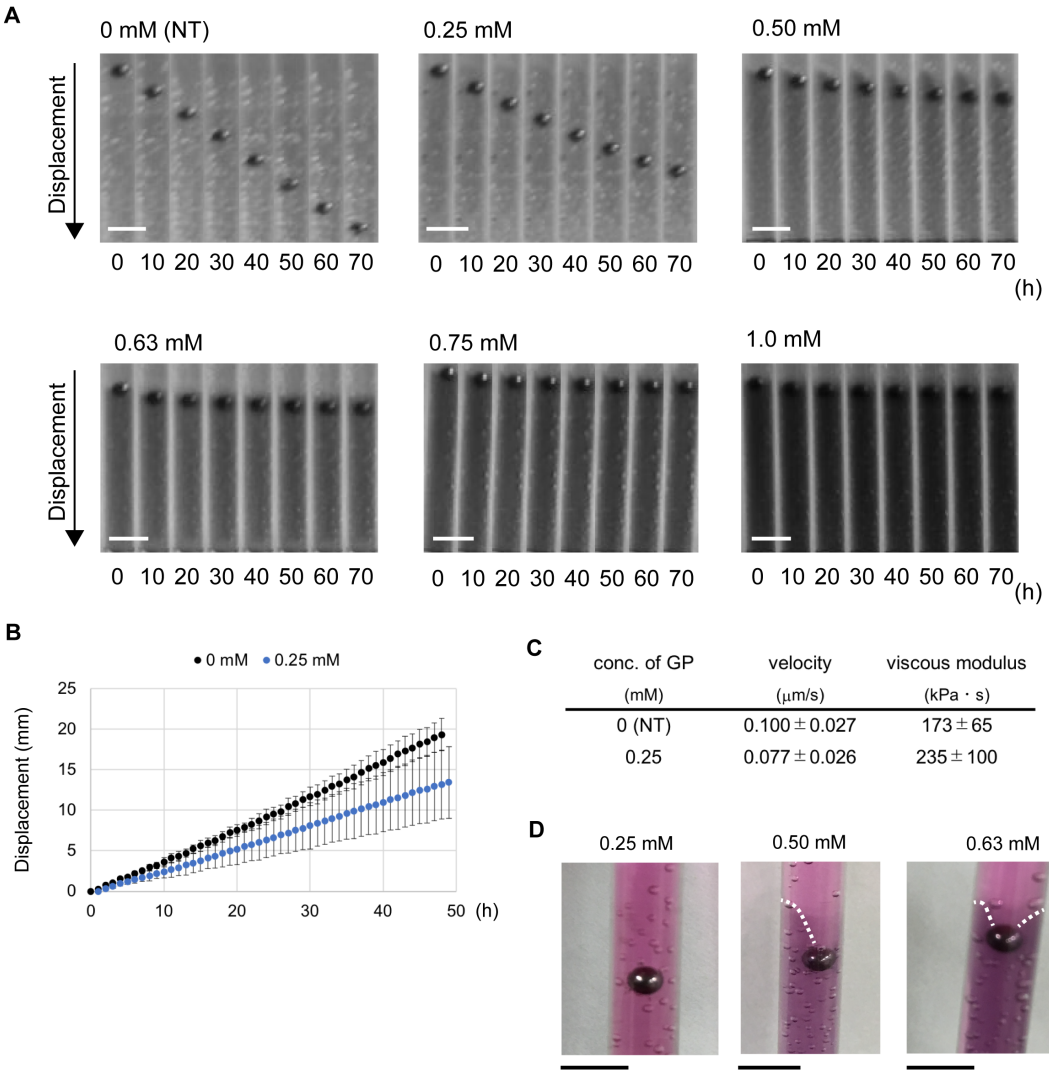

Figure 4.6 The viscosity of GP-Matrigel was measured with ball falling analysis

(**A**) Kymographs of the ball falling analysis with Matrigel with the treatment of different GP-concentration. (**B**) Time-displacement plot of stainless ball through Matrigel with 0 mM and 0.25 mM GP. The horizontal axis is the relative observation time and the vertical axis is the relative displacement of the balls. *n*=3 independent experiments. Mean±S.D. (**C**) Mean velocities of stainless balls and the viscous moduli of non-treated Matrigel and 0.25 mM Matrigel. (**D**) The enlarged image of stainless balls after 3 days observation of ball falling analysis. White dashed lines indicate the surface of GP-Matrigel. Scale bars, 5 mm. Images are the representatives.

Because the stainless ball did not move into GP-Matrigel with 0.5 mM and more (Figure 4.6D), we next examined the fluidity and relaxation time of GP-Matrigel. Previously, our laboratory examined the fluidity of non-treated Matrigel (Appendix 4;

performed by Dr. Misako Imai). Non-treated Matrigel was gelated at 37°C and holes were made by the suction with an aspirator. With the 3 days incubation at 37°C, the surface of non-treated Matrigel flattened out, indicating Matrigel has fluidity at 37°C. To examine the fluidity of 0.63 mM GP-Matrigel, the stainless ball was place onto the GP-Matrigel and then removed after 2 days incubation. Immediately after the removal, the visible holes left on 0.63 mM GP-Matrigel (Figure 4.7A). Furthermore, the deformation remained for two weeks. This indicates that the fluidity of the Matrigel reduced by GP treatment.

Next, we examined the relaxation time of GP-Matrigel. The stainless ball was placed onto the GP-Matrigel, removed after various incubation time, and then the deformation was observed. When the ball was removed immediately after placed, the surface of the gel did not show deformation (Figure 4.7B). With 5 to 10 min incubation, the surface remained deformed even after the ball was removed, suggesting the relaxation time may be 5 to 10 min in this experimental condition.

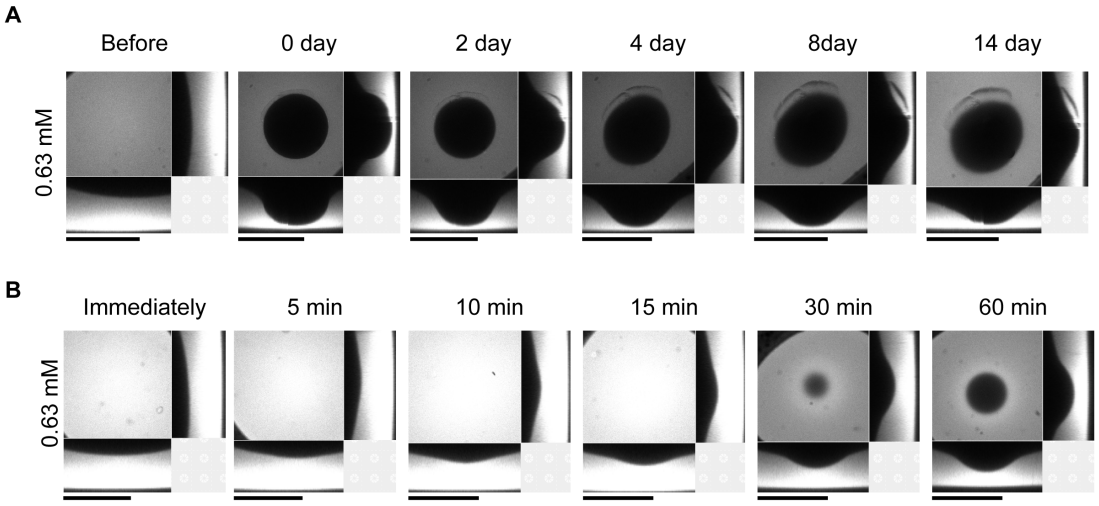

Figure 4.7 The fluidity and relaxation time was observed with the stainless balls

(**A**) Fluorescent images of 0.63 mM GP-Matrigel after removing stainless balls. Images are taken before the ball setting (Before) and then taken on indicated day after the ball removal. (**B**) Fluorescent images of 0.63 mM GP-Matrigel after removing balls with indicated incubation time. Images were taken immediately after the ball removal. White, GP-Matrigel. Scale bars, 5 mm. Images are the representatives.

We next examined the change in the elasticity of GP-Matrigel with atomic force microscopy (AFM). AFM measures the elasticity of substrate from a bending degree of a cantilever (Appendix 5; performed by Dr. Seiishiro Ishihara). The results showed that the elasticity of Matrigel tended to increase in GP concentration dependent manner. These data suggest that GP made crosslinks within Matrigel and modulated the viscoelasticity of Matrigel.

As a result of cell seeding onto GP-Matrigel, the pores did not appear on GP-Matrigel with 0.25 mM and more (Figure 4.8). Because the GP concentration affect the 3D morphogenesis of MDCK cells (Imai et al., 2015), we investigated the dome formation with non-porous monolayer on 0.25 mM or more GP-Matrigel.

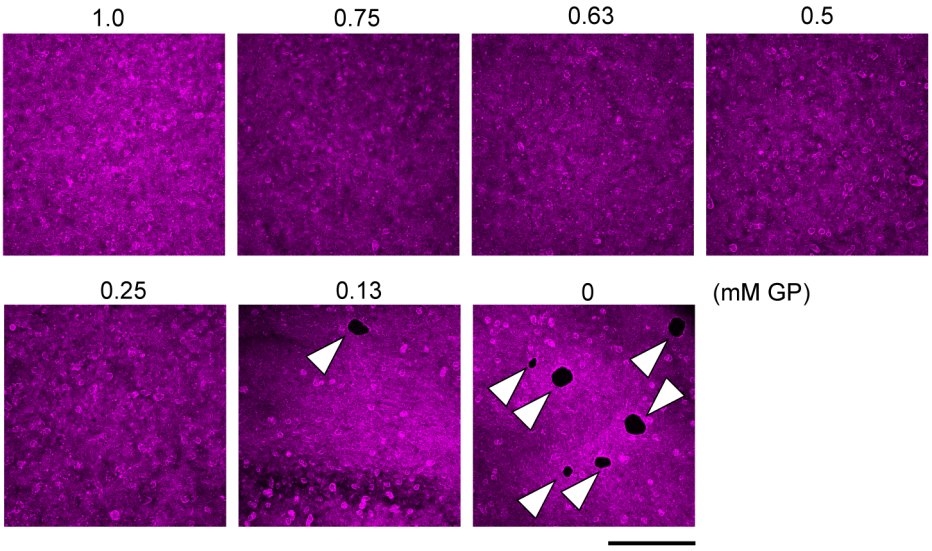

Figure 4.8 The MDCK sheets became confluent on 0.25 mM and more GP-Matrigel.

Max intensity images of fluorescent staining of MDCK sheets cultured on GP-Matrigel. Arrowheads indicated the hole in MDCK monolayer. Magenta, F-actin. Scale bar, 1 mm. Images are the representatives.

4-2-5. Stable Gel-Filled Dome Formation on GP-Matrigel

Using an improved experimental system with GP-Matrigel, MDCK sheets were exposed to osmotic gradient (Figure 4.9A). After overnight incubation in bHS, multiple round structures appeared on 0.75, 0.63, 0.50 mM GP-Matrigel (Figure 4.9B). Hereafter, GP was used at 0.63 mM, unless a different concentration was mentioned.

The round structures were identified as domes by 3D fluorescent observation and the domes were larger than F-domes (Figure 4.9C-E; Movie 4.2). In addition, the overexposed image of GP autofluorescence have shown that the interior of these domes was filled with GP-Matrigel (Figure 4.9F). From here onward, these domes are referred as gel-filled domes (G-domes). The G-domes did not appear on porous MDCK sheets (Figure 4.9G). Furthermore, the osmotic gradient was maintained through the F-dome formation (Figure 4.9H). On 0.25 mM GP-Matrigel, the cells generated the larger G-domes than 0.63 mM (Figure 4.9B-C). One or two domes appeared in the transwell, which the gel partially detached from the membrane. In contrast, no dome appeared on 1.0 mM GP-Matrigel (Figure 4.9B-C).

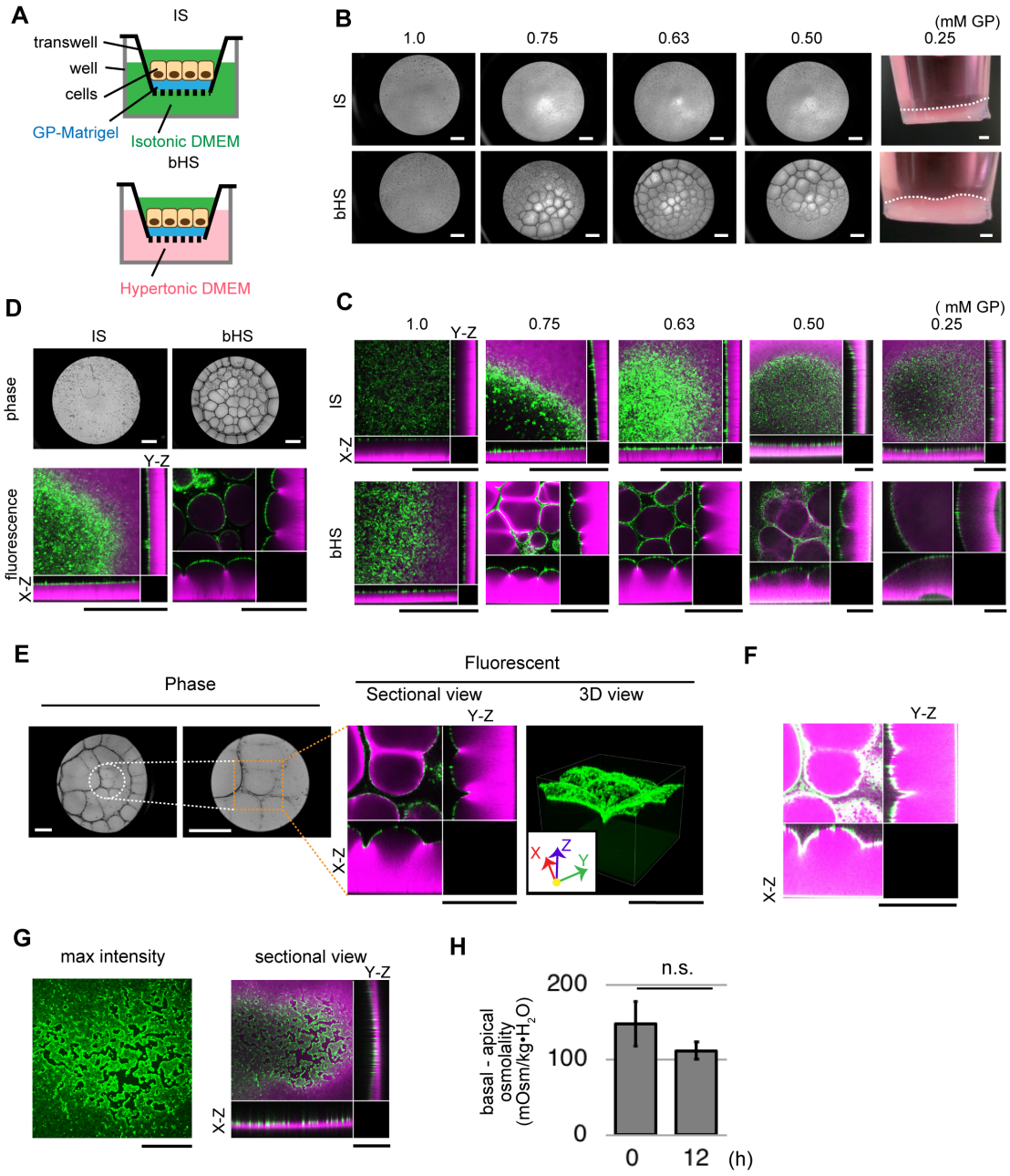

Figure 4.9 Gel-filled domes (G-domes) were induced to confluent MDCK sheets in bHS on Matrigel with certain GP concentration.

(**A**) Improved experimental system to expose MDCK sheet with osmotic gradient on GP-Matrigel. Green, pink and blue indicate I-DMEM, H-DMEM and GP-Matrigel, respectively. (**B-C**) Phase contrast (B) and 3D fluorescent (C) images of MDCK-CAAX sheet on GP-Matrigel with different GP concentration. The sheet was incubated in IS or bHS overnight. (**D**) Phase contrast and fluorescent images of MDCK-WT sheet on 0.63 mM GP-Matrigel with overnight incubation in bHS. Green, calcein-AM. Magenta, GP-Matrigel. (**E**) Phase contrast and fluorescent images of the same

area of G-domes on 0.75 mM GP-Matrigel. White and orange dashed line indicate the enlarged and fluorescent view, respectively. (**F**) The overexposed image of fluorescent sectional view in (E). (**G**) Fluorescent images of porous MDCK-WT sheet on 0.63 mM GP-Matrigel incubated with bHS. Maximum intensity image shows only with green. (**H**) Quantification of the osmolality difference between 0 h and 12 h after bHS treatment on 0.63 mM GP-Matrigel. $n = 3$ independent experiments. Mean±S.D. n.s., nonsignificant (Student's *t*-test. See details in section 2-4). (B, C, E, F) Green, calcein-AM. Magenta, GP-Matrigel. Scale bars, 1 mm. Images are the representatives.

We next confirmed whether the basal hypertonic stress is necessary for G-dome formation. When the osmotic gradient was higher in apical side (Figure 4.10A). G-domes did not appear. Hypertonic stress was applied to both apical and basal side, which had no osmotic gradient, G-domes did not appear, neither. Even when the cells incubated in bHS, domes disappeared with decrease of additional mannitol to basal compartment (Figure 4.10B). As long as the difference of osmolality is high enough, G-domes appeared regardless of absolute values of the osmolality, a type of additional solutes, and size of the transwell (Figure 4.10C-E).

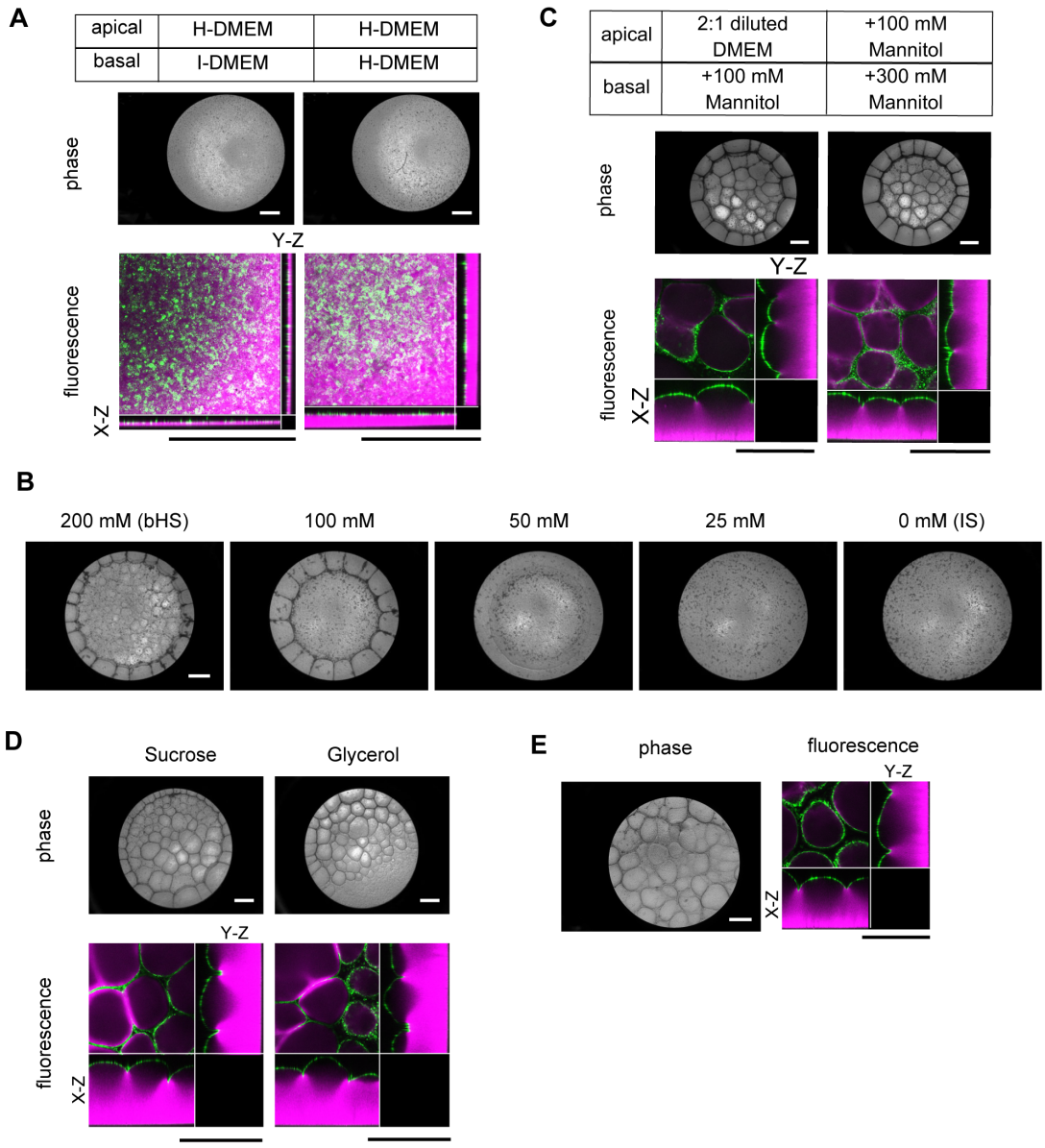

Figure 4.10 bHS was essential for G-dome formation

(**A**) MDCK-CAAX sheets on 0.63 mM GP-Matrigel incubated with hypertonic stress in apical and both sides. (**B**) MDCK-CAAX sheet on 0.63 mM GP-Matrigel in bHS with different concentration of additional mannitol. (**C**) G-domes on 0.63 mM GP-Matrigel generated by the same osmotic difference with different osmolality. MDCK-WT was used. Green, calcein-AM. Magenta, GP-Matrigel. (**D**) G-domes on 0.63 mM GP-Matrigel in bHS with sucrose or glycerol. (**E**) G-domes on 0.63 mM GP-Matrigel in bHS cultured in 12-well transwell. (A, D, E) Green, MDCK-CAAX. Magenta, GP-Matrigel. Scale bars, 1 mm. Images are the representatives (A-D).

Furthermore, time-lapse observation revealed that G-domes did not collapse,

but the structures were maintained throughout 24 h observation (Figure 4.11A; Movie 4.3). After G-domes were formed, the structures were persisted with the removal of bHS (Figure 4.11B). When G-domes were continuously exposed to bHS, they gradually grew into a large dome over the next several days (Figure 4.11C-E). These results demonstrated that bHS induces G-dome on Matrigel with a certain concentration of GP, and that GP-Matrigel provides stability to the dome structures.

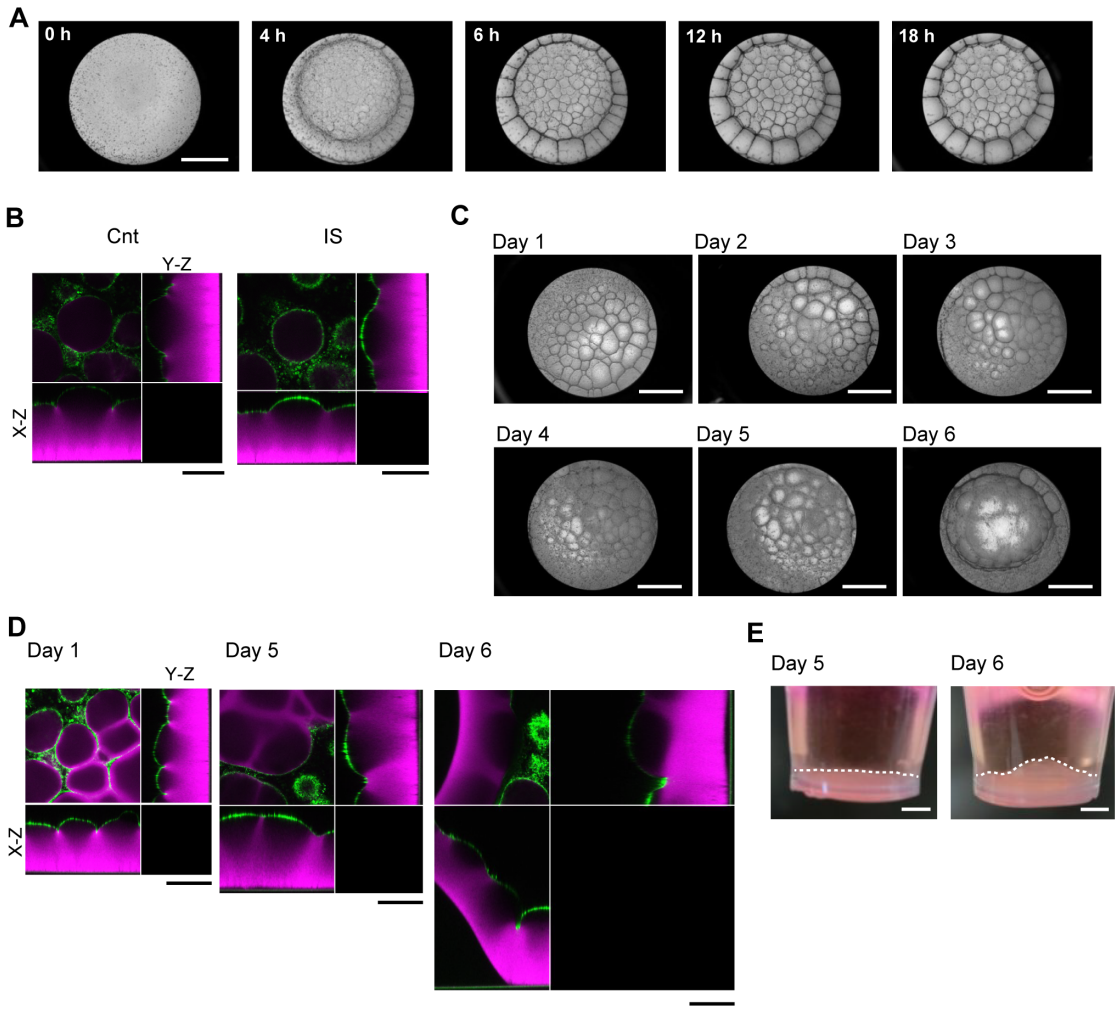

Figure 4.11 G-domes obtained stability

(**A**) Time-lapse observation of G-dome formation by phase contrast microscopy. (**B**) G-domes before (Cnt) and after (IS) the removal of bHS. (**C-E**) Phase contrast (C) and fluorescent (D) images of G-domes that continuously exposed in bHS. Photo images of the side view of transwell are shoen in (E). White dashed line indicate the surface of the MDCK sheet. Green, MDCK-CAAX. Magenta, GP-Matrigel. Scale bars; 2 mm (A,C,E), 500 μm (B,D). Images in A-C,E are representative.

4-2-6. Biased Gel Swelling during G-dome Formation

To further investigate the process of the G-dome formation, 3D live imaging was performed with fluorescent beads to monitor the deformation of substrates. The movie showed that the gel swelled uniformly in the early stages of G-dome formation (Figure 4.12A; Movie 4.4). Moreover, the swelling stopped in some area, resulting in the appearance of G-domes. The beads in the gel moved the axis perpendicular to the cell sheet with the G-dome appearance (Figure 4.12B; Movie 4.5). The final swelling degree of 0.63 mM GP-Matrigel was significantly higher in bHS compared to in IS (Figure 4.12C). On the other hand, 1.0 mM GP-Matrigel in bHS, in which no domes generated, showed the significantly lower swelling rate than 0.63 mM in bHS. Without seeding cells, 0.63 mM GP-Matrigel neither showed G-dome formation nor swelled in response to bHS even though the osmotic gradient was maintained (Figure 4.12D,E). These results suggest that bHS promotes cells to swell the GP-Matrigel for G-dome morphogenesis.

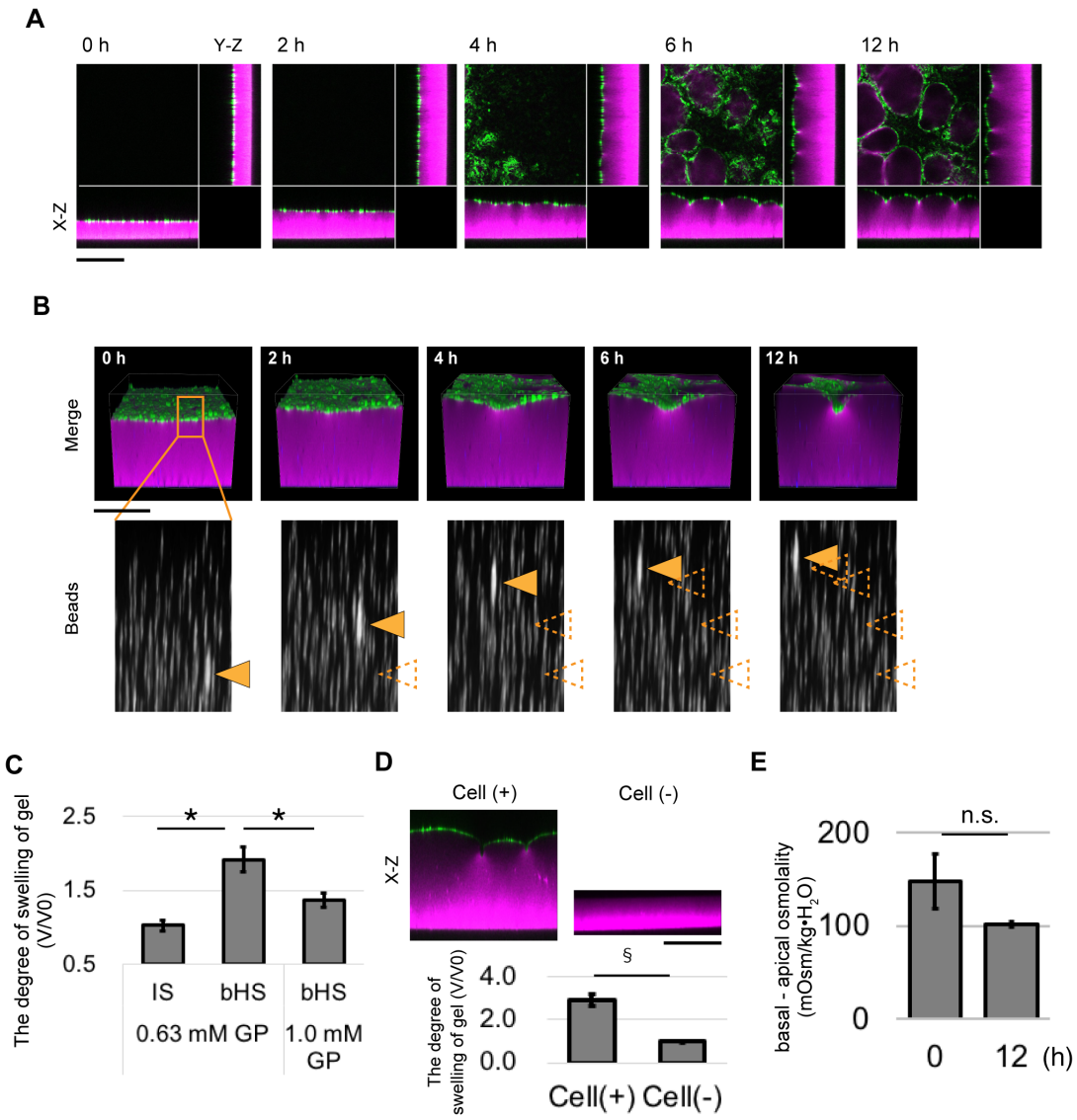

Figure 4.12 GP-Matrigel ununiformly swelled during G-dome formation

(**A**) Time development of G-dome formation on 0.63 mM GP-Matrigel. (**B**) The movement of fluorescent beads in 0.63 mM GP-Matrigel. Orange lines indicates the enlarged view with extraction of beads images. Arrowheads track the same beads. (**C**) The gel swelling analysis of GP-Matrigel with MDCK sheets. n = 3 independent experiments. (**D**) The Z-sectional images and swelling analysis of 0.63 mM GP-Matrigel with cells and without cells. n = 4 independent experiments. (**E**) Quantification of the difference in osmolality between 0 h and 12 h after bHS treatment without cells, using 0.63 mM GP-Matrigel. n = 3 independent experiments. Mean±S.D. *, p<0.05 (Student's t-test with Bonferroni correction). §, p< 0.01 (Welch's t-test). n.s., nonsignificant (Welch's t-test). Green, MDCK-CAAX. Magenta, GP-Matrigel. Scale bars, 500 μm. Images are the representatives.

4-2-7. Cell Height-dependent AQPs Water Transport for the Gel Swelling

Matrigel is the hydrogel that contains ionic groups. The swelling degree of hydrogel containing ionic groups is greatly affected by the ionic strength of a solution (Quesada-Perez et al., 2011). AQPs are water-channel proteins of cells and transport water in presence of osmotic gradient (Deen et al., 1997; Verkman, 2011).We hypothesized that AQPs water transport from apical medium to basal GP-Matrigel causes the reduction of ion strength within the gel and leads to gel swelling. To examine this hypothesis, we measured whether cells transport water in bHS. When the water is transported from the apical to basal side, the concentration of phenol red in apical medium increases (Jovov et al., 1991). For 0.63 mM GP-Matrigel, apical phenol red was significantly condensed in bHS than in IS, whreas apical phenol red did not changed by GP concentration in Matrigel in bHS (Figure 4.13A,B). $HgCl_2$, a broad inhibitor of AQPs (Bai et al., 1996; Deen et al., 1997; Ishibashi et al., 1994), prevented the water transport, the gel swelling, and the G-dome formation (Figure 4.13C-E). In addition, water influx to GP-Matrigel by immersion in pure water without seeding cells resulted in uniform swelling and the surface of the gel remained flat (Figure 4.13F). The presence of $HgCl_2$ did not influenced the swelling of GP-Matrigel in pure water (Figure 4.13G). In pure water, the surface elasticity of the gel tended to increase (Appendix 5), which consistent with a previous study that showed that hydrogel becomes stiffer under highly swollen conditions (Hoshino et al., 2018). These data suggested that cellular water transport by AQPs heterogeneously swells the GP-Matrigel in the formation of G-dome.

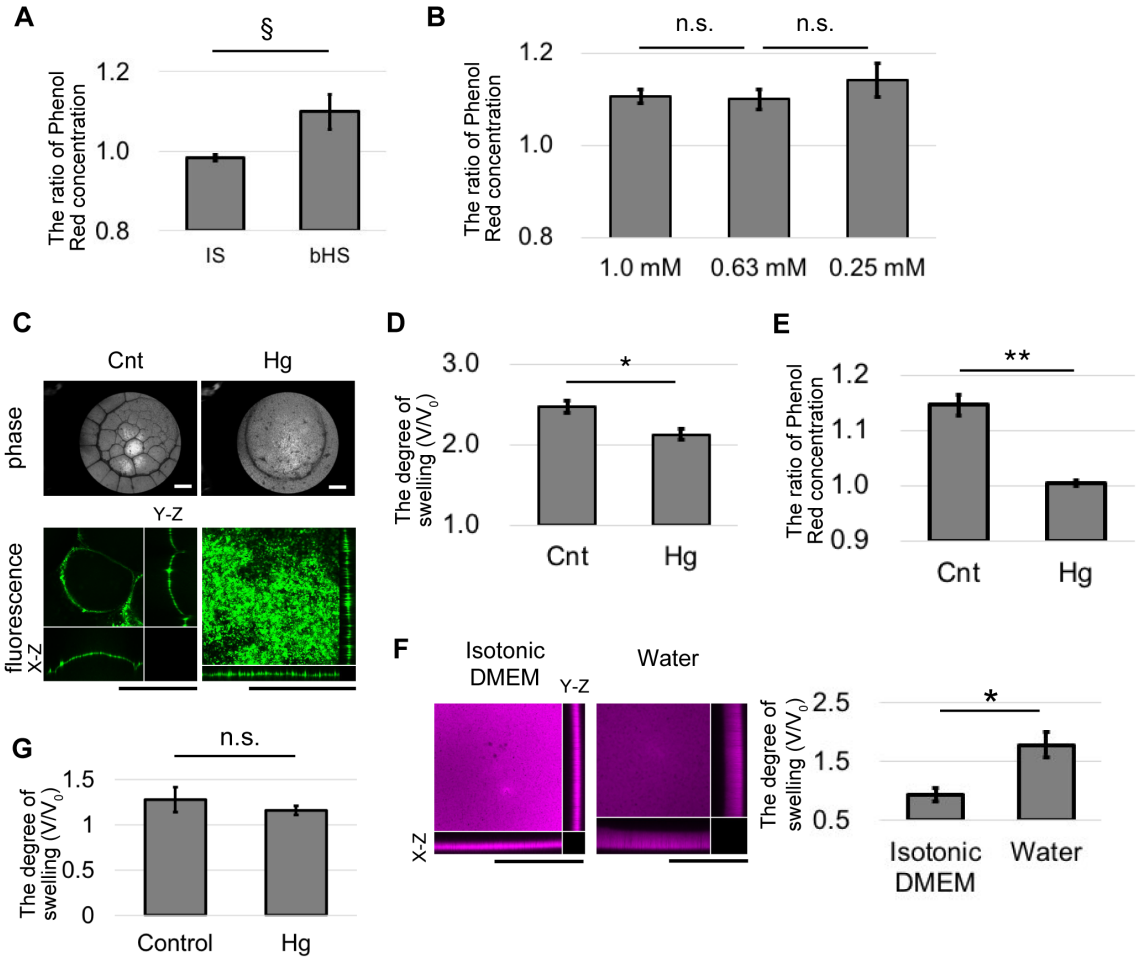

Figure 4.13 Cells transport water via AQPs for G-dome formation

(**A**) Water transport analysis of MDCK-WT sheets on 0.63 mM GP-Matrigel in IS or bHS. n = 6 independent experiments. (**B**) Water transport analysis of MDCK-WT sheets in bHS cultured on GP-Matrigel with different GP concentration. n = at least 2 independent experiments. (C and D) Images (**C**) and gel swelling analysis (**D**) of MDCK-WT cells on 0.63 mM GP-Matrigel in presence (Hg) and absence (Cnt) of 0.1 mM $HgCl_2$. Green, calcein-AM. n = 3 independent experiments. (**E**) Water transport analysis of MDCK-WT sheets on 0.63 mM GP-Matrigel in bHS with 0.1 mM $HgCl_2$ (Hg) treatment. n = 3 independent experiments. (**F**) Images and gel swelling analysis of 0.63 mM GP-Matrigel without cells after immersion in isotonic DMEM or pure water. n = 6 independent experiments. Magenta, GP-Matrigel. (**G**) Gel swelling analysis of GP-Matrigel immersed in pure water in absence (Control) and presence (Hg) of 0.1 mM $HgCl_2$. (A, B, D-G) Mean±S.D. n.s., nonsignificant. §, p<0.05 (Welch's t-test). *, p<0.01 (Student's t-test). **, p<0.001 (Student's t-test). Scale bars, 1 mm. Images are the representatives.

Aside from ionic strength, gel elasticity also modulates the swelling degree of hydrogel. The elasticity of the gel restricts the expansion of the polymer network during swelling (Quesada-Perez et al., 2011). Consistent with this, the stiffer GP-Matrigel showed decreased swelling degree in pure water (Figure 4.14). As the gel elasticity did not affect the AQPs water transport (Figure 4.13B), gel swelling was prevented by limiting gel expansion, not by reducing water transport. These suggest that no domes appearance on 1.0 mM GP-Matrigel may be due to the inhibition of the gel swelling of stiffer gel.

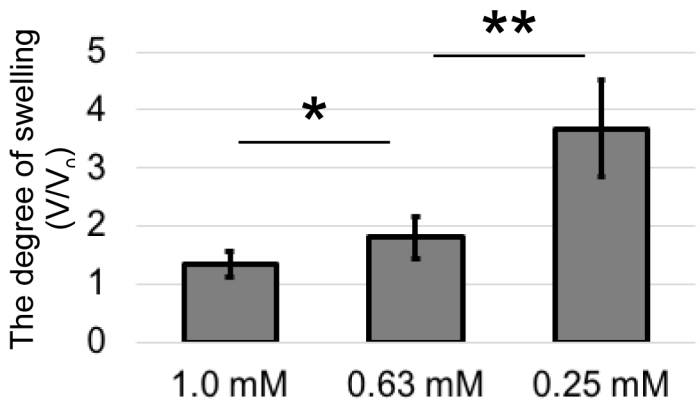

Figure 4.14 Stiffer GP-Matrigel showed decreased degree of swelling.

Gel swelling analysis of GP-Matrigel immersed in pure water. Cells were not seeded. n = at least 3 independent experiments. Mean±S.D. *, $p<0.05$. **, $p<0.01$ (student t-test with Bonferroni correction).

To investigate the mechanism by which cells transport water in dome-shaped formation, we focused on non-uniform swelling, as observed in Figure 4.12A. Cells of F-domes were stretched and became thinner than those in flat regions (Figure 4.15) (Latorre et al., 2018). Moreover, stretch stimuli are known to enhance AQP-1 expression (Baetz et al., 2009). Before the osmotic treatment, we found the cell height was not uniform in MDCK sheets (Figure 4.16A). Because the stretched cell became thinner (Figure 4.15), we hypothesis the heterogeneous swelling occurs as follows: (1) the thinner cells transport more water in response to bHS, (2) the gel locally swelled by the transported water, (3) the swollen gel stretched the cells above, (4) the stretched cells increased water transport, (5) the feedback of (2) to (4) results in the

heterogeneous swelling in dome-shaped formation. To examine this, the correlation between cell thickness and water transport was investigated. Cells were seeded on to non-coat transwell with different cell density in order to obtain the cell sheet of different thickness Cells were thinner with lower cell density, and cells were thicker in higher cell density. For this experiment, transwell with 1.0 μm pores was used. On transwell with 0.4 μm pores, cell sheet generated F-domes in bHS (Figure 4.3), which causes cell flattening (Figure 4.15). For a yet unknown reason, F-domes did not appear on 1.0 μm pores. To exclude the additional cell thinning, the water transport of cell sheet with different thickness was investigated on 1.0 μm pores. The results showed that the thinner cells transported more water in bHS (Figure 4.16B,C). Next we examined whether cells become thinner at G-domes. Because the G-domes were too large to observe the single cell shape with high power objective lens, the cell thickness were observed from the cell density (Figure 4.16A). The nucleus was stained with live cell permeable dye, and observed in flat cell sheet in IS and G-domes in bHS (Figure 4.17A). The density of G-dome top was significantly smaller than both in flat sheet and at the G-dome edge. In addition, fixed cell sheets were stained with F-actin and inverted onto a glass cover slip in order to observe with high power objective lens. The fluorescent images showed that cell sheet became thinner in G-dome top than in IS (Figure 4.17B). To demonstrate the G-domes appeared from a thinner cell area, the cell density was tracked from 3D live imaging of the cell membrane. The results exhibited that the cell density was lower in the area of the future dome top than in the area of the future dome edge (Figure 4.17C). In addition, cell density at the future top decreased during G-dome formation and increased at the future edge (Figure 4.17D,E). These suggest that the swollen gel stretches the cells, as a result of this, cellular water transport is enhanced. Computer simulation also demonstrated the positive feedback between cell stretch and water transport plays a crucial role to generate domes by heterogeneous gel swelling (Appendix 6; performed by Dr. Masakazu Akiyama).

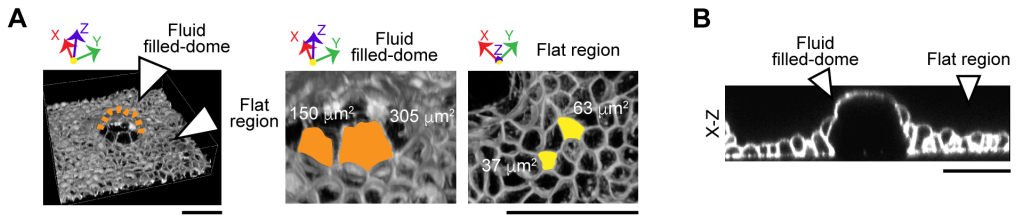

Figure 4.15 The cells in F-domes were stretched.

(**A**) 3D view of fluorescent images of a F-dome of MDCK-WT cells incubated on non-coat 0.4 μm pore transwells with bHS. Orange dashed line indicates the surface of the F-dome. Orange and yellow areas show the cell surface of the F-dome and the flat region, respectively. Each apical area is shown in the picture. (**B**) Sectional view of (A). White, F-actin. Scale bars, 50 μm.

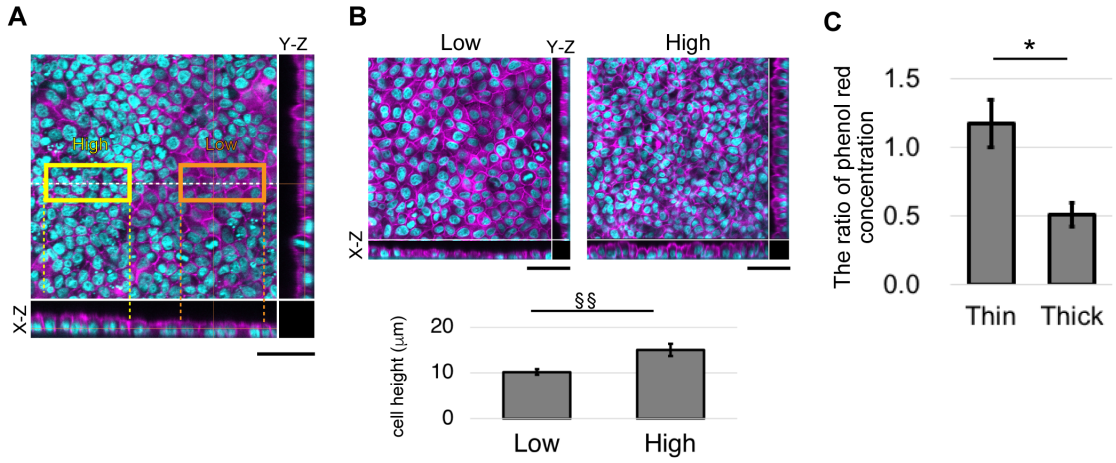

Figure 4.16 The thinner cells had higher water transport activity

(**A**) Fluorescent images of MDCK sheet on GP-Matrigel in IS before bHS treatment. White dashed line indicates where the Z-sectional view was created. Yellow and orange boxes showed the area with high and low cell density, respectively. Yellow and orange dot lines indicate the XZ-sectional view corresponded to each color boxes in XY section. (**B**) Fluorescent images and quantitative analysis of cell height with low or high cell density. Cells were seeded on non-coat 1.0 μm pore transwells and incubated in bHS for 9 h. $n = 9$ area from three independent experiments. Images are representatives. (**C**) Water transport analysis of non-coat transwell with thin or thick cells. $n = 3$ independent experiments. Mean±S.D. §§, $p<0.0001$ (Welch's t-test). *, $p<0.01$ (Student's t-test). Cyan, nucleus. Magenta, F-actin. Scale bars, 50 μm.

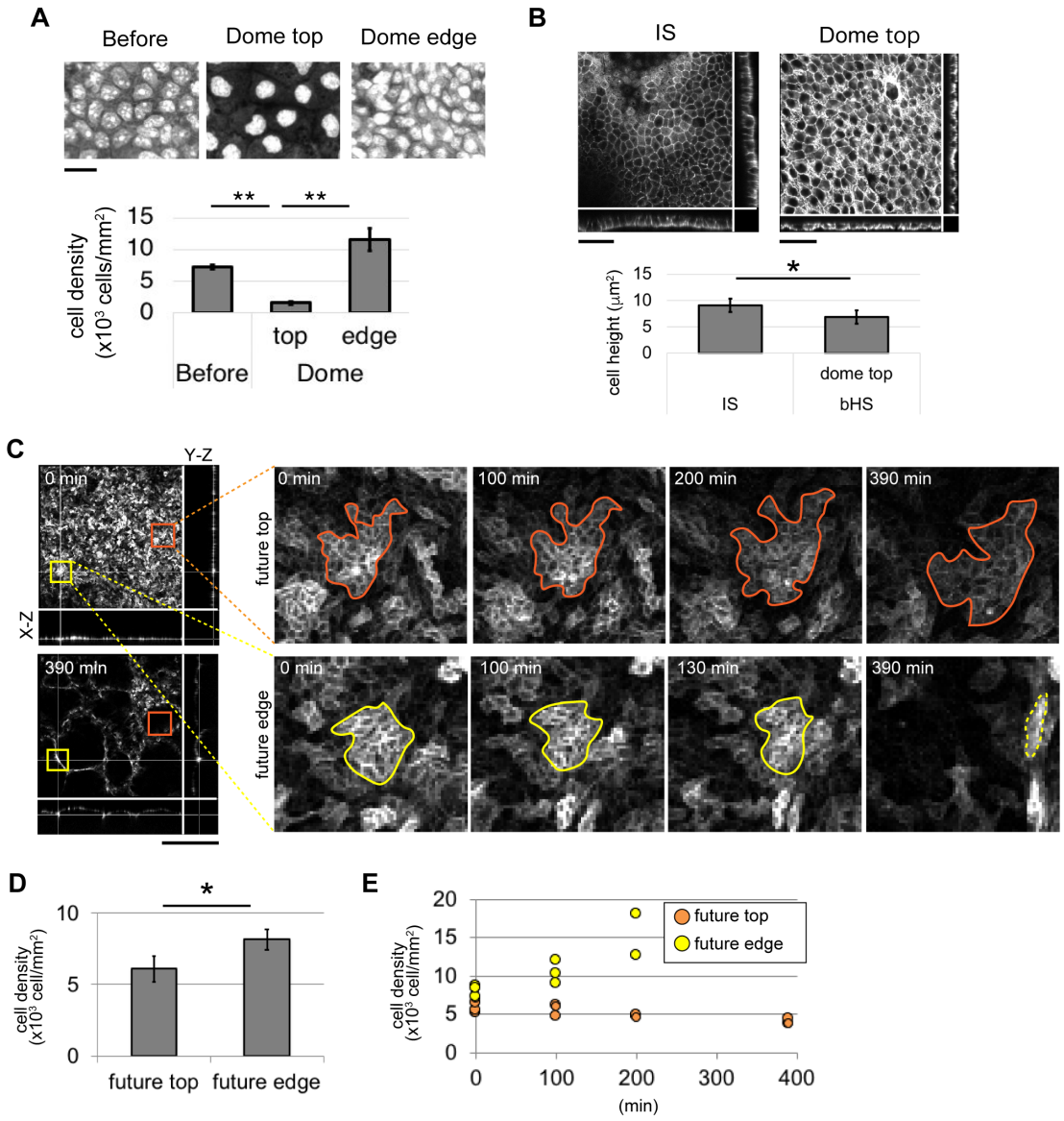

Figure 4.17 The cells became thinner at G-dome top.

(**A**) Fluorescent images of nucleus and cell density analysis on 0.63 mM GP-Matrigel. n = 9 regions from 3 independent experiments. Mean±S.D. *, p<0.01. **, p<0.0001 with Bonferroni correction (Student's t-test). Scale bar, 20 μm. Images are the representatives. (**B**) Fluorescent images of F-actin and cell height analysis of MDCK sheet on 0.63 mM GP-Matrigel. Scale bar, 50 μm. Images are the representatives. n = 15 cells from at least 1 experiment. Mean±S.D. *, p< 0.001 (Student's t-test). Scale bars, 50 μm. (**C**) 3D live imaging of the G-dome formation on 0.63 mM GP-Matrigel. Orange and yellow lines indicate the area of future G-dome top and future G-dome edge, respectively. Yellow dashed line indicates the unmeasurable state after aggregation of another area with strong fluorescence intensity. White, MDCK-CAAX. Scale bar, 500 μm. (**D**) Cell density

analysis of the area between the future top and future edge of G-domes at 0 h. *n* = at least 3 area from 1 experiment. Mean±S.D. *, $p<0.05$ (Student's *t*-test). (**E**) Cell density tracking of the area in the future top and future edge of G-domes. Orange and yellow dots represent future top and future edge, respectively. *n* = at least 2 area from 1 experiment.

4-2-8. Cell Volume Change by Cell Stretching

Stretch stimuli regulate cellular volume and contractility. Cell spreading reduces the volume and consequently modulates cellular behaviors, including cell cycle, differentiation and contractility (Bao et al., 2017; Guo et al., 2017; Neurohr et al., 2019). Therefore, we investigated whether stretching change the cell volume in MDCK monolayer. Cells were isotropically stretched using a silicone rubber chamber (Takemoto et al., 2015) that increased the cell area by 26% (± 13%) (Figure 4.18A). As the nucleus volume denotes the same tendency of the change in the cytoplasmic volume (Guo et al., 2017), we measured the volume of the nucleus and found it to be increased (26% ± 14%) in stretched cells (Figure 4.18*A*). In addition, cells were seeded onto a glass with difference cell density, as described in previous report (Guo et al., 2017), and the volume of nucleus was measured. The cell with larger adhesion area had increased volume of nucleus, showing the positive correlation (Pearson's correlation, 0.73) (Figure 4.18B). These results were contradictory to previous reports, which may be attributed to the different cell type as human mammary epithelial cells were used in previous reports.

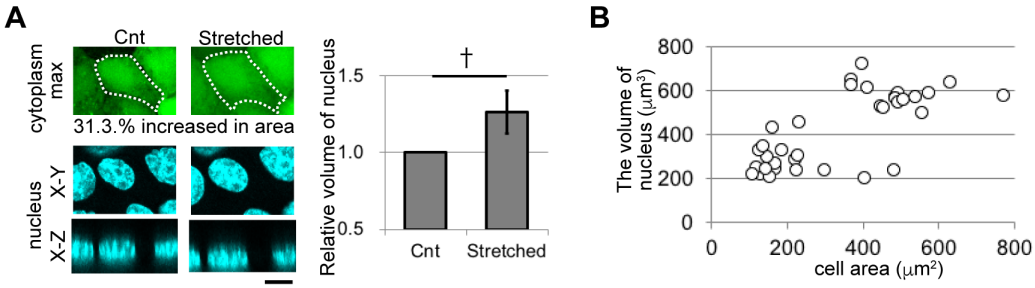

Figure 4.18 The stretched cells increased the volume of nucleus.

(**A**) Image and nucleus volume analysis of MDCK monolayer before (Cnt) and after (Stretched) cell stretching using a silicone rubber chamber. The same cells were tracked. Cytoplasm and nucleus were shown in max intensity and sectional image, respectively. White dot line represents the single cell area. Cyan, nucleus. Green, Calcein-AM. Scale bar, 10 μm. Images are representative. *n* = 26

cells from 1 experiment. Mean±S.D. †, significance by 99% confidence interval. (**B**) Nucleus volume analysis of MDCK cells seeded on glass with difference cell density. n = 35 cells from 1 experiment.

4-2-9. The Contribution of Cellular Traction Force to G-domes Formation

Stretch stimuli enhanced the cellular contractile force through actomyosin (Mizutani et al., 2009; Uyeda et al., 2011). We investigated the contribution of actomyosin in G-dome formation because actomyosin contractility, in general, plays a key role in morphogenesis (Diaz-de-la-Loza et al., 2018; Heisenberg and Bellaïche, 2013; Kasza and Zallen, 2011; Martin, 2010; Young et al., 1993). Myosin II generates contractility through the motor activity of myosin heavy chains following phosphorylation of the myosin regulatory light chain (MRLC) (Mizutani et al., 2006b). We performed immunofluorescence imaging for phosphorylated MRLC (P-MRLC) and inverted stained G-domes onto a coverslip to observe the localization of P-MRLC within the cells. Immunofluorescent imaging of mono-phosphorylated MRLC (1P-MRLC) and di-phosphorylated MRLC (2P-MRLC) were partially co-localized with F-actin before and after G-dome formation (Figure 4.19A,B). To evaluate the contribution of cellular contractile force, MDKC monolayer were treated with the inhibitor of actin polymerization (cytochalasinD; CytoD), inhibitor of myosin heavy chain (blebbistatin; Bleb), or inhibitor of phosphorylation of MRLC (Y27632). The cytoD treatment disrupted the integrity of MDCK monolayer, resulting in the perforated monolayer, possibly because F-actin functions to maintain epithelial integrity (Ivanov et al., 2010). G-domes did not appeared with porous monolayer (Figure 4.19C), the contribution of actomyosin was tested using blebbistatin and Y27632. Although Y27632 treatment decreased the phosphorylation level of MDCK cells (Figure 4.19D), neither blebbistatin nor Y27632 treatment did not affected the G-dome appearance (Figure 4.19E,F). These results indicate that the contribution of actomyosin contractile force is negligibly small.

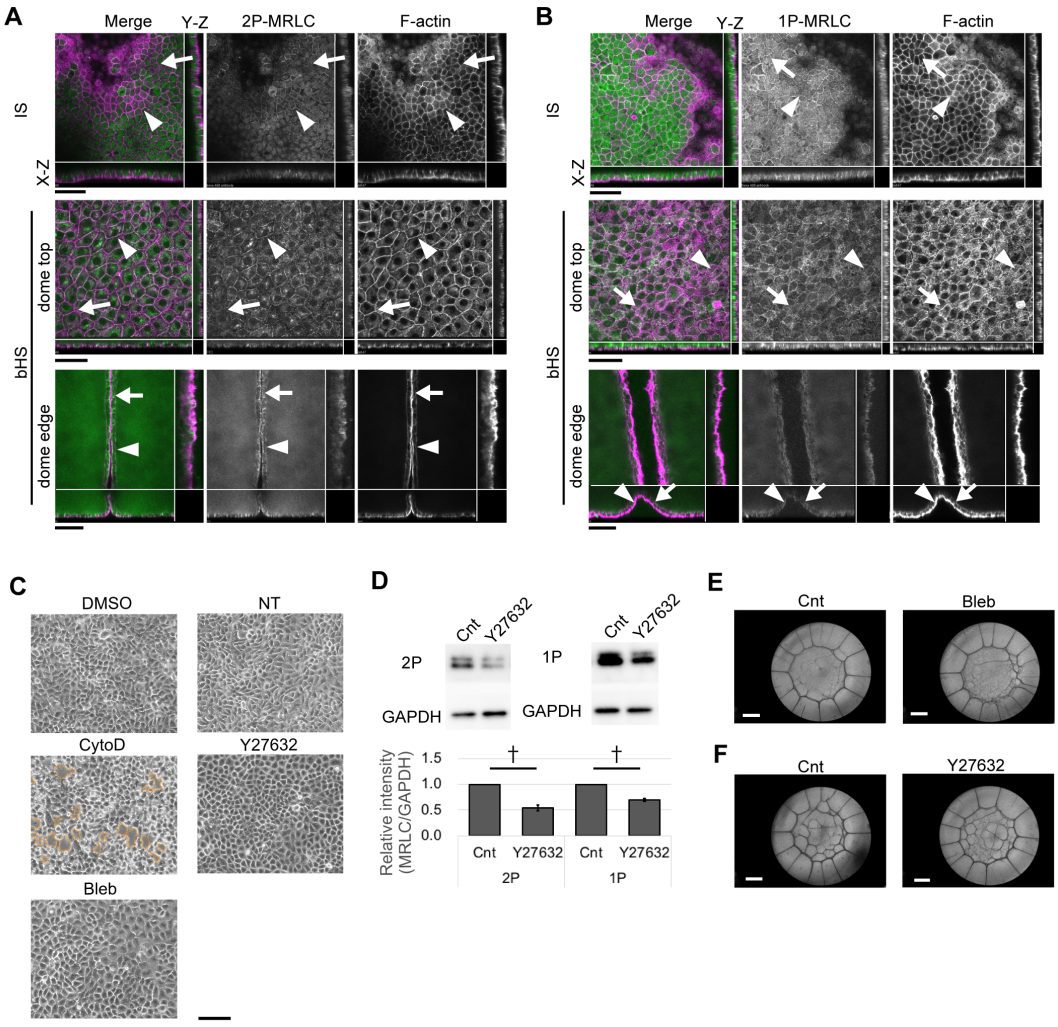

Figure 4.19 The inhibition of myosin did not affect G-dome formation.

(**A-B**) Fluorescent images of 2P-MRLC (A) and 1P-MRLC (B) of MDCK monolayer in IS and in bHS. The samples were inverted onto a cover glass. Arrowheads and arrows indicate colocalization and non-colocalization of P-MRLC and F-actin, respectively. Green, F-actin. Magenta, P-MRLCs. Scale bars, 50 μm. Images are from *n* = at least 1 experiment. (**C**) Phase-contrast images of MDCK sheet after 4 h incubation with actomyosin inhibitors. DMSO is control for cytochalasin D (CytoD) and blebbistatin (Bleb). NT is control for Y27632. Orange dashed lines represents the hole in MDCK monolayer. Scale bar, 100 μm. Images are representatives from *n* = 1 experiment. (**D**) Western blot analysis for 2P-MRLC, 1P-MRLC, and GAPDH in G-dome om 0.63 mM GP-Matrigel with Y27632 treatment. *n* = 2 independent experiments. Mean±S.D. †, significance by 99% confidence interval. (**E, F**) Phase-contrast images of G-domes on 0.63 mM GP-Matrigel after 9 h incubation in bHS with Bleb (E) and Y27632 (F). Scale bars, 1 mm. Images are the representatives.

4-2-10. The Contribution of Cell Proliferation to G-dome Formation

We next evaluated the contribution of cell proliferation because the surface area of MDCK monolayer increased through G-dome formation. In addition to cell stretching, cell proliferation has key roles in the area increase. Cell proliferation inhibitor roscovitine was treated to MDCK cells and it significantly reduced the proliferation after 2 days treatment (Figure 4.20A). After the 2 days pre-treatment, MDCK monolayer on GP-Matrigel was exposed to bHS. The G-dome appeared regardless of roscovitine treatment, not so much as delayed the G-dome formation (Figure 4.20B,C). These data suggest that the increase of surface area may be attributes not to cell proiferation, but to cell stretching.

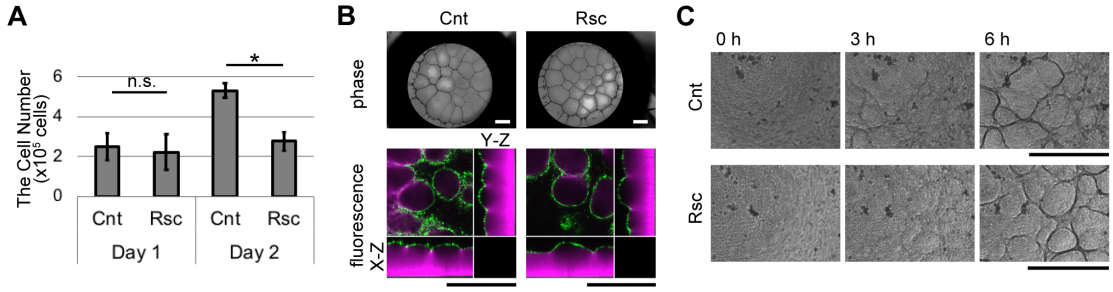

Figure 4.20 The inhibition of cell proliferation did not affect G-dome formation

(**A**) Cell proliferation assay of MDCK cells in presence of roscotivine (Rsc) or DMSO (control; Cnt). n = 3 independent experiments. Mean±S.D. n.s., no significance. *, p<0.05 (Student's t-test). (**B**) Images of G-domes on 0.63 mM GP-Matrigel after overnight incubation in bHS with Rsc and Cnt. Green, MDCK-CAAX. Magenta, GP-Matrigel.

(**C**) Time development of G-dome frmation on 0.63 mM GP-Matrigel with treatment of Rsc or Cnt. Scale bars, 1 mm. Images are the representatives.

4-3. Discussion

To the best of our knowledge, this is the first report that the osmotic gradient induces stable dome morphogenesis *in vitro*. Here, we suggest a model for the stable G-dome morphogenesis (Figure 4.21). In response to bHS, cells started water transport in a cell height-dependent manner. Thin cells transport more water than thick cells, leading to local swelling of the GP-Matrigel and positive feedback of heterogeneous water transport. This results in G-dome formation.

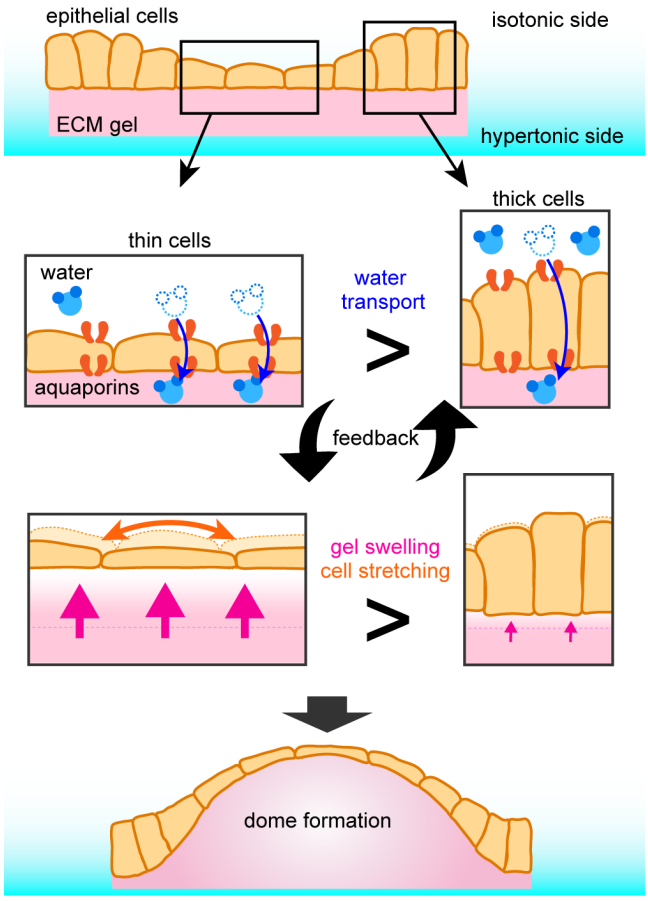

Figure 4.21 The osmotic gradient triggers G-dome formation via the positive feedback of heterogeneous water transport and subsequent gel swelling.

In response to the bHS, MDCK cells on an ECM gel transport water *via* AQPs in cell height-dependent manner. The heterogeneous water transport causes local gel swelling, which induces local cell stretching. The stretching increased the difference in cell height, accelerating a feedback loop of heterogeneous water transport. The feedback leads G-dome formation.

The concentration of GP, which is a cross-linker that increases the viscoelasticity of biomaterials, affected the G-dome appearance in bHS. The mechanical properties of the substrates regulate cell morphogenesis *in vitro*. Increased elasticity inhibits lumen formation by folding cell migration (Ishida et al., 2014). In addition, increased viscosity disrupts the formation of the tulip hat structure of a cell cluster (Imai et al., 2015). The elasticity of gel increased with increase of GP concentration. In addition, the swelling property decreased with increase of GP concentration. Because the increase in elasticity of the gel has a negative effect on gel swelling (Quesada-Perez et al., 2011), GP crosslinking is presumed to prevent Matrigel from swelling by augmenting its elasticity.

With the use of GP-Matrigel, the domes did not collapse but were maintained, probably owing to the difference in ground substances. F-domes are generated by the hydrostatic pressure of the fluid inside of the dome (Latorre et al., 2018). Ethylenediaminetetraacetic acid (EDTA) treatment generates small spaces between the cells and vanishes F-domes (Latorre et al., 2018). Fluid immediately flows out from teh domes through the small disruption. On the other hand, the inside of G-domes was filled with GP-Matrigel, which is gelated (not in the liquid state) and may not leak from the domes following local disruption. Further, the mechanical plasticity of the ECM supports the branching morphogenesis in the mammary gland (Buchmann et al., 2019). G-dome structures were maintained after the removal of the osmotic gradient, indicating that the GP-Matrigel plastically deformed and supported the dome structure.

Cells at the top of the G-domes were stretched. Previous studies have reported volumes of both cytoplasm and nucleus decrease for extended cells (Guo et al., 2017) and that volume changes regulate cell behavior. In our study, the nuclear volume in stretched MDCK cells did not decrease, rather increased. The increase in the cell volume causes the decrease in the macromolecular concentration inside the cells, leading cell cycle arrest (Neurohr et al., 2019). We revealed that the cells at the G-dome top were stretched, and their increased volume may arrest cell cycle progression. The inhibition of cell proliferation did not affect G-dome formation. Thus, the increase in the volume of extended cells may not significantly impact on the formation of G-dome.

A certain degree of swelling was necessary for G-dome formation. The contribution of the ECM to morphogenesis has been actively investigated; however, the contribution of ECM swelling to morphogenesis is mostly unknown. Tanaka *et al*.

reported the a folding pattern appears when the swelling occurs only at the surface of hydrogels (Tanaka et al., 1987). Another group mimicked the formation of cortical convolution in the brain with gel swelling (Tallinen et al., 2016). Our findings propose the possibility of the contribution of ECM swelling to *in vivo* morphogenesis.

In conclusion, this study has found that G-dome morphogenesis is affected by osmotic gradient across a cell sheet. The osmotic gradient triggered the swelling of GP-Matrigel *via* AQPs water transport activity in a cell height-dependent manner. In addition, computer simulations demonstrated that water transport with positive feedback between cell stretching and gel swelling plays key roles for G-dome formation. This study raises the possibility that osmotic gradient induces dome morphogenesis *in vivo* by promoting water transport of AQPs.

4-4 Legends for Movies

Movie 4.1 3D live cell imaging of F-domes induced by bHS.

3D live imaging video that F-domes collapsed and rebirthed on permeable membrane. Green, MDCK-CAAX cells. 75 min/frame.

Movie 4.2 3D view of the domes on 0.75 mM GP-Matrigel induced by bHS.

3D view of the domes that appeared on 0.75 mM GP-Matrigel with the incubation in bHS. Green, MDCK-CAAX cells.

Movie 4.3 Phase contrast time-lapse movie of the appearance of G-domes.

Time-lapse video that MDCK sheet generated and kept the dome stuructures on 0.63 mM GP-Matrigel. 75 min/frame.

Movie 4.4 3D live cell imaging of G-domes induced by bHS.

3D live imaging video that G-dome formation on 0.63 mM GP-Matrigel. The video started immediately after the application of bHS. Green, MDCK-CAAX cells. Magenta, GP-Matrigel. 180 min/frame.

Movie 4.5 3D live cell imaging of G-dome formation on GP-Matrigel containing fluorescent beads.

3D live imaging video that G-dome formation on 0.63 mM GP-Matrigel with fluorescent beads. The first half of the video was merge and the second half was beads image that was extracted from the first half. Video started immediately after the bHS treatment. Green, MDCK-CAAX. Magenta, GP-Matrigel. Cyan and white, beads. 180 min/frame.

Chapter 5

Summary and Remaining Questions

This study reported that lumen and dome morphogenesis with the sheet deformation of MDCK cells. Folding lumen formation was induced by gel overlay to MDCK colonies cultured on collagen gel. During the lumen formation, MDCK cells exhibited the folding collective cell migration, showing the periphery of the colonies folded up and migrated inwardly. The inhibition of integrin-β1 and Rac1, which is the key proteins for cell migration, delayed the folding migration. In addition, cells maintained the apical basal polarity through the lumen formation, and the polarity disruption resulted in random cell migration and defects of lumen formation. These indicate that cell migration and polarity maintenance is crucial for lumen formation of the folding after gel overlay.

However, why cells migrate inwardly, not outwardly, remained as an unsolved question. Gel sandwich assay generate the space around MDCK colonies, but cells did not spread out but still migrated inwardly. This suggests that folding migration is not the migration on the surface of overlaid collagen layer, but specific factor regulates the direction of migration. Further studies are required to reveal the key factor to regulate the direction of the migration.

The stable dome morphogenesis was induced to MDCK sheet by both bHS and the Matrigel with the treatment of specific GP concentration. During the G-dome formation, the GP-Matrigel swelled via cellular AQP water transport, and the water transport was increased as cells were extended by gel swelling. These indicated that stable dome morphogenesis on ECM is affected by osmotic gradient and subsequent water transport of cells.

However, how the dome diameter is determined is unclear. This study revealed that heterogeneous of cell height caused the biased water transport, and the biased water transport caused dome formation. In addition, observation of partial area supported that initial cell height correlated to future position on domes. Meanwhile, the correlation between initial heterogeneity and dome diameter are unknown. To investigate this, cell height is needed to be tracked in the whole process of G-dome formation with large area. However, it is technically difficult to track both the cell shape in G-dome formation because it is beyond the performance limitation of our confocal microscopy. The G-domes were large and beyond the depth of the field of our high power objective lens. Therefore, we performed 3D live imaging using a low power objective lens. However, the cell height was beyond recognition. Because cell density

was related to cell height, we tried to track the cell density with MDCK cells with fluorescent-labeled nucleus (MDCK-H2B cells). However, MDCK-H2B cells did not show G-dome formation, which may be because the transfection modulates the cell characters. Thus, another approach is required. The 3D live imaging of nucleus in the whole process of G-dome formation may promote the understanding of the mechanisms of G-dome formation.

Reference

Aukhil, I. (2000). Biology of wound healing. *Periodontol 2000* **22**, 44-50.

Baetz, N. W., Hoffman, E. A., Yool, A. J. and Stamer, W. D. (2009). Role of aquaporin-1 in trabecular meshwork cell homeostasis during mechanical strain. *Exp Eye Res* **89**, 95-100.

Bai, L., Fushimi, K., Sasaki, S. and Marumo, F. (1996). Structure of aquaporin-2 vasopressin water channel. *J Biol Chem* **271**, 5171-6.

Bao, M., Xie, J., Piruska, A. and Huck, W. T. S. (2017). 3D microniches reveal the importance of cell size and shape. *Nat Commun* **8**, 1962.

Barnes, J. M., Przybyla, L. and Weaver, V. M. (2017). Tissue mechanics regulate brain development, homeostasis and disease. *J Cell Sci* **130**, 71-82.

Bonnans, C., Chou, J. and Werb, Z. (2014). Remodelling the extracellular matrix in development and disease. *Nat Rev Mol Cell Biol* **15**, 786-801.

Borgnia, M., Nielsen, S., Engel, A. and Agre, P. (1999). Cellular and molecular biology of the aquaporin water channels. *Annu Rev Biochem* **68**, 425-58.

Boyd, J. D., Hamilton, W. J. and Boyd, C. A. (1968). The surface of the syncytium of the human chorionic villus. *J Anat* **102**, 553-63.

Buchmann, B., Meixner, L. K., Fernandez, P., Huttere, F. P., Raich, M. K., Scheel, C. H. and Bausch, A. R. (2019). Mechanical plasticity of the ECM directs invasive branching morphogenesis in human mammary gland organoids. *bioRxiv*.

Butcher, D. T., Alliston, T. and Weaver, V. M. (2009). A tense situation: forcing tumour progression. *Nat Rev Cancer* **9**, 108-22.

Camilleri, M., Sellin, J. H. and Barrett, K. E. (2017). Pathophysiology, Evaluation, and Management of Chronic Watery Diarrhea. *Gastroenterology* **152**, 515-532.e2.

Caswell, P. T., Vadrevu, S. and Norman, J. C. (2009). Integrins: masters and slaves of endocytic transport. *Nat Rev Mol Cell Biol* **10**, 843-53.

Chen, D. Y., Crest, J., Streichan, S. J. and Bilder, D. (2019). Extracellular matrix stiffness cues junctional remodeling for 3D tissue elongation. *Nat Commun* **10**, 3339.

Chen, H., Ouyang, W., Lawuyi, B., Martoni, C. and Prakash, S. (2005). Reaction of chitosan with genipin and its fluorogenic attributes for potential microcapsule membrane characterization. *J Biomed Mater Res A* **75**, 917-27.

Chen, J. and Zhang, M. (2013). The Par3/Par6/aPKC complex and epithelial cell polarity. *Exp Cell Res* **319**, 1357-64.

Chin, A. M., Hill, D. R., Aurora, M. and Spence, J. R. (2017). Morphogenesis and maturation of the embryonic and postnatal intestine. *Semin Cell Dev Biol* **66**, 81-93.

Cooke, R. (1995). The actomyosin engine. *FASEB J* **9**, 636-42.

Day, R. E., Kitchen, P., Owen, D. S., Bland, C., Marshall, L., Conner, A. C., Bill, R. M. and Conner, M. T. (2014). Human aquaporins: regulators of transcellular water flow. *Biochim Biophys Acta* **1840**, 1492-506.

Deen, P. M., Nielsen, S., Bindels, R. J. and van Os, C. H. (1997). Apical and basolateral expression of aquaporin-1 in transfected MDCK and LLC-PK cells and functional evaluation of their transcellular osmotic water permeabilities. *Pflugers Arch* **433**, 780-7.

Diaz-de-la-Loza, M. D., Ray, R. P., Ganguly, P. S., Alt, S., Davis, J. R., Hoppe, A., Tapon, N., Salbreux, G. and Thompson, B. J. (2018). Apical and Basal Matrix Remodeling Control Epithelial Morphogenesis. *Dev Cell* **46**, 23-39.e5.

Dukes, J. D., Whitley, P. and Chalmers, A. D. (2011). The MDCK variety pack: choosing the right strain. *BMC Cell Biol* **12**, 43.

Dupont, S., Morsut, L., Aragona, M., Enzo, E., Giulitti, S., Cordenonsi, M., Zanconato, F., Le Digabel, J., Forcato, M., Bicciato, S. et al. (2011). Role of YAP/TAZ in mechanotransduction. *Nature* **474**, 179-83.

Eiraku, M., Takata, N., Ishibashi, H., Kawada, M., Sakakura, E., Okuda, S., Sekiguchi, K., Adachi, T. and Sasai, Y. (2011). Self-organizing optic-cup morphogenesis in three-dimensional culture. *Nature* **472**, 51-6.

Eisen, R., Walid, S., Ratcliffe, D. R. and Ojakian, G. K. (2006). Regulation of epithelial tubule formation by Rho family GTPases. *Am J Physiol Cell Physiol* **290**, C1297-309.

Engler, A. J., Sen, S., Sweeney, H. L. and Discher, D. E. (2006). Matrix elasticity directs stem cell lineage specification. *Cell* **126**, 677-89.

Friedl, P. and Gilmour, D. (2009). Collective cell migration in morphogenesis, regeneration and cancer. *Nat Rev Mol Cell Biol* **10**, 445-57.

Gao, L., Gan, H., Meng, Z., Gu, R., Wu, Z., Zhang, L., Zhu, X., Sun, W., Li, J., Zheng, Y. et al. (2014). Effects of genipin cross-linking of chitosan hydrogels on

cellular adhesion and viability. *Colloids Surf B Biointerfaces* **117**, 398-405.

Gaush, C. R., Hard, W. L. and Smith, T. F. (1966). Characterization of an established line of canine kidney cells (MDCK). *Proc Soc Exp Biol Med* **122**, 931-5.

Gilmour, D., Rembold, M. and Leptin, M. (2017). From morphogen to morphogenesis and back. *Nature* **541**, 311-320.

Greene, N. D. and Copp, A. J. (2014). Neural tube defects. *Annu Rev Neurosci* **37**, 221-42.

Guo, M., Pegoraro, A. F., Mao, A., Zhou, E. H., Arany, P. R., Han, Y., Burnette, D. T., Jensen, M. H., Kasza, K. E., Moore, J. R. et al. (2017). Cell volume change through water efflux impacts cell stiffness and stem cell fate. *Proc Natl Acad Sci U S A* **114**, E8618-E8627.

Haga, H., Irahara, C., Kobayashi, R., Nakagaki, T. and Kawabata, K. (2005). Collective movement of epithelial cells on a collagen gel substrate. *Biophys J* **88**, 2250-6.

Hall, D. E., Reichardt, L. F., Crowley, E., Holley, B., Moezzi, H., Sonnenberg, A. and Damsky, C. H. (1990). The alpha 1/beta 1 and alpha 6/beta 1 integrin heterodimers mediate cell attachment to distinct sites on laminin. *J Cell Biol* **110**, 2175-84.

Hall, H. G., Farson, D. A. and Bissell, M. J. (1982). Lumen formation by epithelial cell lines in response to collagen overlay: a morphogenetic model in culture. *Proc Natl Acad Sci U S A* **79**, 4672-6.

Hashimoto, W., Sudo, R., Fukasawa, K., Ikeda, M., Mitaka, T. and Tanishita, K. (2008). Ductular network formation by rat biliary epithelial cells in the dynamical culture with collagen gel and dimethylsulfoxide stimulation. *Am J Pathol* **173**, 494-506.

Hayashi, K., Yamamoto, T. S. and Ueno, N. (2018). Intracellular calcium signal at the leading edge regulates mesodermal sheet migration during Xenopus gastrulation. *Sci Rep* **8**, 2433.

Hegerfeldt, Y., Tusch, M., Bröcker, E. B. and Friedl, P. (2002). Collective cell movement in primary melanoma explants: plasticity of cell-cell interaction, beta1-integrin function, and migration strategies. *Cancer Res* **62**, 2125-30.

Heisenberg, C. P. and Bellaïche, Y. (2013). Forces in tissue morphogenesis and patterning. *Cell* **153**, 948-62.

Hellman, N. E., Spector, J., Robinson, J., Zuo, X., Saunier, S., Antignac, C., Tobias, J. W. and Lipschutz, J. H. (2008). Matrix metalloproteinase 13 (MMP13) and tissue inhibitor of matrix metalloproteinase 1 (TIMP1), regulated by the MAPK pathway, are both necessary for Madin-Darby canine kidney tubulogenesis. *J Biol Chem* **283**, 4272-82.

Hendzel, M. J., Wei, Y., Mancini, M. A., Van Hooser, A., Ranalli, T., Brinkley, B. R., Bazett-Jones, D. P. and Allis, C. D. (1997). Mitosis-specific phosphorylation of histone H3 initiates primarily within pericentromeric heterochromatin during G2 and spreads in an ordered fashion coincident with mitotic chromosome condensation. *Chromosoma* **106**, 348-60.

Hirano, Y., Okimoto, N., Kadohira, I., Suematsu, M., Yasuoka, K. and Yasui, M. (2010). Molecular mechanisms of how mercury inhibits water permeation through aquaporin-1: understanding by molecular dynamics simulation. *Biophys J* **98**, 1512-9.

Hirata, E., Ichikawa, T., Horike, S. I. and Kiyokawa, E. (2018). Active K-RAS induces the coherent rotation of epithelial cells: A model for collective cell invasion in vitro. *Cancer Sci* **109**, 4045-4055.

Hollway, G. E., Bryson-Richardson, R. J., Berger, S., Cole, N. J., Hall, T. E. and Currie, P. D. (2007). Whole-somite rotation generates muscle progenitor cell compartments in the developing zebrafish embryo. *Dev Cell* **12**, 207-19.

Horsefield, R., Nordén, K., Fellert, M., Backmark, A., Törnroth-Horsefield, S., Terwisscha van Scheltinga, A. C., Kvassman, J., Kjellbom, P., Johanson, U. and Neutze, R. (2008). High-resolution x-ray structure of human aquaporin 5. *Proc Natl Acad Sci U S A* **105**, 13327-32.

Hoshino, K. I., Nakajima, T., Matsuda, T., Sakai, T. and Gong, J. P. (2018). Network elasticity of a model hydrogel as a function of swelling ratio: from shrinking to extreme swelling states. *Soft Matter* **14**, 9693-9701.

Hull, R. N., Cherry, W. R. and Weaver, G. W. (1976). The origin and characteristics of a pig kidney cell strain, LLC-PK. *In Vitro* **12**, 670-7.

Humphries, J. D., Byron, A. and Humphries, M. J. (2006). Integrin ligands at a glance. *J Cell Sci* **119**, 3901-3.

Hwang, Y. J., Larsen, J., Krasieva, T. B. and Lyubovitsky, J. G. (2011). Effect of genipin crosslinking on the optical spectral properties and structures of

collagen hydrogels. *ACS Appl Mater Interfaces* **3**, 2579-84.

Hynes, R. O. (2002). Integrins: bidirectional, allosteric signaling machines. *Cell* **110**, 673-87.

Ichigi, J. and Asashima, M. (2001). Dome formation and tubule morphogenesis by Xenopus kidney A6 cell cultures exposed to microgravity simulated with a 3D-clinostat and to hypergravity. *In Vitro Cell Dev Biol Anim* **37**, 31-44.

Ikuzawa, M., Akiduki, S. and Asashima, M. (2007). Gene expression profile of X*enopus* A6 cells cultured under random positioning machine shows downregulation of ion transporter genes and inhibition of dome formation. *Advances in Space Research* **40**, 1694-1702.

Ilina, O. and Friedl, P. (2009). Mechanisms of collective cell migration at a glance. *J Cell Sci* **122**, 3203-8.

Imai, M., Furusawa, K., Mizutani, T., Kawabata, K. and Haga, H. (2015). Three-dimensional morphogenesis of MDCK cells induced by cellular contractile forces on a viscous substrate. *Sci Rep* **5**, 14208.

Inoue, Y., Suzuki, M., Watanabe, T., Yasue, N., Tateo, I., Adachi, T. and Ueno, N. (2016). Mechanical roles of apical constriction, cell elongation, and cell migration during neural tube formation in Xenopus. *Biomech Model Mechanobiol* **15**, 1733-1746.

Ishibashi, K., Sasaki, S., Fushimi, K., Uchida, S., Kuwahara, M., Saito, H., Furukawa, T., Nakajima, K., Yamaguchi, Y. and Gojobori, T. (1994). Molecular cloning and expression of a member of the aquaporin family with permeability to glycerol and urea in addition to water expressed at the basolateral membrane of kidney collecting duct cells. *Proc Natl Acad Sci U S A* **91**, 6269-73.

Ishida, S., Tanaka, R., Yamaguchi, N., Ogata, G., Mizutani, T., Kawabata, K. and Haga, H. (2014). Epithelial sheet folding induces lumen formation by Madin-Darby canine kidney cells in a collagen gel. *PLoS One* **9**, e99655.

Ishihara, S., Mizutani, T., Kawabata, K. and Haga, H. (2016). An improved method for western blotting when extracting proteins from mammalian cells cultured on a collagen gel under serum-free conditions. *Cytotechnology* **68**, 25-32.

Ishihara, S., Yasuda, M., Harada, I., Mizutani, T., Kawabata, K. and Haga, H. (2013). Substrate stiffness regulates temporary NF-κB activation via actomyosin contractions. *Exp Cell Res* **319**, 2916-27.

Ivanov, A. I., Parkos, C. A. and Nusrat, A. (2010). Cytoskeletal regulation of epithelial barrier function during inflammation. *Am J Pathol* **177**, 512-24.

Jacinto, A., Martinez-Arias, A. and Martin, P. (2001). Mechanisms of epithelial fusion and repair. *Nat Cell Biol* **3**, E117-23.

Jovov, B., Wills, N. K. and Lewis, S. A. (1991). A spectroscopic method for assessing confluence of epithelial cell cultures. *Am J Physiol* **261**, C1196-203.

Jung, J. S., Bhat, R. V., Preston, G. M., Guggino, W. B., Baraban, J. M. and Agre, P. (1994). Molecular characterization of an aquaporin cDNA from brain: candidate osmoreceptor and regulator of water balance. *Proc Natl Acad Sci U S A* **91**, 13052-6.

Kadono, Y., Shibahara, K., Namiki, M., Watanabe, Y., Seiki, M. and Sato, H. (1998). Membrane type 1-matrix metalloproteinase is involved in the formation of hepatocyte growth factor/scatter factor-induced branching tubules in madin-darby canine kidney epithelial cells. *Biochem Biophys Res Commun* **251**, 681-7.

Kasza, K. E. and Zallen, J. A. (2011). Dynamics and regulation of contractile actin-myosin networks in morphogenesis. *Curr Opin Cell Biol* **23**, 30-8.

Kato, T., Enomoto, A., Watanabe, T., Haga, H., Ishida, S., Kondo, Y., Furukawa, K., Urano, T., Mii, S., Weng, L. et al. (2014). TRIM27/MRTF-B-dependent integrin β1 expression defines leading cells in cancer cell collectives. *Cell Rep* **7**, 1156-67.

Kechagia, J. Z., Ivaska, J. and Roca-Cusachs, P. (2019). Integrins as biomechanical sensors of the microenvironment. *Nat Rev Mol Cell Biol* **20**, 457-473.

Keller, R. (2012). Developmental biology. Physical biology returns to morphogenesis. *Science* **338**, 201-3.

Khan, L. A., Zhang, H., Abraham, N., Sun, L., Fleming, J. T., Buechner, M., Hall, D. H. and Gobel, V. (2013). Intracellular lumen extension requires ERM-1-dependent apical membrane expansion and AQP-8-mediated flux. *Nat Cell Biol* **15**, 143-56.

Kivelä-Rajamäki, M., Maisi, P., Srinivas, R., Tervahartiala, T., Teronen, O., Husa, V., Salo, T. and Sorsa, T. (2003). Levels and molecular forms of MMP-7 (matrilysin-1) and MMP-8 (collagenase-2) in diseased human peri-implant sulcular fluid. *J Periodontal Res* **38**, 583-90.

Kolotuev, I., Hyenne, V., Schwab, Y., Rodriguez, D. and Labouesse, M.

(2013). A pathway for unicellular tube extension depending on the lymphatic vessel determinant Prox1 and on osmoregulation. *Nat Cell Biol* **15**, 157-68.

Kumagai, Y., Nio-Kobayashi, J., Ishida-Ishihara, S., Tachibana, H., Omori, R., Enomoto, A., Ishihara, S. and Haga, H. (2019). The intercellular expression of type-XVII collagen, laminin-332, and integrin-β1 promote contact following during the collective invasion of a cancer cell population. *Biochem Biophys Res Commun* **514**, 1115-1121.

Kuwahara, M., Gu, Y., Ishibashi, K., Marumo, F. and Sasaki, S. (1997). Mercury-sensitive residues and pore site in AQP3 water channel. *Biochemistry* **36**, 13973-8.

Latorre, E., Kale, S., Casares, L., Gómez-González, M., Uroz, M., Valon, L., Nair, R. V., Garreta, E., Montserrat, N., Del Campo, A. et al. (2018). Active superelasticity in three-dimensional epithelia of controlled shape. *Nature* **563**, 203-208.

Lee, S.-W., Lim, J.-M., Bhoo, S.-H., Paik, Y.-S. and Hahn, T.-R. (2003). Colorimetric determination of amino acids using gene-in from Gardenia jasminoides. *Analytica Chimica Acta* **480**, 267-274.

Leighton, J., Brada, Z., Estes, L. W. and Justh, G. (1969). Secretory activity and oncogenicity of a cell line (MDCK) derived from canine kidney. *Science* **163**, 472-3.

Leighton, J., Estes, L. W., Mansukhani, S. and Brada, Z. (1970). A cell line derived from normal dog kidney (MDCK) exhibiting qualities of papillary adenocarcinoma and of renal tubular epithelium. *Cancer* **26**, 1022-8.

Liu, K., Kozono, D., Kato, Y., Agre, P., Hazama, A. and Yasui, M. (2005). Conversion of aquaporin 6 from an anion channel to a water-selective channel by a single amino acid substitution. *Proc Natl Acad Sci U S A* **102**, 2192-7.

Liu, X., Wu, H., Byrne, M., Krane, S. and Jaenisch, R. (1997). Type III collagen is crucial for collagen I fibrillogenesis and for normal cardiovascular development. *Proc Natl Acad Sci U S A* **94**, 1852-6.

Madrid, R., Le Maout, S., Barrault, M. B., Janvier, K., Benichou, S. and Mérot, J. (2001). Polarized trafficking and surface expression of the AQP4 water channel are coordinated by serial and regulated interactions with different clathrin-adaptor complexes. *EMBO J* **20**, 7008-21.

Markert, C. D., Guo, X., Skardal, A., Wang, Z., Bharadwaj, S., Zhang, Y.,

Bonin, K. and Guthold, M. (2013). Characterizing the micro-scale elastic modulus of hydrogels for use in regenerative medicine. *J Mech Behav Biomed Mater* **27**, 115-27.

Marsden, M. and DeSimone, D. W. (2001). Regulation of cell polarity, radial intercalation and epiboly in Xenopus: novel roles for integrin and fibronectin. *Development* **128**, 3635-47.

Marsden, M. and DeSimone, D. W. (2003). Integrin-ECM interactions regulate cadherin-dependent cell adhesion and are required for convergent extension in Xenopus. *Curr Biol* **13**, 1182-91.

Martin, A. C. (2010). Pulsation and stabilization: contractile forces that underlie morphogenesis. *Dev Biol* **341**, 114-25.

Martin, A. C. and Goldstein, B. (2014). Apical constriction: themes and variations on a cellular mechanism driving morphogenesis. *Development* **141**, 1987-98.

Martin-Belmonte, F. and Mostov, K. (2008). Regulation of cell polarity during epithelial morphogenesis. *Curr Opin Cell Biol* **20**, 227-34.

Matsuda, K., Gotoh, H., Tajika, Y., Sushida, T., Aonuma, H., Niimi, T., Akiyama, M., Inoue, Y. and Kondo, S. (2017). Complex furrows in a 2D epithelial sheet code the 3D structure of a beetle horn. *Sci Rep* **7**, 13939.

Matsuzaki, T., Suzuki, T. and Takata, K. (2001). Hypertonicity-induced expression of aquaporin 3 in MDCK cells. *Am J Physiol Cell Physiol* **281**, C55-63.

Mi, F.-L., Sung, H.-W. and Shy, S.-S. (2000). Synthesis and characterization of a novel chitosan-basad network prepared using naturally occurring crosslinker. *Phlymer Chemistry* **38**, 2804-2814.

Migeotte, I., Omelchenko, T., Hall, A. and Anderson, K. V. (2010). Rac1-dependent collective cell migration is required for specification of the anterior-posterior body axis of the mouse. *PLoS Biol* **8**, e1000442.

Miroshnikova, Y. A., Jorgens, D. M., Spirio, L., Auer, M., Sarang-Sieminski, A. L. and Weaver, V. M. (2011). Engineering strategies to recapitulate epithelial morphogenesis within synthetic three-dimensional extracellular matrix with tunable mechanical properties. *Phys Biol* **8**, 026013.

Mizutani, T., Haga, H., Kato, K., Matsuda, K. and Kawabata, K. (2006a). Observation of Stiff Domain Structure on Collagen Gels by Wide-Range Scanning Probe Microscopy. *Japanese Journal of Applied Physics* **45**, 3.

Mizutani, T., Haga, H., Koyama, Y., Takahashi, M. and Kawabata, K.

(2006b). Diphosphorylation of the myosin regulatory light chain enhances the tension acting on stress fibers in fibroblasts. *J Cell Physiol* **209**, 726-31.

Mizutani, T., Kawabata, K., Koyama, Y., Takahashi, M. and Haga, H. (2009). Regulation of cellular contractile force in response to mechanical stretch by diphosphorylation of myosin regulatory light chain via RhoA signaling cascade. *Cell Motil Cytoskeleton* **66**, 389-97.

Morita, H., Kajiura-Kobayashi, H., Takagi, C., Yamamoto, T. S., Nonaka, S. and Ueno, N. (2012). Cell movements of the deep layer of non-neural ectoderm underlie complete neural tube closure in Xenopus. *Development* **139**, 1417-26.

Mulders, S. M., Rijss, J. P., Hartog, A., Bindels, R. J., van Os, C. H. and Deen, P. M. (1997). Importance of the mercury-sensitive cysteine on function and routing of AQP1 and AQP2 in oocytes. *Am J Physiol* **273**, F451-6.

Murata-Hori, M., Suizu, F., Iwasaki, T., Kikuchi, A. and Hosoya, H. (1999). ZIP kinase identified as a novel myosin regulatory light chain kinase in HeLa cells. *FEBS Lett* **451**, 81-4.

Murrell, M., Kamm, R. and Matsudaira, P. (2011). Substrate viscosity enhances correlation in epithelial sheet movement. *Biophys J* **101**, 297-306.

Muzzarelli, R. A., El Mehtedi, M., Bottegoni, C., Aquili, A. and Gigante, A. (2015). Genipin-Crosslinked Chitosan Gels and Scaffolds for Tissue Engineering and Regeneration of Cartilage and Bone. *Mar Drugs* **13**, 7314-38.

Nakayama, M., Amano, M., Katsumi, A., Kaneko, T., Kawabata, S., Takefuji, M. and Kaibuchi, K. (2005). Rho-kinase and myosin II activities are required for cell type and environment specific migration. *Genes Cells* **10**, 107-17.

Neurohr, G. E., Terry, R. L., Lengefeld, J., Bonney, M., Brittingham, G. P., Moretto, F., Miettinen, T. P., Vaites, L. P., Soares, L. M., Paulo, J. A. et al. (2019). Excessive Cell Growth Causes Cytoplasm Dilution And Contributes to Senescence. *Cell* **176**, 1083-1097.e18.

Nikolopoulou, E., Galea, G. L., Rolo, A., Greene, N. D. and Copp, A. J. (2017). Neural tube closure: cellular, molecular and biomechanical mechanisms. *Development* **144**, 552-566.

Nogawa, H. and Hasegawa, Y. (2002). Sucrose stimulates branching morphogenesis of embryonic mouse lung in vitro: a problem of osmotic balance between lumen fluid and culture medium. *Dev Growth Differ* **44**, 383-90.

Noitem, R., Yuajit, C., Soodvilai, S., Muanprasat, C. and Chatsudthipong, V. (2018). Steviol slows renal cyst growth by reducing AQP2 expression and promoting AQP2 degradation. *Biomed Pharmacother* **101**, 754-762.

Nukuda, A., Sasaki, C., Ishihara, S., Mizutani, T., Nakamura, K., Ayabe, T., Kawabata, K. and Haga, H. (2015). Stiff substrates increase YAP-signaling-mediated matrix metalloproteinase-7 expression. *Oncogenesis* **4**, e165.

O'Brien, L. E., Zegers, M. M. and Mostov, K. E. (2002). Opinion: Building epithelial architecture: insights from three-dimensional culture models. *Nat Rev Mol Cell Biol* **3**, 531-7.

Ojakian, G. K. and Schwimmer, R. (1988). The polarized distribution of an apical cell surface glycoprotein is maintained by interactions with the cytoskeleton of Madin-Darby canine kidney cells. *J Cell Biol* **107**, 2377-87.

Okuda, S., Inoue, Y. and Adachi, T. (2015). Three-dimensional vertex model for simulating multicellular morphogenesis. *Biophys Physicobiol* **12**, 13-20.

Omelchenko, T., Vasiliev, J. M., Gelfand, I. M., Feder, H. H. and Bonder, E. M. (2003). Rho-dependent formation of epithelial "leader" cells during wound healing. *Proc Natl Acad Sci U S A* **100**, 10788-93.

Paszek, M. J., Zahir, N., Johnson, K. R., Lakins, J. N., Rozenberg, G. I., Gefen, A., Reinhart-King, C. A., Margulies, S. S., Dembo, M., Boettiger, D. et al. (2005). Tensional homeostasis and the malignant phenotype. *Cancer Cell* **8**, 241-54.

Preston, G. M., Jung, J. S., Guggino, W. B. and Agre, P. (1993). The mercury-sensitive residue at cysteine 189 in the CHIP28 water channel. *J Biol Chem* **268**, 17-20.

Quesada-Perez, M., Maroto-Centeno, J. A., Forcada, J. and Hidalgo-Alvarez, R. (2011). Gel swelling theories: the classical formalism and recent aqqroaches. *Soft Matter*, 11.

Rabito, C. A., Tchao, R., Valentich, J. and Leighton, J. (1980). Effect of cell-substratum interaction on hemicyst formation by MDCK cells. *In Vitro* **16**, 461-8.

Raven, P. H., Johnson, G. B., Losos, J. B. and Singer, S. R. (2006). Biology.

Reffay, M., Parrini, M. C., Cochet-Escartin, O., Ladoux, B., Buguin, A., Coscoy, S., Amblard, F., Camonis, J. and Silberzan, P. (2014). Interplay of RhoA and mechanical forces in collective cell migration driven by leader cells. *Nat Cell Biol* **16**,

217-23.

Ridley, A. J. (2001). Rho GTPases and cell migration. *J Cell Sci* **114**, 2713-22.

Ridley, A. J. (2015). Rho GTPase signalling in cell migration. *Curr Opin Cell Biol* **36**, 103-12.

Ridley, A. J., Schwartz, M. A., Burridge, K., Firtel, R. A., Ginsberg, M. H., Borisy, G., Parsons, J. T. and Horwitz, A. R. (2003). Cell migration: integrating signals from front to back. *Science* **302**, 1704-9.

Rozario, T. and DeSimone, D. W. (2010). The extracellular matrix in development and morphogenesis: a dynamic view. *Dev Biol* **341**, 126-40.

Scarpa, E. and Mayor, R. (2016). Collective cell migration in development. *J Cell Biol* **212**, 143-55.

Schnermann, J., Chou, C. L., Ma, T., Traynor, T., Knepper, M. A. and Verkman, A. S. (1998). Defective proximal tubular fluid reabsorption in transgenic aquaporin-1 null mice. *Proc Natl Acad Sci U S A* **95**, 9660-4.

Schwimmer, R. and Ojakian, G. K. (1995). The alpha 2 beta 1 integrin regulates collagen-mediated MDCK epithelial membrane remodeling and tubule formation. *J Cell Sci* **108 (Pt 6)**, 2487-98.

Shyer, A. E., Rodrigues, A. R., Schroeder, G. G., Kassianidou, E., Kumar, S. and Harland, R. M. (2017). Emergent cellular self-organization and mechanosensation initiate follicle pattern in the avian skin. *Science* **357**, 811-815.

Shyer, A. E., Tallinen, T., Nerurkar, N. L., Wei, Z., Gil, E. S., Kaplan, D. L., Tabin, C. J. and Mahadevan, L. (2013). Villification: how the gut gets its villi. *Science* **342**, 212-8.

Sigurbjörnsdóttir, S., Mathew, R. and Leptin, M. (2014). Molecular mechanisms of de novo lumen formation. *Nat Rev Mol Cell Biol* **15**, 665-76.

Simmons, N. L. (1982). Cultured monolayers of MDCK cells: a novel model system for the study of epithelial development and function. *Gen Pharmacol* **13**, 287-91.

Solnica-Krezel, L. (2005). Conserved patterns of cell movements during vertebrate gastrulation. *Curr Biol* **15**, R213-28.

Somlyo, A. P. and Somlyo, A. V. (2003). Ca2+ sensitivity of smooth muscle and nonmuscle myosin II: modulated by G proteins, kinases, and myosin phosphatase.

Physiol Rev **83**, 1325-58.

Soofi, S. S., Last, J. A., Liliensiek, S. J., Nealey, P. F. and Murphy, C. J. (2009). The elastic modulus of Matrigel as determined by atomic force microscopy. *J Struct Biol* **167**, 216-9.

Sumigray, K. D., Terwilliger, M. and Lechler, T. (2018). Morphogenesis and Compartmentalization of the Intestinal Crypt. *Dev Cell* **45**, 183-197.e5.

Sundararaghavan, H. G., Monteiro, G. A., Lapin, N. A., Chabal, Y. J., Miksan, J. R. and Shreiber, D. I. (2008). Genipin-induced changes in collagen gels: correlation of mechanical properties to fluorescence. *J Biomed Mater Res A* **87**, 308-20.

Sung, H. W., Chang, W. H., Ma, C. Y. and Lee, M. H. (2003). Crosslinking of biological tissues using genipin and/or carbodiimide. *J Biomed Mater Res A* **64**, 427-38.

Sung, H. W., Huang, R. N., Huang, L. L., Tsai, C. C. and Chiu, C. T. (1998). Feasibility study of a natural crosslinking reagent for biological tissue fixation. *J Biomed Mater Res* **42**, 560-7.

Takami, M. and Suzuki, Y. (1994). Hydrophobic blue pigment formation from phosphatidylgenipin. *J Nutr Sci Vitaminol (Tokyo)* **40**, 505-9.

Takemoto, K., Ishihara, S., Mizutani, T., Kawabata, K. and Haga, H. (2015). Compressive stress induces dephosphorylation of the myosin regulatory light chain via RhoA phosphorylation by the adenylyl cyclase/protein kinase A signaling pathway. *PLoS One* **10**, e0117937.

Tallinen, T., Chung, J. Y., Rousseau, F., Girard, N., Lefevre, J. and Mahadevan, L. (2016). On the growth and form of cortical convolutions. *Nature Physics* **12**, 588-593.

Tanaka, T., Sun, S.-T., Hirokawa, Y., Katayama, S., Kucera, J., Hirose, Y. and Amiya, T. (1987). Mechanical instability of gels at the phase transition. *Nature* **325**, 796-798.

Tonoli, H., Flachon, V., Audebet, C., Callé, A., Jarry-Guichard, T., Statuto, M., Rousset, B. and Munari-Silem, Y. (2000). Formation of three-dimensional thyroid follicle-like structures by polarized FRT cells made communication competent by transfection and stable expression of the connexin-32 gene. *Endocrinology* **141**, 1403-13.

Totsukawa, G., Wu, Y., Sasaki, Y., Hartshorne, D. J., Yamakita, Y.,

Yamashiro, S. and Matsumura, F. (2004). Distinct roles of MLCK and ROCK in the regulation of membrane protrusions and focal adhesion dynamics during cell migration of fibroblasts. *J Cell Biol* **164**, 427-39.

Tsai, C. C., Huang, R. N., Sung, H. W. and Liang, H. C. (2000). In vitro evaluation of the genotoxicity of a naturally occurring crosslinking agent (genipin) for biologic tissue fixation. *J Biomed Mater Res* **52**, 58-65.

Ueda, K., Murata-Hori, M., Tatsuka, M. and Hosoya, H. (2002). Rho-kinase contributes to diphosphorylation of myosin II regulatory light chain in nonmuscle cells. *Oncogene* **21**, 5852-60.

Ushiki, T. (2013). 入門組織学　改訂第２版.

Uyeda, T. Q., Iwadate, Y., Umeki, N., Nagasaki, A. and Yumura, S. (2011). Stretching actin filaments within cells enhances their affinity for the myosin II motor domain. *PLoS One* **6**, e26200.

van Balkom, B. W., van Raak, M., Breton, S., Pastor-Soler, N., Bouley, R., van der Sluijs, P., Brown, D. and Deen, P. M. (2003). Hypertonicity is involved in redirecting the aquaporin-2 water channel into the basolateral, instead of the apical, plasma membrane of renal epithelial cells. *J Biol Chem* **278**, 1101-7.

Van Itallie, C. M., Fanning, A. S., Bridges, A. and Anderson, J. M. (2009). ZO-1 stabilizes the tight junction solute barrier through coupling to the perijunctional cytoskeleton. *Mol Biol Cell* **20**, 3930-40.

Verkman, A. S. (2011). Aquaporins at a glance. *J Cell Sci* **124**, 2107-12.

Vicente-Manzanares, M., Ma, X., Adelstein, R. S. and Horwitz, A. R. (2009). Non-muscle myosin II takes centre stage in cell adhesion and migration. *Nat Rev Mol Cell Biol* **10**, 778-90.

Vogel, W. F., Aszódi, A., Alves, F. and Pawson, T. (2001). Discoidin domain receptor 1 tyrosine kinase has an essential role in mammary gland development. *Mol Cell Biol* **21**, 2906-17.

Walton, K. D., Freddo, A. M., Wang, S. and Gumucio, D. L. (2016a). Generation of intestinal surface: an absorbing tale. *Development* **143**, 2261-72.

Walton, K. D., Whidden, M., Kolterud, Å., Shoffner, S. K., Czerwinski, M. J., Kushwaha, J., Parmar, N., Chandhrasekhar, D., Freddo, A. M., Schnell, S. et al. (2016b). Villification in the mouse: Bmp signals control intestinal villus patterning. *Development* **143**, 427-36.

Wang, W., Li, F., Sun, Y., Lei, L., Zhou, H., Lei, T., Xia, Y., Verkman, A. S. and Yang, B. (2015). Aquaporin-1 retards renal cyst development in polycystic kidney disease by inhibition of Wnt signaling. *FASEB J* **29**, 1551-63.

Wang, X., He, L., Wu, Y. I., Hahn, K. M. and Montell, D. J. (2010). Light-mediated activation reveals a key role for Rac in collective guidance of cell movement in vivo. *Nat Cell Biol* **12**, 591-7.

Wolpert, L. and Tickle, C. (2012). Principles of Development, 4th Edition: Medical Science International.

Xu, J., Lamouille, S. and Derynck, R. (2009). TGF-beta-induced epithelial to mesenchymal transition. *Cell Res* **19**, 156-72.

Yamaguchi, N., Mizutani, T., Kawabata, K. and Haga, H. (2015). Leader cells regulate collective cell migration via Rac activation in the downstream signaling of integrin β1 and PI3K. *Sci Rep* **5**, 7656.

Yoshino, D., Funamoto, K., Sato, K., Kenry, Sato, M. and Lim, C. T. (2020). Hydrostatic pressure promotes endothelial tube formation through aquaporin 1 and Ras-ERK signaling. *Commun Biol* **3**, 152.

Young, P. E., Richman, A. M., Ketchum, A. S. and Kiehart, D. P. (1993). Morphogenesis in Drosophila requires nonmuscle myosin heavy chain function. *Genes Dev* **7**, 29-41.

Yu, W., Datta, A., Leroy, P., O'Brien, L. E., Mak, G., Jou, T. S., Matlin, K. S., Mostov, K. E. and Zegers, M. M. (2005). Beta1-integrin orients epithelial polarity via Rac1 and laminin. *Mol Biol Cell* **16**, 433-45.

Yu, W., Shewan, A. M., Brakeman, P., Eastburn, D. J., Datta, A., Bryant, D. M., Fan, Q. W., Weiss, W. A., Zegers, M. M. and Mostov, K. E. (2008). Involvement of RhoA, ROCK I and myosin II in inverted orientation of epithelial polarity. *EMBO Rep* **9**, 923-9.

Yurchenco, P. D. (2011). Basement membranes: cell scaffoldings and signaling platforms. *Cold Spring Harb Perspect Biol* **3**.

Zahm, J. M., Kaplan, H., Hérard, A. L., Doriot, F., Pierrot, D., Somelette, P. and Puchelle, E. (1997). Cell migration and proliferation during the in vitro wound repair of the respiratory epithelium. *Cell Motil Cytoskeleton* **37**, 33-43.

Zihni, C., Mills, C., Matter, K. and Balda, M. S. (2016). Tight junctions: from simple barriers to multifunctional molecular gates. *Nat Rev Mol Cell Biol* **17**,

564-80.

Zuk, A. and Matlin, K. S. (1996). Apical beta 1 integrin in polarized MDCK cells mediates tubulocyst formation in response to type I collagen overlay. *J Cell Sci* **109 (Pt 7)**, 1875-89.

Acknowledgement

First thanks go to Prof. Hisahi Haga for his guidance and supports of my study, and to Prof. Kazushige Kawabata and Associate Prof. Takeomi Mizutani for accepting me to Laboratory of Cell Dynamics. I would like to appreciate Associate Prof. Kazuya Furusawa and Assistant Prof. Seiichiro Ishihara for the critical suggestion to my study. I am grateful to Prof. Tokiyoshi Ayabe and Associate Prof. Tasuku Nakajima for their critical comments of this dissertation.

Huge thanks go to Associate Prof. Masakazu Akiyama and Mr. Ryosuke Tanaka for the collaborative works in mathematical model, and for Prof. Akiyama's mathematical lecture to me. I would also give thanks to Prof. Atsushi Enomoto for the collaborative research and useful valuable discussion.

I would also like to thank the past/current members of the Laboratory of Cell Dynamics and my classmates of Biological Sciences (Macromolecular Functions). The discussion and get-togethers we had were fun times and encourage me throughout my studies.

To family and friends outside of the laboratory, thank you for encouraging me during hard time. Special thanks to my husband for your warm supports and encouragements. I also give thanks to the huge supports from my mother throughout my doctoral course, the helps of my father to proceed to doctorial course and the warm supports from my parents-in-law. I give thanks from my heart to Helmers for accepting me to study English. The experience with Helmers have always helped and taught me.

Finally, I greatly appreciate my Protector, the Lord Jesus Christ for His never-ending encouragements and supports.

Appendix

Appendix 1. Establishment of MDCK-CAAX cell line performed by Mr. N. Yamaguchi

The cell membrane of MDCK cells was labeled with Azami-green (AG) fluorescent proteins (Karasawa et al., 2003). A phmAG1-MCLinker vector (Takara Bio Inc.) carrying the membrane trafficking domain of human H-Ras (Hancock et al., 1991) (phmAG1-H-Ras-CAAX) was constructed. The H-Ras CAAX motif was designed with the EcoRI and BamHI site by using the following primer set: 5'-GATCCGGCTGCATGAGCTGCAAGTGTGTGCTCTCCTGAG-3' (forward) and 5'-AATTCTCAGGAGAGCACACACTTGCAGCTCATGCAGCCG-3' (reverse). MDCK cells were transfected with the plasmid using Lipofectamine 2000 (11668019, Invitrogen) and subcloned for the establishment of MDCK-CAAX cell line.

Appendix 2. Computer simulation for folding lumen formation performed by Mr. R. Tanaka

Appendix.

A soft substrate was necessary for the folding after gel overlay.

Introduction

The elasticity of the ECM changes cell behaviors such as migration and adhesion (Dupont et al., 2011; Haga et al., 2005; Imai et al., 2015; Ishihara et al., 2016; Ishihara et al., 2013; Nukuda et al., 2015; Paszek et al., 2005; Rozario and DeSimone, 2010). To investigate how a glass substrate prevented folding (Figure 3.4A,B), a computational simulation was performed by building a 2D mathematical model of a vertical cross section of an epithelial sheet.

Materials and Methods

Appendix Figure 2.1. Definitions and parameters of the simulation.

In this model, an MDCK cells defined as a circle, whose chain represents the vertical cross section of an MDCK sheet (Appendix Figure 2.1A). The center of the chain is defined as the origin of the *X*-*Z* coordinate. r_{ci}, shown in a white dot, presents the position of the center of the blue circle. Appendix Figure 2.1B-F show the five parameters used in the simulation. First, a force causing random motion is given at the two points shown as black dots in Appendix Figure 2.1B by following form:

$$\boldsymbol{F}_{rand} = W \begin{pmatrix} \cos\theta_{rand} \\ \sin\theta_{rand} \end{pmatrix}$$

where W is magnitude of force, θ_{rand} is an angle of independent random function of time. As shown in Appendix Figure 2.1B, these two points are connected by a spring by following form:

$$\boldsymbol{F}_{con_{tibi}} = k_{con}(L_{con} - |r_{ti} - r_{bi}|)\frac{r_{ti} - r_{bi}}{|r_{ti} - r_{bi}|}$$

$$\boldsymbol{F}_{con_{biti}} = k_{con}(L_{con} - |r_{bi} - r_{ti}|)\frac{r_{bi} - r_{ti}}{|r_{bi} - r_{ti}|}$$

where k is the spring constant and L is the natural length of the spring. L_{con} is equal

to the diameter of a circle. t and b in subscript represent top and bottom, respectively. Note that the first positional relationship between top and bottom is maintained as the experimental observation showed the maintenance of apical-basal polarity (Figure 3.7A). Second, the repulsive force (subscribed in *rep*) that exists between cells is defined as follows (Appendix Figure 2.1C):

$$\boldsymbol{F}_{rep_{ij}} = k_{rep}\left(2R - \left|r_{ci} - r_{cj}\right|\right)\frac{r_{ci} - r_{cj}}{\left|r_{ci} - r_{cj}\right|}$$

where R is the radius of a circle, $j = i + 1$. Note that this equation holds only when $2R - \left|r_{ci} - r_{cj}\right| > 0$; otherwise, $F_{rep_{ij}} = 0$ .Third, shear tolerance is given by the two pairs of springs (Appendix Figure 2.1D) as the experimental observation showed cells kept the monolayer (Figure 3.1C). The dynamics of the parallel springs (subscribed in *sp*) are described as follow:

$$\boldsymbol{F}_{sp_{titj}} = k_{sp}\left(L_{sp} - \left|r_{ti} - r_{tj}\right|\right)\frac{r_{ti} - r_{tj}}{\left|r_{ti} - r_{tj}\right|}$$

$$\boldsymbol{F}_{sp_{bibj}} = k_{sp}\left(L_{sp} - \left|r_{bi} - r_{bj}\right|\right)\frac{r_{bi} - r_{bj}}{\left|r_{bi} - r_{bj}\right|}$$

and the dynamics of the crossed spring (subscribed in *sc*) are described as follow:

$$\boldsymbol{F}_{sc_{titj}} = k_{sc}\left(L_{sc} - \left|r_{ti} - r_{tj}\right|\right)\frac{r_{ti} - r_{tj}}{\left|r_{ti} - r_{tj}\right|}$$

$$\boldsymbol{F}_{sc_{bibj}} = k_{sc}\left(L_{sc} - \left|r_{bi} - r_{bj}\right|\right)\frac{r_{bi} - r_{bj}}{\left|r_{bi} - r_{bj}\right|}$$

where $L_{sp} = 2R$ and $L_{sp} = \sqrt{2R}$.

Fourth, cells are assumed to receive the repulsive force from the substrate as they are surrounded with ECM. The springs in Appendix Figure 2.1E represent the repulsive force and the dynamics is given as follow:

$$\boldsymbol{F}_{base_{xr}} + \boldsymbol{F}_{base_{xl}} + \boldsymbol{F}_{base_z} = k_{base}\begin{pmatrix} B_{xr} - r_{ci_x} \\ B_z - r_{ci_z} \end{pmatrix} + k_{base}\begin{pmatrix} B_{xl} - r_{ci_x} \\ B_z - r_{ci_z} \end{pmatrix} + k_{basetop}\begin{pmatrix} 0 \\ B_z - r_{ci_z} \end{pmatrix}$$

$$\boldsymbol{F}_{base_{xr}} + \boldsymbol{F}_{base_{xl}} + \boldsymbol{F}_{base_y} = k_{base}\begin{pmatrix} B_{xr} - r_{ci_x} \\ B_z - r_{ci_z} \end{pmatrix} + k_{base}\begin{pmatrix} B_{xl} - r_{ci_x} \\ B_z - r_{ci_z} \end{pmatrix} + k_{basebottom}\begin{pmatrix} 0 \\ B_z - r_{ci_z} \end{pmatrix}$$

where B is the initial r_{ci}, B_{xp} and B_{xn} is the initial *X* coordinate of r_{ci} of positive

and negative edge in a cell chain, respectively. When $B_z - r_{ci_z} < 0$, upper equation is applied. When $B_z - r_{ci_z} > 0$, lower equation is applied. The $F_{base_{xp}}$, $F_{base_{xn}}$ and F_{base_z}holds only when $B_{xp} < r_{ci_x}$, $r_{ci_x} < B_{xn}$, and $B_{xn} < r_{ci_x} < B_{xp}$, respectively.

Last, the migratory force is given as a driving force of cell migration from the cell experimental results (Figure 3.1 and 3.10). Three-dimensional imaging of cells in collagen gel embedded with beads revealed that the gel was mostly deformed along the direction of migration of the cells and rarely in the *Z*-axial direction. Immunofluorescent staining of 2P-MRLC showed that cells generated a traction force at the leading edge of folding movement. In addition, the myosin inhibitor completely prevented the lumen formation (Figure 3.10). From these experimental results, the migratory force is assumed as follow:

$$\boldsymbol{F}_{mig} = \begin{pmatrix} C \\ 0 \end{pmatrix}$$

where C is the magnitude of force, $+\boldsymbol{F}_{mig}$ and $-\boldsymbol{F}_{mig}$ are given to r_{ti} of the negative and positive edge in a chain, respectively (shown in red arrows in Appendix Figure 2.1F). Further, assuming that the viscosity of the cellular environment is sufficiently high, inertia can be ignored, and the velocity is proportional to the force (Yamao et al., 2011). Altogether, the dynamics of the circle position are described as follow:

$$\mu \frac{dr_{ti}}{dt} = \sum \boldsymbol{F}_{rand_{ti}} + \sum \boldsymbol{F}_{str_{tibi}} + \sum \boldsymbol{F}_{rep_{cicj}} + \sum \boldsymbol{F}_{sp_{titj}} + \sum \boldsymbol{F}_{sc_{tibi}} + \sum \boldsymbol{F}_{base_{ti}} \left(\pm \sum \boldsymbol{F}_{mig} \right)$$

$$\mu \frac{dr_{bi}}{dt} = \sum \boldsymbol{F}_{rand_{bi}} + \sum \boldsymbol{F}_{str_{biti}} + \sum \boldsymbol{F}_{rep_{cicj}} + \sum \boldsymbol{F}_{sp_{bibj}} + \sum \boldsymbol{F}_{sc_{bitj}} + \sum \boldsymbol{F}_{base_{bi}}$$

where μ is a viscous modulus.

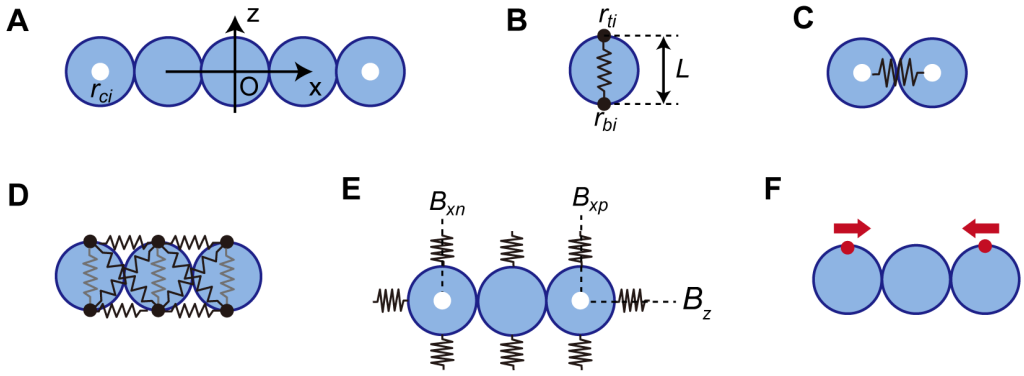

Appendix Figure 2.1 Definitions and parameters used in the simulation

(**A-F**) Position of variable and its conceptual diagram.

Appendix Table 2.1 The parameter values used in the simulation

Parameter	Value	Parameter	Value
W	5	R	100
k_{con}	0.5	k_{rep}	0.3
k_{sp}	0.04	k_{sc}	0.45
k_{base}	0.005	$k_{basetop}$	0.005(control) or 2.0 (stiff)
$k_{basebottom}$	0.005(control) or 2.0 (stiff)	C	5
μ	1	B_x	200n (-9<n<9)
B_y	0		

Results

By modulating these parameters appropriately (Appendix Table 2.1), the model simulated folding (Appendix Figure. 2.2A). However, the monolayer buckled during folding, which did not occur in the MDCK cell sheets. This may be because the model lacks a parameter for cell-substrate adhesion. Adding this parameter to the model is a challenge for the future. Then, the elasticity of the substrate was increased to

observe the contribution of substrate elasticity. The elasticity of the collagen gel here is approximately 0.6 kPa according to the results of another study (Mizutani et al., 2006a). The elasticity of a glass substrate (2–4 GPa) (Butcher et al., 2009) is virtually infinitely greater than that of the gel. Therefore, we increased the spring constant to the maximum value for a stiff substrate and observed the shape of the monolayer. When the elasticity of the top or bottom spring was increased, the monolayer did not fold (Appendix Figure 2.2B,C). These results support the importance of the elasticity of the surrounding substrate in the folding of MDCK cells after the gel overlay.

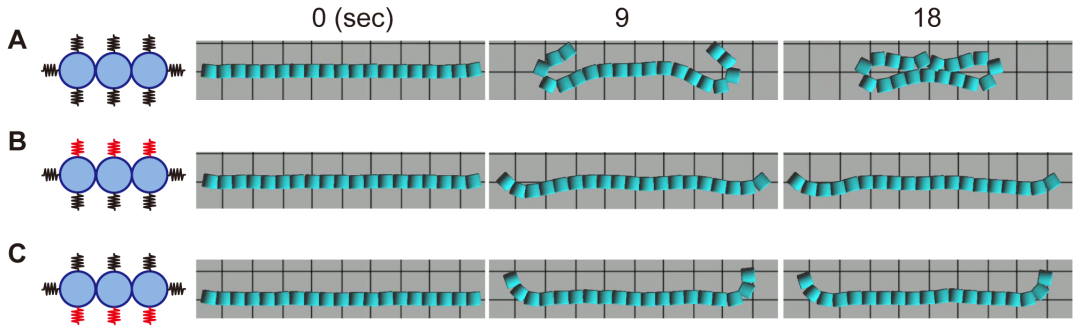

Appendix Figure 2.2 Results of the simulation.

(A) Results with the parameters modulated appropriately. (B,C) Results with the elastic parameter of the upper (B) or lower (C) substrate is increased. (shown in red)

Discussion

Consistent with the experimental results of folding of the MDCK sheet, the computer simulation demonstrated that a rigid substrate prevented folding. Because we did not use exact values for all of the parameters, further analyses are required, such as measuring the deformation volume of the ECM, the traction force during cell migration, and cell-cell adhesion force.

Appendix 3. Experiments performed by Mr. G. Ogata

Appendix 3-1. Folding Lumens with the arbitrary shapes after gel overlay.

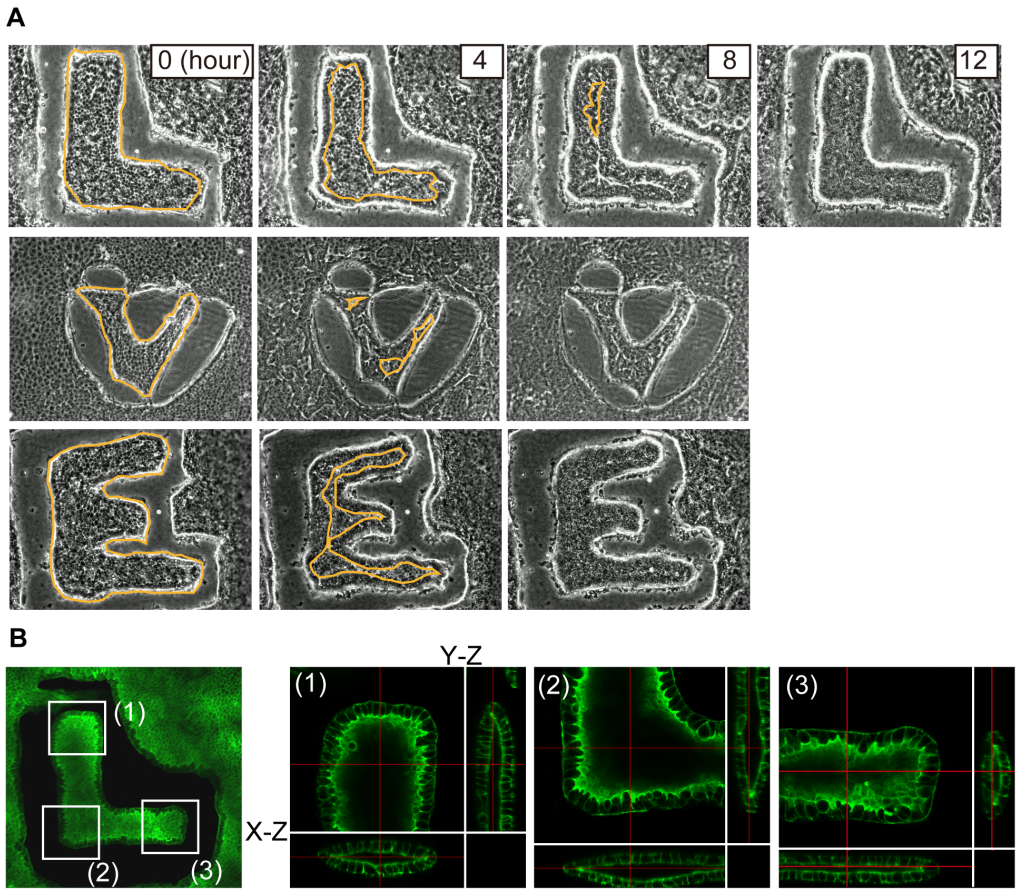

The folding lumen formation of MDCK sheets cut in the arbitrary shapes.

(**A**) Temporal sequence of epithelial sheets cut in "L", "V", "E"-shapes. Orange lines represent the migrating edge of the folding.

(**B**) Fluorescent images of F-actin in the "L"-shaped structure shown in Figure 3.3A. Images (1–3) are enlargements of indicated areas in the leftmost image.

Appendix 3-2. Roscovitine treatment to the folding lumen formation

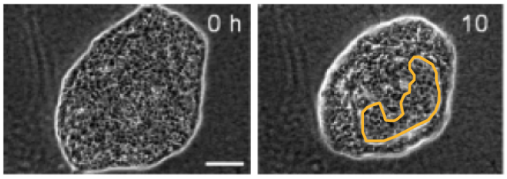

Time-lapse imaging of roscovitine-treated MDCK colony after the gel overlay.

Roscovitine was added immediately after the gel overlay. The Orange line indicates the migrating edge of folding. Scale bar, 100 μm.

Appendix 3-3 Collagen Zymography in folding lumen formation

Materials and Methods

The culture supernatant of MDCK cells in folding migration was harvested and mixed with equal volume of 2x lading buffer (0.5 M Tris-HCl, pH 6.8; 3% glycerol; 0.004% bromophenol blue). Then the samples were subjected to 0.25% collagen-containing 4% SDS-polyacrylamide gel electrophoresis. After electrophoresis, gels were rinsed with renuturation buffer renaturation buffer (2.5% Triton-X100; 54 mM Tris-base, pH 7.5; 200 mM $CaCl_2$; and 200 mM NaCl) and incubated in a developing buffer (54 mM Tris-base, pH 7.5; 200 mM $CaCl_2$; and 200 mM NaCl) at 37 °C for 24 h. The gel was stained with Coomassie brilliant blue R250 and observed.

Results

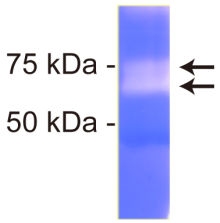

Collagen zymography of the culture supernatant from MDCK cells in gel overlay.

The black arrows point to the MMP bands that consistent with the molecular weight of the precursor (upper) active (lower) forms of MMP-8.

Appendix 3-4 Gel sandwich assay to MDCK monolayer

Materials and Methods

For the collagen gel sandwich assay, the collagen solution was placed over the glass coverslip with a radius smaller than that of the glass dish. After the collagen was gelated, the coverslip was gently put onto the MDCK sheets with collagen-side down.

Results

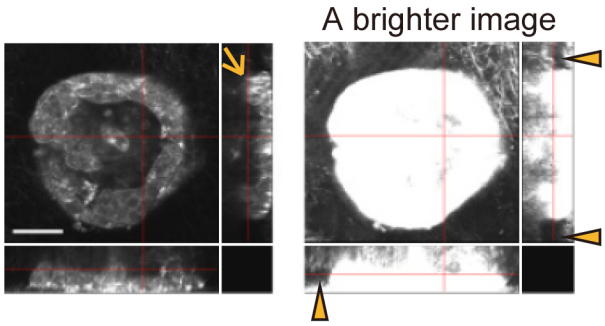

MDCK cells under the collagen gel did not migrate to collagen-gel free space.

Interference reflection images of an MDCK sheet in gel sandwich assay. Red lines indicate where the sectional views were generated. Arrow in the right column of the image on the left points to the cells that migrated to the upper layer. Overexposure images were shown in right. Arrowheads point to the collagen gel-free space between collagen layers. Scale bar, 50 μm.

Appendix 4. The investigation of fluidity in Matrigel performed by Dr. M. Imai

Materials and Methods

Liquified Matrigel was poured in the hand-made glass dish with 16 mm diameter. After the gelation of Matrigel, holes were opened in Matrigel by an aspirator. Then Matrigel was incubated at 37°C for 3 days. The surface of Matrigel was observed immediately and 3 days after the hole opening.

Results

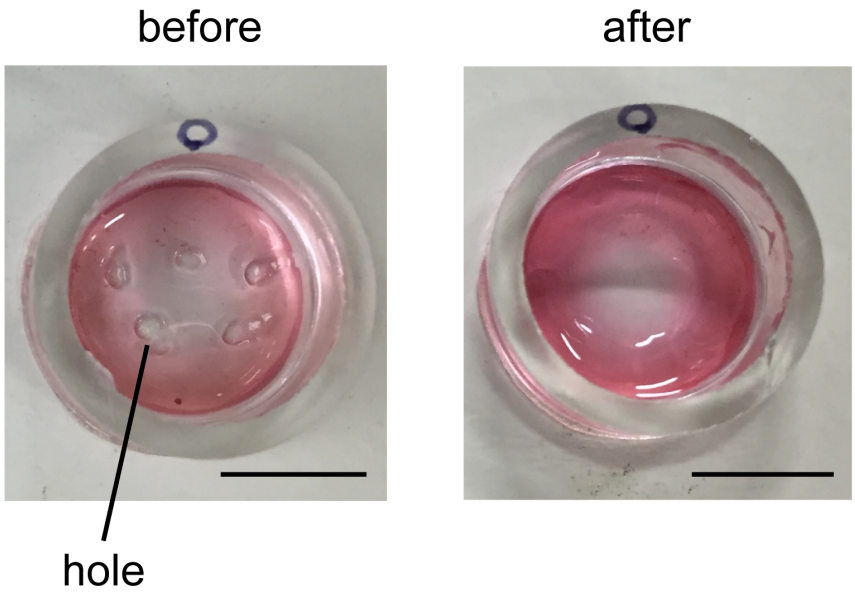

Perforated normal Matrigel became flat after the incubation at 37°C.

The images of the surface of perforated Matrigel before and after 3 days incubation at 37°C. Scale bars, 10 mm.

Appendix 5. AFM measurement of GP-Matrigel performed by Dr. S. Ishihara

Materials and Methods

AFM (Nanowizard4, Bruker) using a microscope (TE300, Nikon Instech) was used to measure the elasticity of the surface of gels. The AFM was equipped with pyramidal silicone nitride cantilevers (MLCT; Bruker) with a spring constant of 0.06 N/m, calibrated by thermal tuning using a simple harmonic oscillator model. Samples were indented with a calibrated force of 0.5-1.5 nN in. The elastic properties (Young modulus) were estimated after the application of the Hertzian model with an assumed Poisson's ratio of 0.5.

Results

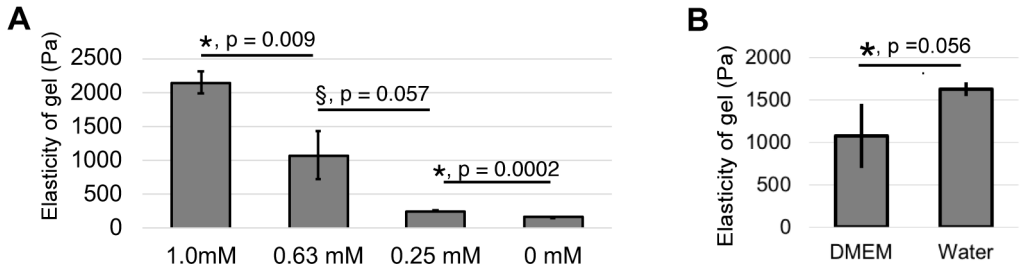

AFM measurement of GP-Matrigels

(**A**) Surface elasticity of GP-Matrigel. (**B**) Surface elasticity of 0.63 mM GP-Matrigel immersed in DMEM or pure water. $n = 3$ area from 1 experiment. Means ± S.D. *, student *t*-test. §, welch *t*-test.

Appendix 6. Mathematical model performed with Dr. M. Akiyama

Introduction

The deformations of epithelial sheets are foundation of 3D morphogenesis. The deformations are provided by the accumulation of shape change and migration of single cells. A mathematical framework called the vertex dynamics model has often been a powerful tool to understand the two or three-dimensional morphogenesis of cell sheets (Honda et al., 2004).

In this study, the vertex dynamics model is adopted for introducing deformation of cell sheets in order to examine our hypothesis that positive feedback between an extending cell area and enhanced water transport induces G-dome formation. We also build a phenomenological 2D model representing the interaction of the ECM interface, cell, and water absorbed by cells.

Materials and Methods

Mathematical model

In our modeling, we represent the whole structure of a cellular tissue on the gel is represented as a set of triangular prisms; that is, a cell layer is represented by the top faces of triangular prisms (Appendix Figure 6.1).

In this vertex dynamics model, the whole structure of a cellular tissue on the gel is represented as a set of triangular prisms; that is, a cell sheet is represented by the top faces of triangular prisms (Appendix Figure 6.1). A cell layer on a gel represents in a circular region Ω. The whole system is described as a set of *N* triangular prisms and the vertex dynamics model is consists of an equation of vertices in the triangular region representing cell groups and an equation of total water absorbed by cells on each triangle.

First, a governing equation of the i-th vertex $\mathbb{r}_i\ (i = 1,2,\cdots,M)$ in the triangulated region is constructed, where the notation M stands for the total number of vertices. In this modeling, two potential energies of the bending energy and the volume conservation are considered as follow:

$U^{Bend} = \frac{\kappa_1}{2}\sum_{i=1}^{M}\sum_{(j,k)\in\Lambda_i}(\mathbb{m}_j \cdot \mathbb{m}_k - \cos(\theta))^2,$

$U^{Volume} = \frac{\kappa_2}{2}(V - V_{Ideal})^2,$

where κ_1 and κ_2 are positive constants. The bending energy U^{Bend} describes an

effect that an angle of two neighboring triangles with $\mathbb{r}_i$ preserves to a specified angle θ. The vectors $\mathbb{m}_j$ and $\mathbb{m}_k$ are the outward normal vectors of j-th and k-th triangle, respectively. The notation Λ_i stands for the set of pairs (j,k) of two neighboring triangles with $\mathbb{r}_i$. In this simulation, the angle θ is specified as $\theta = 0$, leading that vertices move to the direction that two neighboring triangles become flat.

In general, bending energy often adopts the formula $\kappa C^2/2$ for a continuous curve, where κ is a positive constant, and C is curvature. Here, this model considers a bending energy on a discrete curve, defined by a point sequence as follows. Suppose that θ is an angle between outward normal vectors for two neighboring edges on a discrete curve, and consider the energy $\kappa\theta^2/2$. If θ is sufficiently small, $\theta \sim C$ is obtained, where the notation $a \sim b$ represents that a is asymptotically equal to b. Hence, $\kappa C^2/2 \sim O(\theta^2)$ is obtained, where the notation O stands for the Landau symbol. On the other hand, in the bending energy in this model, if two vectors $\mathbb{m}_j$ and $\mathbb{m}_k$ are almost parallel, that is, the angle between $\mathbb{m}_j$ and $\mathbb{m}_k$ is sufficiently small, the following equation holds:

$(\mathbb{m}_j \cdot \mathbb{m}_k - \cos(\theta))^2 \sim (1 - \cos(\theta))^2 \sim O(\theta^4)$.

This implies that our bending energy formula is softer than the general formula. The formulation of $O(\theta^4)$ is already discussed in the previous paper (Kobayashi et al., 2018). Especially, it is easy to see that the bending energy value increases, depending on the total number of triangles. However, this is intuitively strange. In the other method, the bending energy value does not change depending on the number of triangles. In order to avoid the same problem in this model, the parameter κ_1 is considered as the bending energy coefficient per unit area. Let R and A be the radius of the circular region and be the average area of a triangle, respectively. $A \sim \pi R^2/N$ is obtained in the initial state. Here $\kappa_1 = \kappa_1' A$ is defined, where κ_1' is a positive constant. By this formulation, it may be expected that the energy value will not change even when the total number N of triangles is changed. In this numerical simulation, although $\kappa_1' = 100.0$ is fixed and the number of N is varied from about 3000 to 12000, similar patterns that are almost similar were observed. On the other hand, we do not know what kind of bending energy formulation is the most appropriate when θ is large. The volume conservation energy U^{Volume} shows an effect that the volume of a set of all triangular prisms preserves to an ideal value V_{Ideal}.

A governing equation of the i-th vertex $\mathbb{r}_i$ which is obtained as the gradient

system of the potential energy $U = U^{Bend} + U^{Volume}$ is given as follows:

$$\tau_i \frac{d\mathbb{r}_i}{dt} = -\frac{\delta U}{\delta \mathbb{r}_i},$$

where the term $\delta U/\delta \mathbb{r}_i$ stands for the functional derivative of U and the time constant τ_i is explained in the later part of this section.

Second, the equation of the total water that cells on j-th triangle absorb is described as follows:

$$\frac{dw_j}{dt} = f(c_j),$$

where the function $f(c_j) = (\tanh(\mu(c_0 - c)) + 1)/2$ is specified from the experimental observations. The variable c_j stands for thickness of cells on the j-th triangle, where c_0 and μ are positive constants. Note that in this model, the thickness c_j is determined as the height at the centroid of the j-th triangle (Appendix Figure 6.1). Since we have $\lim_{c\to 0} f(c) = 1$ and $\lim_{c\to \infty} f(c) = 0$, when the thickness of the cells are small, the absorption of water is large, and vice versa. The function type of $f(c_j)$ is introduced based on the experimental results. The relationship between the height of the cells and the amount of water absorbed is not fully understood. However, as shown in Figure 4.15B,C, thinner cells absorbed more water than when they were taller. From this result, the function f is adopted as the simplest nonlinear function. As seen from the above equation, when c is greater than c_0, the cells hardly take water, and vice versa. Thus, the parameter c_0 must be determined appropriately. Here, c_0 is defined as the mean height of cells. The initial height of cells is set with a uniform random number in the closed interval $[0.8, 1.2]$, as described later. Therefore, in this case, it is reasonable to set c_0 to approximately 1.0. Note that if the initial cells' height is changed, c_0 will change as well. In this sense, the parameter c_0 setting is not so strict. The parameter μ is an important to change the shape of the function f. In particular, it can be confirmed in numerical computations that minor changes do not exhibit major differences of output patterns. In addition, when the water is absorbed by cells, the volume of the whole structure (the set of triangular prisms) increases. That is, the ideal value V_{Ideal} at the time t is described by

$$V_{Ideal}(t) = V_{Init} + \rho \sum_{j=1}^{N} w_j(t)\, A_j(t),$$

where the notation V_{Init} stands for the initial volume for the whole of triangular prisms,

and the notation $A_j(t)$ stands for the area of j-th triangle at the time $t \geq 0$. ρ is a positive constant. In this model, the amount of absorbed water is not scaled. Therefore, it is necessary that the amount of absorbed water is converted to the ideal volume using the parameter ρ. The cells thickness c_j is supposed to depend on the cells area, thus the thickness $c_j(t)$ at the time $t > 0$ is defined by

$$c_j(t) = c_j(0)\left(\frac{A_j(0)}{A_j(t)}\right).$$

As seen from the equation, the volume of the cells on each triangular prism is constant. From the observation of cells (Figure 4.19), this model assumes that cell proliferations do not occur. Furthermore, we confirm that the displacement of the gel is small when cells are thicker. Therefore, the time constant of vertices of the j-th triangle is assumed to be large when c_j is large, and to be small when c_j is small. Note that this is the most important assumption in this mathematical model. In this vertex dynamics model, since some triangles share the i-th vertex $\mathbb{r}_i$, the time constant τ_i of $\mathbb{r}_i$ is defined as follows:

$$\tau_i = \frac{1}{\#\Pi_i}\sum_{j\in\Pi_i}\frac{1}{f(c_j)}.$$

In the above definition, the notation $\#\Pi_i$ stands for the number of elements contained in the set Π_i which contains the labels' j-th triangles, along with the vertex $\mathbb{r}_i$. If this assumption is removed, dome-like patterns cannot be observed.

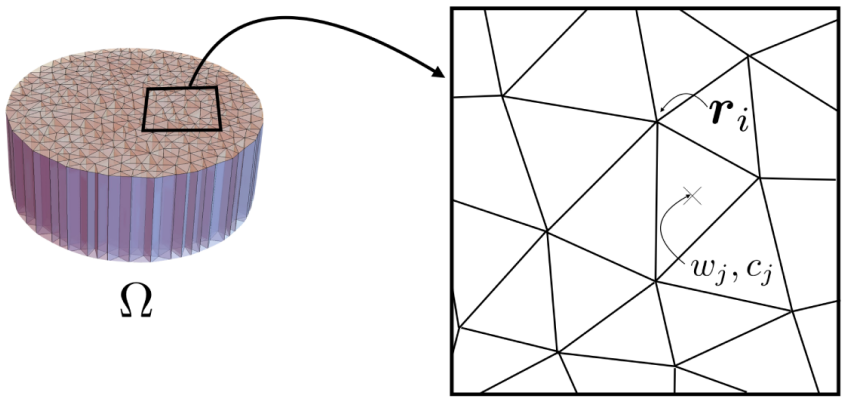

Appendix Figure 6.1 Details of the symbols appearing in the model
Position of variable and its conceptual diagram.

Initial state, boundary condition, and terminated condition

The initial state of this numerical simulation is defined as follow. Ω was a circular region given as a disk with the specified radius $R = 12$ and consider a triangulation on the region Ω, which is determined by *Wolfram Mathematica*. As the boundary condition, vertices on the boundary of Ω are fixed ($z = 1$), and the other vertices are given small perturbations (see the Appendix Figure 6.2A,C in results section). The thickness c_j defined at the j-th triangle is given from a uniform random number in the closed interval $[0.8, 1.2]$. Also, the initial value of the variable $w_j(t)$ for all indices j is given as $w_j(0) = 0$. In the process of determination of the initial state, the *Mersenne Twister* method (Matsumoto and Nishimura, 1998) is used for pseudorandom number generation. Moreover, this model adopts values of parameters as listed in Appendix Table 6.1. Second, in some numerical simulations, since self-intersection of two triangles occurred, a mathematical condition for self-intersection is used, and if its condition is satisfied, the numerical simulation is then terminated.

Appendix Table 6.1. Parameters of the simulation.

Parameter	Value	Descriptions
μ	10.0	Parameter of the function f
c_0	1.0	Parameter of the function f
ρ	0.001	Parameter of convert ratio
κ_1	3.564	Coefficient of the potential energy U^{Bend}
κ_2	0.05	Coefficient of the potential energy U^{Volume}
N	6459	Number of vertices
M	12695	Number of vertices
$Atol$	1.0e-8	Absolute tolerance value of embedded R.K. method
$Rtol$	1.0e-8	Absolute tolerance value of embedded R.K. method

Computational Method and Visualization

This vertex dynamics model was solved by using a variation of the embedded *Runge-Kutta* method –the Bogacki–Shampine method (Bogacki and Shampine, 1996), adapting the absolute and relative tolerance values. We confirmed that if the absolute and relative tolerance values were smaller than ones listed in Appendix Table 6.1, the final pattern did not change. These numerical results were visualized by the graphical library named Graphics Library for Scientific Computing (G. L. S. C.) 3D, developed by Masakazu Akiyama (Meiji Uniersity, Japan), Kazuma Tateiri (Hokkaido University, Japan), Takamichi Sushida. (Salesian Polytechnic, Japan), and Ryo Kobayashi (Hiroshima University, Japan).

Results

In the numerical computations, we calculated the model with or without cells. As shown in Appendix Figure 6.2, although the initial conditions were the same, the final states were different patterns, showing that some domes were generated within the circular region Ω with the existence of cells. Hence, these results obtained by numerical simulations support that cell existence played an important role in determining the final gel pattern.

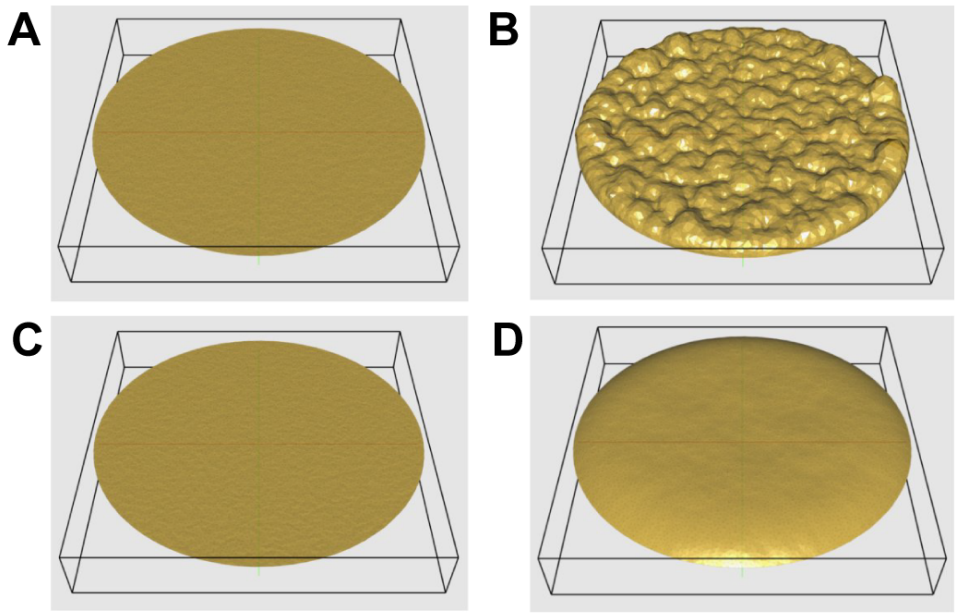

Appendix Figure 6. The results of numerical simulation.

(**A** and **C**) The initial state of the domes. (**B** and **D**) The final state of the domes. (B) Cells on the gel corresponded to Figure 4.11A. (D) Cells are not on the gel, which corresponds to GP-Matrigel in the water of Figure 4.12F. In this simulation, we set the thickness of all cells to 0.0, that is, for all index $j,\ c_j = 0$.

Reference in Appendix

Bogacki, P. and Shampine, L. F. (1996). An efficient Runge-Kutta (4,5) pair. *Computers & Mathematics with Applications* **32**, 13.

Hancock, J. F., Cadwallader, K., Paterson, H. and Marshall, C. J. (1991). A CAAX or a CAAL motif and a second signal are sufficient for plasma membrane targeting of ras proteins. *EMBO J* **10**, 4033-9.

Honda, H., Tanemura, M. and Nagai, T. (2004). A three-dimensional vertex dynamics cell model of space-filling polyhedra simulating cell behavior in a cell aggregate. *J Theor Biol* **226**, 439-53.

Karasawa, S., Araki, T., Yamamoto-Hino, M. and Miyawaki, A. (2003). A green-emitting fluorescent protein from Galaxeidae coral and its monomeric version for use in fluorescent labeling. *J Biol Chem* **278**, 34167-71.

Kobayashi, Y., Yasugahira, Y., Kitahata, H., Watanabe, M., Natsuga, K. and Nagayama, M. (2018). Interplay between epidermal stem cell dynamics and dermal deformation. *NPJ Comput. Mater.* **4**.

Matsumoto, M. and Nishimura, T. (1998). Mersenne Twister: A 623-Dimensionally Equidistributed Uniform Pseudo-Random Number Generator. *ACM Transactions on Modeling and Computer Simulation* **8**, 27.

Yamao, M., Naoki, H. and Ishii, S. (2011). Multi-cellular logistics of collective cell migration. *PLoS One* **6**, e27950.